Response of American Electric Power to Draft Dam Assessment Report Recommendations
Philip Sporn Plant

At the request of the U.S. EPA, American Electric Power has reviewed the recommendation section of the draft Dam Assessment Report prepared by Dewberry for the fly ash and bottom ash ponds at the Philip Sporn Plant. In summary, AEP is in general agreement with some of the recommendations, but strongly disagrees with the conclusion that the facilities are "rated as poor" for continued safe and reliable operation. American Electric Power believes a "Fair" or better rating is warranted based on the following:

- The facilities have been designed, permitted, monitored and maintained in accordance with the requirements of the West Virginia dam safety regulations and in accordance with the standards of good engineering practice. The facilities have been routinely inspected by qualified staff of the West Virginia Department of Environmental Protection and have undergone a number of professional engineering assessments by recognized experts since the Kingston failure. Additionally, the facilities undergo routine inspection by plant personnel and annual inspections by qualified professional engineers.

- In response to the TVA Kingston impoundment failure, AEP worked with the WVDEP Dam Safety Office to re-evaluate the integrity and safety of these facilities. Those reviews again confirmed that the Sporn ash ponds are stable and safe. The following inspections and investigations have been performed in 2009 and support the conclusion that the facilities are stable and safe:

    - Independent professional engineer detailed inspection with findings that concluded " the overall condition remains good" and specific work was needed to address localized surface sloughing and erosion repairs: February 12, 2009
    - WV Department of Environmental Protection dam safety inspection (March 11, 2009) with recommendations that indicated the need for additional studies for a 100-year Ohio River flood scouring potential of the eastern embankment and the repair of the surface sloughing on the down stream embankment slopes: Scour analysis has been completed and there is not need for special revetment of the slope. An application for the approval of the modifications necessary to improve the down stream slopes of the facility is currently under review by the regulatory agency. We are awaiting final approval to proceed with the repairs.
    - Fulfilled an Order from WVDEP to perform a number of detailed structural integrity and safety investigations. Following the completion of the item outlined in the order, DEP closed the Order on May 27, 2009.
    - AEP engineering staff inspection on August 27, 2009, including a review of the monitoring and surveillance data, concluded that the facility was overall in "good condition" with the need with the surface repairs noted..
    - Performed quarterly dam deformation surveys at 30 points around the ponds to detect movement. All findings were within normal parameters.
    - Installed additional wells to monitor water levels within the dikes to further improve our monitoring and surveillance efforts.
    - Performed additional soil borings and laboratory analyses to confirm the strength of the soils in the dikes and foundations. No issues or abnormalities were found.
    - Performed analyses to confirm the "factor of safety" in the dike design and construction and all safety factors met or exceeded required standards.
    - Evaluated the potential for effects from underground mine subsidence in the area. No problems were found.

- AEP has thoroughly reviewed the Kingston root cause report and worked with Mr. Barry Thacker, P.E., owner of GeoEnvironmental, Inc., and others to understand the Kingston failure. As a result of these reviews, AEP has concluded that the unique conditions that led to the failure at Kingston do not exist at the Philip Sporn facilities.

It is AEP's understanding that the "poor" rating in the draft report is driven primarily by three issues:

1. Liquefaction concerns associated with the use of fly ash and bottom ash as a material of construction for foundations and existing dikes.
2. Surface sloughing, erosion surface irregularities of some of the bottom ash and fly ash embankments.
3. Slope stability issues related to ground vibration induced by the nearby railroad.

The draft report contains recommendations for conducting field remediation and additional analyses to address these issues. AEP provides the following response to these three noted items:

1. **Liquefaction concerns associated with the use of fly ash and bottom ash as a material of construction for foundations and existing dikes**. AEP concurs with the statement in the draft report that fly ash materials may be susceptible to liquefaction under certain conditions. The draft report contains a recommendation to perform analyses to determine the potential for soil liquefaction. Studies have been completed and based on those studies AEP has concluded that the conditions necessary to liquefy the fly ash located in the embankments and foundations at the Philip Sporn site are not present. Attachment A provides additional information and copies of the relevant studies.

2. **Surface sloughing, erosion surface irregularities of some of the bottom ash and fly ash embankments**. AEP agrees that this condition needs to be corrected and has been monitoring the condition and working with the WVDEP to implement remedial measures. AEP has submitted a formal design modification request to WVDEP to implement field improvements to eliminate the surface sloughs and erosion gullies. We expect to receive approval to implement the remedial measures and will initiate and complete the field work as soon as possible. This work will result in greater than one acre of soil disturbance, thus requiring approval under the WV general permit for storm water discharges associated with construction activity. Attachment B to this package provides a detailed description of the status of these activities and the plans going forward.

3. **Slope stability issues related to ground vibration induced by the nearby railroad.** AEP is fully aware of the localized repair needed to address the shallow surface instability and this work was included in the above permit request to the WVDEP. Steps to repair surface instability on the fly ash pond dike will be completed. AEP will also complete vibration measurements and analysis of the fly ash pond dike caused by the railway traffic. Thereafter, AEP will prepare a report summarizing the results of the monitoring and analyses. Attachment C provides additional information on this issue. The proposed remedial measures for the fly ash pond dike will be similar to those previously completed in 2002 for the bottom ash pond dike. The bottom ash dike has not experienced further instability following those repairs.

In addition, we note that the EPA news release dated October 29, 2009 stated that "EPA contractors identified factors at the AEP Sporn facility that are similar to the Kingston facility – specifically, both facilities piled coal ash and bottom ash around the impoundment to raise the impoundment's walls." In response to that statement, AEP provides a draft "white paper" found in Attachment D which summarizes many of the critical differences between the Sporn and Kingston facilities. After reviewing this information, the liquefaction information submitted in attachment A and the previously submitted design information for the facilities, we believe EPA and its contractor will conclude that the Sporn facility is stable and safe, and that the proposed "poor" rating is not justified.

AEP requests EPA's thoughtful consideration of these comments and concurrence that we have provided compelling justification to warrant a revision of the overall rating of these facilities to a rating of "fair" or higher. As also requested by EPA, AEP will provide additional comments on the entirety of the draft report by the November 30, 2009 deadline.

ATTACHMENT A
STUDIES IN RESPONSE TO COMMENTS REGARDING POTENTIAL FOR LIQUEFACTION OF EMBANKMENT AND FOUNDATION SOILS
U.S. EPA DIRECTED DAM SAFETY ASSESSMENT
PHILIP SPORN PLANT – MASON COUNTY, WEST VIRGINIA

Response to contractor's conclusion that fly ash material strata may be susceptible to liquefaction under certain conditions and associated recommendation for further study.

We concur with the US EPA inspector that "fly ash material strata may be susceptible to liquefaction under certain conditions." We believe that the requested studies have been conducted and based on those studies, have concluded that the conditions necessary to liquefy the fly ash located in the embankments and foundation soil of the impoundments are not present at the site of the Philip Sporn Plant due to its geologic and seismic setting (anticipated ground accelerations in the range of 0.06g as indicated by the US EPA inspector).

The liquefaction potential of fly ash has been understood within the engineering profession since at least the early 1970's, (Casagrande, Gandhi 1999, Wolfe 2007, Wolfe 2009) even though it has not been highly publicized. In order to liquefy fly ash, and for that matter any material, it is imperative that a mechanism capable of inducing high pore pressures in the materials exists, triggering a resulting overall lost of strength of the material. Thus, the efforts associated with the study of the liquefaction of fly ash have focused on understanding the triggering mechanism of the behavior.

In 2005, American Electric Power commissioned an evaluation of the liquefaction of ponded ash at The Ohio State University. In this work, samples of ponded fly ash were re-constructed to different densities and subjected to cyclic loading until liquefaction was achieved. Based on the results of these tests, relationships were developed between the imposed shear stress ratio and the number of cycles to liquefy fly ash to assist in design and review efforts of AEP' facilities. In addition, ground response analyses were performed using design accelerations of 0.08g and 0.15g. These accelerations were selected as they represent the upper range of accelerations induced by credible earthquakes within the locations of AEP Fly Ash impoundments. The results of The Ohio State University research revealed that ground accelerations of these magnitudes were not capable of inducing liquefaction of the fly ash. (2005). These results were published by the researchers in peered reviewed conferences and journals. Liquefaction studies in ponded ash conducted by Gandhi (1999) concluded that there is no risk of liquefaction for ash deposits located in earthquake zones where the values of the acceleration do not exceed 0.211g. The results of the Ohio State evaluation are in agreement with the conclusions drawn on the basis of Gandhi's 1999 research.

It is worth mentioning, that the raising of the eastern dike of the Fly Ash pond at the Sporn Plant was planned and constructed under the technical supervision of Arthur Casagrande as AEP consultant in 1972 (Amaya 1998) who was well aware of the liquefaction potential of fly ash. In summary, AEP has studied the liquefaction potential of fly ash and concluded that the conditions necessary for the

liquefaction of the ash materials located in the embankments and foundation soil of the impoundments are not present at the site of the Philip Sporn Plant due to its geologic and seismic setting.

Works Cited:

1. Gandhi, R. S. "LIQUEFACTION ANALYSES OF POND ASH." Proceedings of the 15th International Conference in Solid Waste Technology & Management. Philadelphia, PA. Dec. 12-15, 1999.
2. Wolfe, W. E., B. Zand, W. Tu, P. Amaya, T.S. Butalia. "Evaluation of Liquefaction Potential of Impounded Fly Ash." World of Coal Ash Conference. Covington, KY. May 7-10, 2007.
3. Wolfe, W. E., B. Zand, W. Tu, P. Amaya, T.S. Butalia. " An Experimental Investigation on Liquefaction Potential and Post-Liquefaction shear strength of impounded Fly Ash." Elsevier. Fuel Journal, Vol. 88, Number 7, July 2009.
4. "Evaluation Potential of Impounded Fly Ash." The Ohio State University, Department of Civil and Environmental Engineering and Geodetic Science. Report to American Electric Power. October 17, 2005.
5. Amaya, P. J., and C.S. Togni. "Unit 5 Fly Ash Facility Engineering Report." Report prepared for Appalachian Power Company, Philip Sporn Electric Generating Plant. Prepared in support of the application for a certificate of approval in accordance with title 47 of the West Virginia Division of Environmental Protection, Dam Safety Rule, Series 34. Geotechnical Engineering Section, American electric Power Service Corporation. July, 1998.

Evaluation of Liquefaction Potential of Impounded Fly Ash

Draft Final Report

The Ohio State University Research Project # 60005876

July, 2005 – October, 2005

Submitted to: American Electric Power

Department of Civil and Environmental Engineering and Geodetic Science

The Ohio State University

470 Hitchcock Hall, 2070 Neil Avenue

Columbus, Ohio 43210

October 17, 2005

Abstract

The objective of this study was to evaluate the liquefaction potential of impounded fly ash material from a power plant of American Electric Power (AEP). Standard cyclic triaxial tests were performed on reconstituted samples at various relative densities, confining stresses, and cyclic stress ratios. After cyclic triaxial tests, samples were reconsolidated at the initial effective confining stress and subjected to consolidated undrained (CU) triaxial tests to determine the static undrained shear strength. Additional CU tests were performed to determine the initial static undrained shear strength. The design seismic loading in terms of cyclic stress ratio and equivalent number of cycles were obtained from ground response analyses using SHAKE. The cyclic loading imposed by the design earthquakes was founded to be lower than the cyclic strength of the fly ash material.

Table of Contents

List of Figures

List of Tables

Chapter 1 Introduction

1.1 Project Objective

The objective of this research was to evaluate the liquefaction potential of impounded fly ash material from a power plant of American Electric Power (AEP). This evaluation, which includes a laboratory cyclic behavior characterization combined with an equivalent-linear seismic ground response analyses carried out with SHAKE, was needed to support the predesign analyses for a proposed landfill design over the top of an existing fly ash pond.

1.2 Outline of Project

The impounded fly ash material provided by AEP to OSU for investigation was produced by the Mitchell power plant. The specific gravity, grain size distribution, and the standard proctor compaction test results were provided by AEP. The cyclic strength of the fly ash material was measured using standard cyclic triaxial strength test method according to ASTM D5311. A total of 18 reconstituted samples were prepared and tested with the cyclic triaxial testing method. These samples were prepared using either wet tamping or wet pouring methods to obtain three different density levels. The test matrix variables included the confining stress, shear stress, and the relative density of the material. After cyclic triaxial tests, most of the samples were

reconsolidated at the initial effective confining stress and subjected to consolidated undrained (CU) triaxial tests to determine the static undrained shear strength. Additional four CU tests (one for each relative density) were performed to determine the initial static undrained shear strength.

One-dimensional equivalent linear ground response analyses were carried out on two typical soil profiles of the fly ash pond based on the information given by AEP to estimate the threat imposed by design seismic events. The liquefaction potential of the fly ash material was evaluated based on the comparison of the loading conditions required to trigger liquefaction obtained in the laboratory cyclic triaxial tests and the calculated earthquake-induced loading from ground response analyses.

Details of the laboratory testing program and ground response analyses are presented in the next chapter. Chapter 3 includes a discussion of results. Chapter 4 presents project summary and conclusions. The detailed testing data and numerical analyses results are presented in the appendices.

Chapter 2 Testing Procedures and Numerical Analyses

All laboratory tests and numerical modeling was carried out in the Soil Mechanics Laboratory of the Department of Civil and Environmental Engineering and Geodetic Science at The Ohio State University.

2.1 Sample Preparation and Testing

Samples were prepared with 86%, 90%, 95%, and 105% of maximum dry density obtained from standard Proctor test (ASTM D 698). The samples were made using either wet tamping or pouring method.

2.1.1 Wet Tamping Method

All the samples were compacted in Harvard Miniature molds (1.31" in diameter, 2.8" in length) using a 25 lb hand tamper. Each sample was compacted in five equal lifts in such a way that the last compacted lift be about 0.5" above the top level of the mold. The top surface of each layer was roughed up before adding the next later to allow a better bonding between the layers. In order to find the proper compaction effort for each lift, calibration compaction tests were

conducted and compaction curves were established for various moisture contents and number of tampers per lift. Figure 2.1 shows two examples of such curves. The obtained curves then were utilized to compact samples with desired target relative dry density. The samples were weighed, and their height, diameter, and moisture content were measured to calculate the actual dry densities. Samples with density more than 1% off the target dry density were discarded.

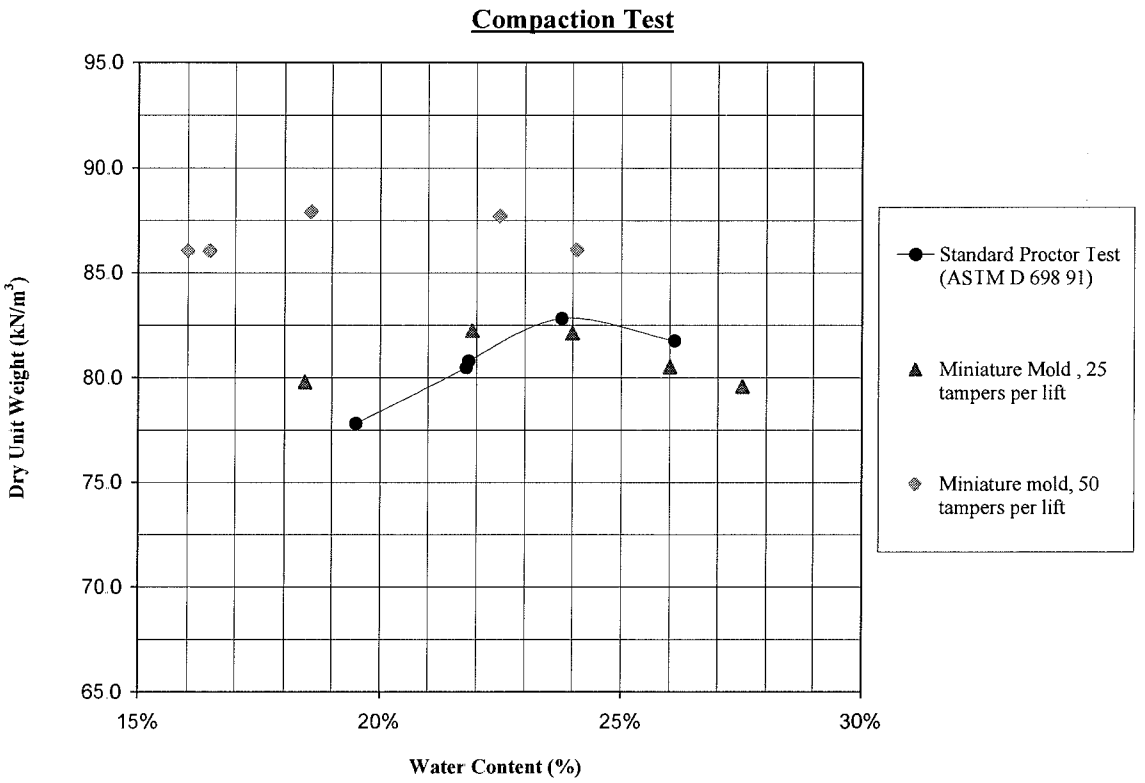

Figure 2.1 Calibration of Compaction Effort for Harvard Miniature Samples

Immediately after compaction, each sample was mounted in the triaxial chamber with dry drainage lines. Oven dried porous stones were placed at the two ends of the sample and the membrane was installed. A small vacuum pressure (5 to 10 psi) was applied to the top of the sample and kept for at least two hours to remove some air out of the sample. The dimensions of the sample were measured once more after the application of vacuum. The bottom drainage valve was then opened to let distilled de-aired water flow into the sample from bottom to top. While the water was drawn into the sample the vacuum pressure was allowed to decrease by 1 psi and a cell pressure of 1 psi was applied. The vacuum pressure was kept constant thereafter until the top drainage lines became saturated. The vacuum pressure was then removed. Cell pressure and back pressure were increased simultaneously with a maximum step size of 2 psi. Each sample was kept under 15 psi or 20 psi back pressure for a few days with a relatively low pressure gradient to keep water flowing from bottom to top. The B-value of each sample was measured during this time to inspect degree of saturation. Samples with B-value greater than 0.97 were considered fully saturated. Whenever the minimum B-value of 0.97 was not achieved in few days, the back pressure was increased to speed up saturation process. The average time needed to saturate the samples varied from 24 hrs for 85% compacted samples to one week for 105% compacted samples.

2.1.2 Wet Pouring Method

Samples were made in several layers. For each layer about 20 grams of dry fly ash was poured into a 500 ml flask. Distilled water was added into the flask to raise the water level at about 0.5" above the fly ash layer. The mix was boiled for approximately 20 minutes to minimize dissolved

air. After the temperature of the mix decreased to room temperature, the flask was filled with distilled de-aired water. A split miniature mold with a stretched membrane inside it was installed on the bottom cap of a triaxial chamber. The mold was filled with distilled de-aired water and a saturated porous stone was placed at the bottom. To make the first layer of the sample, the flask was turned upside-down and the tip was placed inside the mold at about one inch above the bottom to allow fly ash to settle. The rest of the layers were made in a similar manner by placing the tip of the flask one inch above the previous layer, except the last layer (usually the fourth layer was the last one) for which the tip was placed level to the mold top. Since the material was very fine, each layer of fly ash was given at least two hours to settle. Finally the top porous stone and cap were installed and 5 psi vacuum pressure was applied to the sample. Then the mold was removed by splitting and the dimensions of the sample were measured. Sample weight was determined by subtracting the weight of leftover material from the total weight of material that had initially been poured into the flasks. The weight of the sample was double checked after the accomplishment of cyclic and undrained triaxial tests. When the sample was removed from the triaxial chamber, efforts were made to avoid losing any materials while removing the membrane. The sample was weighed, oven dried and weighed again to determine dry weight and moisture content. One advantage of wet pouring method is that the placed sample is saturated and can be tested immediately.

2.1.3 Cyclic Triaxial Test

In order to apply extensional loads to the samples, the existing triaxial chambers were modified by attaching a loading rod to the aluminum top cap using a threaded stud. The cyclic triaxial tests

(ASTM D 5311, see Appendix C) were performed using an MTS hydraulic load frame with dynamic capabilities controlled by an MTS Test Star Controller. The triaxial cell loading rod was connected to the cyclic loading actuator with a custom-made connection. This connection, the modified loading rod, and aluminum top caps were designed and made in the Physics Machine Shop at The Ohio State University. A 100 lb load cell was installed between the connection and the attachment to measure deviator load. An LVDT was attached on the loading rod to measure and record sample axial deformations.

For each test a saturated sample was consolidated under the desired effective confining stress by closing the drainage valves, increasing the cell pressure, and opening the bottom drainage valve, thereafter. In order to compensate for the rod uplift force, a mechanical force equal to the cell pressure times the cross-section area of the rod was applied to the rod. Sample axial deformation and the volume of water squeezed out during consolidation were measured. The samples were consolidated by draining water from the bottom, while the water pressure was being monitored at the top to measure the excess pore water pressure dissipation. Due to the high permeability of the samples (of the order of 10^{-4} cm/sec) the primary consolidation typically took less than 15 seconds. The triaxial chamber then was mounted into the load frame and the cyclic test was conducted in a stress-control mode. During the test, cell pressure was monitored and sample pore water pressure and deformation, as well as the deviator load were recorded continuously with a sampling rate of 100 Hz. The water pressure was measured at the bottom of the sample.
The applied cyclic load was a full sine wave cycling around the zero load as specified in ASTM D 5311. Various effective stresses and shear stress ratios were selected to develop cyclic strength

curves. The loading frequency was selected to be 0.5 Hz except for one case where a frequency of 1 Hz was used.

Each sample was designated with a sample ID which indicates its relative density, initial confining pressure, and cyclic stress ratio. For instance, "85C-20-13" means the sample was compacted at 85% of maximum dry density, consolidated under 20 psi effective confining pressure, and tested at a 0.13 cyclic stress ratio.

During the cyclic tests, sample pore water pressure increased with a rate that was a function of cyclic stress ratio, relative density, and effective confining pressure. Liquefaction was identified as the excess pore water pressure reaching an asymptotic level of the initial effective confining pressure accompanied with a dramatic increase in the axial deformation (Figure 2.2).

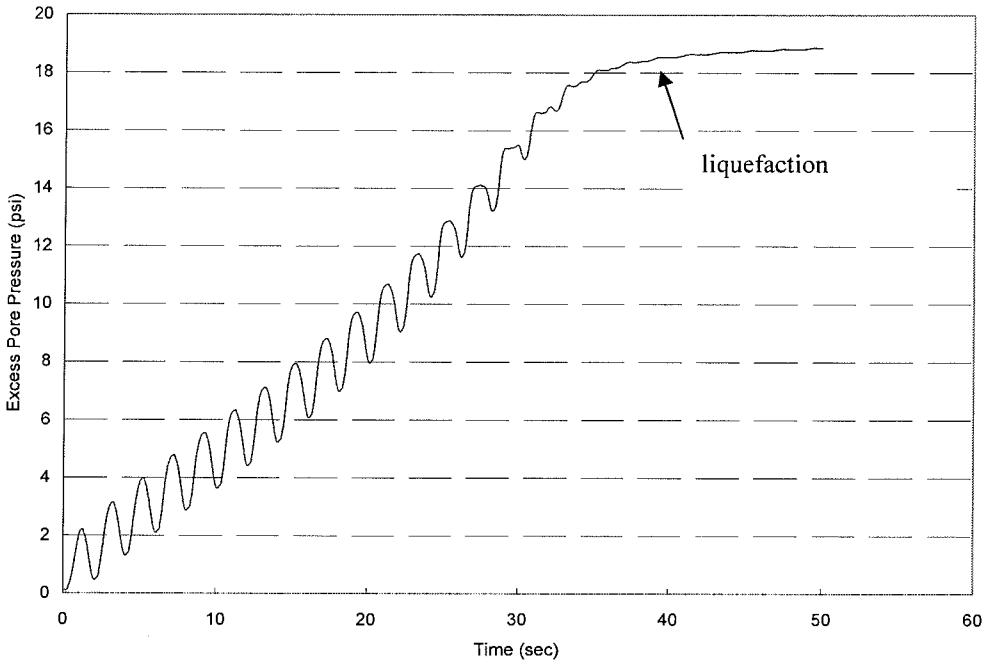

Figure 2.2 Identification of Liquefaction for Cyclic Traxial Tests

2.1.4 Consolidated Undrained Shear Test

The undrained shear strength of the samples was measured after liquefaction. These tests were performed in accordance with the ASTM 4767 using a strain control Instron load frame. Axial deformation and load were measured by the internal LVDT and load cell of the frame and collected by the controlling software at a sampling rate of 1 Hz. Sample pore water pressure was collected simultaneously on a separate computer using a National Instruments data acquisition system.

2.2 Ground Response Analyses

Ground response analysis was used to predict the ground surface motions and estimate the earthquake-induced stresses and strains for evaluation of liquefaction potential for a design earthquake input motion. This section describes the steps involved in the one-dimensional equivalent linear ground response analysis using a widely used computer program SHAKE.

2.2.1 Equivalent Linear Approximation and SHAKE

Ground response analysis is typically performed by either equivalent linear analysis or nonlinear analysis. In an equivalent linear analysis, the soil stiffness and damping characteristics are adjusted until they are compatible with the level of strain induced in the soil. In a nonlinear analysis, the non-linear stress-strain behavior of soil is considered by integrating equations of motion in small time steps. Both methods have been used successfully for ground response analysis while the equivalent linear analysis approach is generally more computational efficient (Kramer, 1996). The one-dimensional equivalent linear approach has been coded into a widely used ground response analysis computer program called SHAKE.

2.2.2 Numerical Analysis

The one-dimensional equivalent linear ground response analysis was carried out using SHAKE for two critical sections. The analysis procedure includes the following general steps:

1. Site Characterization

One or more critical profiles are developed for the site based on the results of laboratory and subsurface investigation programs. Site characterization includes thickness, and unit weight for each soil layer present at the site, and estimates of the dynamic soil properties (shear modulus or shear velocity, modulus reduction and damping models).

2. Selection of Earthquake Input Motions

Appropriate earthquake (natural or synthetic) input motions are selected or developed to represent the design bedrock motion for the site. Each input motion includes a suite of seismological parameters (e.g., peak acceleration, time step, cut off frequency).

3. Ground Response Analysis with SHAKE

Ground response analysis is conducted using SHAKE with the prepared input parameters (site characteristics and input motion). Output from the program typically includes the time histories of acceleration, velocity, displacement, shear strain, and shear stress on the top of layers of interest.

4. Liquefaction Potential Evaluation

The liquefaction potential then can be evaluated by comparing the earthquake loading in terms of equivalent number of uniform stress cycles and cyclic stress ratio with the liquefaction resistance obtained from laboratory tests expressed in cyclic strength curves.

Chapter 3 Results and Discussion

The complete laboratory test results are presented in Appendix A (Figures A.1 through A.45). The detailed ground response analyses results can be found in Appendix B. A summary and discussion of results of the ground response analysis and laboratory tests are presented in this chapter.

3.1 Ground Response Analysis

Two soil profiles are developed for the site based on the results of laboratory and subsurface investigation programs provided by AEP. Site characterization includes estimate of dynamic soil properties (shear modulus or shear velocity, modulus reduction and damping models), thickness, and unit weight for each soil and fly ash layer present at the site. The two soil profiles and dynamic soil properties were shown in the Tables 3.1-3.2 and Figures 3.1-3.2, respectively.

Based on wave propagation theory, the ground motion amplitude depends on the shear modulus (G) or shear wave velocity (V_S) of near-surface materials. Measurements of the shear velocity profile using seismic geophysical tests are generally considered the most reliable way to evaluate the in-situ shear modulus using the following equation:

$$G_{\max} = \rho V_s^2 \tag{3.1}$$

where $G_{\max}$ is maximum shear modulus and ρ is the density.

Since the shear velocity measurements are not available in this study, the maximum shear modulus of each layer was estimated based on empirical relationships in literature. The maximum shear modulus of sand was estimated as

$$G_{\max} = 1000 K_{2,\max} (\sigma_m')^{0.5} \tag{3.2}$$

where $K_{2,\max}$ is determined from the void ratio or relative density and σ_m' is mean principal effective stress in lb/ft^2 (Seed and Idriss, 1970). For fine grain materials, the maximum shear modulus was obtained based on the undrained shear strength and the subsurface investigation results (Kramer, 1996; Seed and Idriss, 1970). The maximum shear modulus of the bedrock was estimated based on the typical shear wave velocity of sandstone (Burger, 1992).

The shear modulus of soil is known to be strain dependent. The shear modulus decreases as the strain amplitude increases. The damping ratio characterizes the energy dissipation during earthquake-induced stress wave propagation. In most engineering applications, standard curves for various basic soil types are available although site specific curves can be derived from laboratory tests and back-analysis (Kramer, 1996). In this study, standard curves were chosen based on the soil type (Tables 3.1-3.2). Experimental studies on a broad range of materials have shown that the shape of both modulus reduction and damping curves are influenced by the plasticity index (Kramer, 1996). Since no specific curves for fly ash materials are available, the curves developed for sands were selected for approximating fly ash material because of its low plasticity.

The dry unit weight has relatively little variation with depth compared with the shear modulus. The unit weight of each layer was determined based on the given subsurface investigation results or assumed depending on the material type. The depths of ground water table for the two soil profiles were given by AEP as observed in the ground water monitoring well data.

Table 3.1 Site Characteristics of Soil Profile A-A'

Layer Number	Material Description	Thickness (ft)	Unit Weight (pcf)	Gmax (ksf)	Vs (ft/sec)	Modulus Reduction	Damping Curve
1	Recompacted Clay Liner	10	125	3,885	1,000	Clay (Seed and Sun 1989)	Clay (Idriss 1990)
2	Drainage layer	8	125	3,300	921	Sand (Seed & Idriss) - Average	Sand (Seed & Idriss) Average
3	Fly ash	10	100	1,000	567	Sand (Seed and Idriss 1970)	Sand (Idriss 1990)
4	Fly ash	10	100	1,200	621	Sand (Seed and Idriss 1970)	Sand (Idriss 1990)
5	Fly ash	18	100	1,400	671	Sand (Seed and Idriss 1970)	Sand (Idriss 1990)
6	Fly ash	30	100	1,600	717	Sand (Seed and Idriss 1970)	Sand (Idriss 1990)
7	Fly ash	30	100	1,800	761	Sand (Seed and Idriss 1970)	Sand (Idriss 1990)
8	Fly ash	30	100	1,900	781	Sand (Seed and Idriss 1970)	Sand (Idriss 1990)
9	Fly ash	30	100	2,000	802	Sand (Seed and Idriss 1970)	Sand (Idriss 1990)
10	Sandstone	Infinite	140	135,360	5,577	Linear	Linear

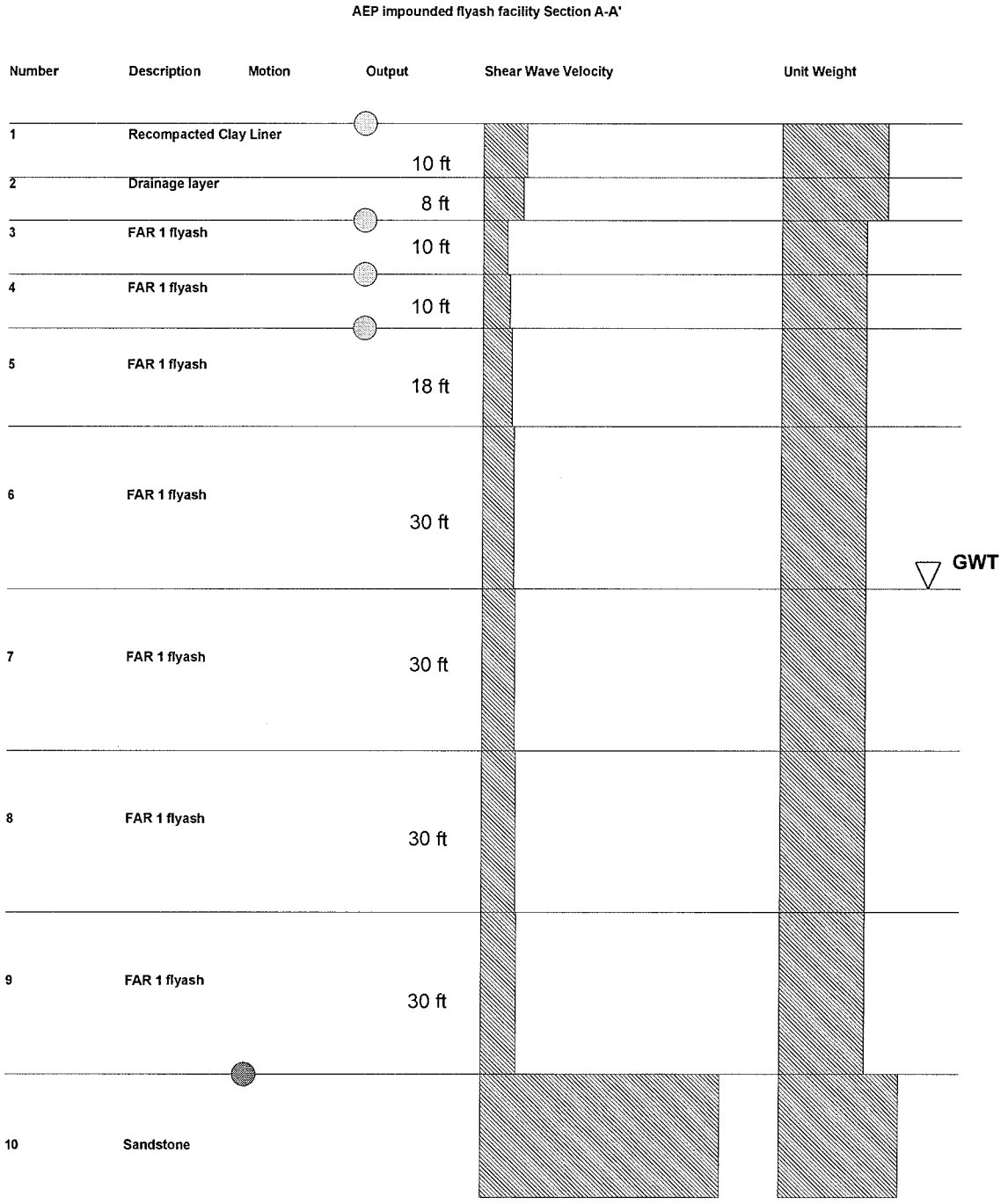

Figure 3.1 Soil Profile A-A'

Table 3.2 Site Characteristics of Soil Profile B-B'

Layer Number	Material Description	Thickness (ft)	Unit Weight (pcf)	Gmax (ksf)	Vs (ft/sec)	Modulus Reduction	Damping Curve
1	Recompacted Clay Liner	18	125	3,885	1,000	Clay (Seed and Sun 1989)	Clay (Idriss 1990)
2	Drainage layer	8	125	4,000	1,014	Sand (Seed & Idriss) - Average	Sand (Seed & Idriss) - Average
3	Fly ash	10	100	1,000	567	Sand (Seed and Idriss 1970)	Sand (Idriss 1990)
4	Fly ash	10	100	1,200	621	Sand (Seed and Idriss 1970)	Sand (Idriss 1990)
5	Fly ash	20	100	1,400	671	Sand (Seed and Idriss 1970)	Sand (Idriss 1990)
6	Fly ash	20	100	1,600	717	Sand (Seed and Idriss 1970)	Sand (Idriss 1990)
7	Fly ash	32	100	1,800	761	Sand (Seed and Idriss 1970)	Sand (Idriss 1990)
8	Sandstone	Infinite	140	135,360	5,577	Linear	Linear

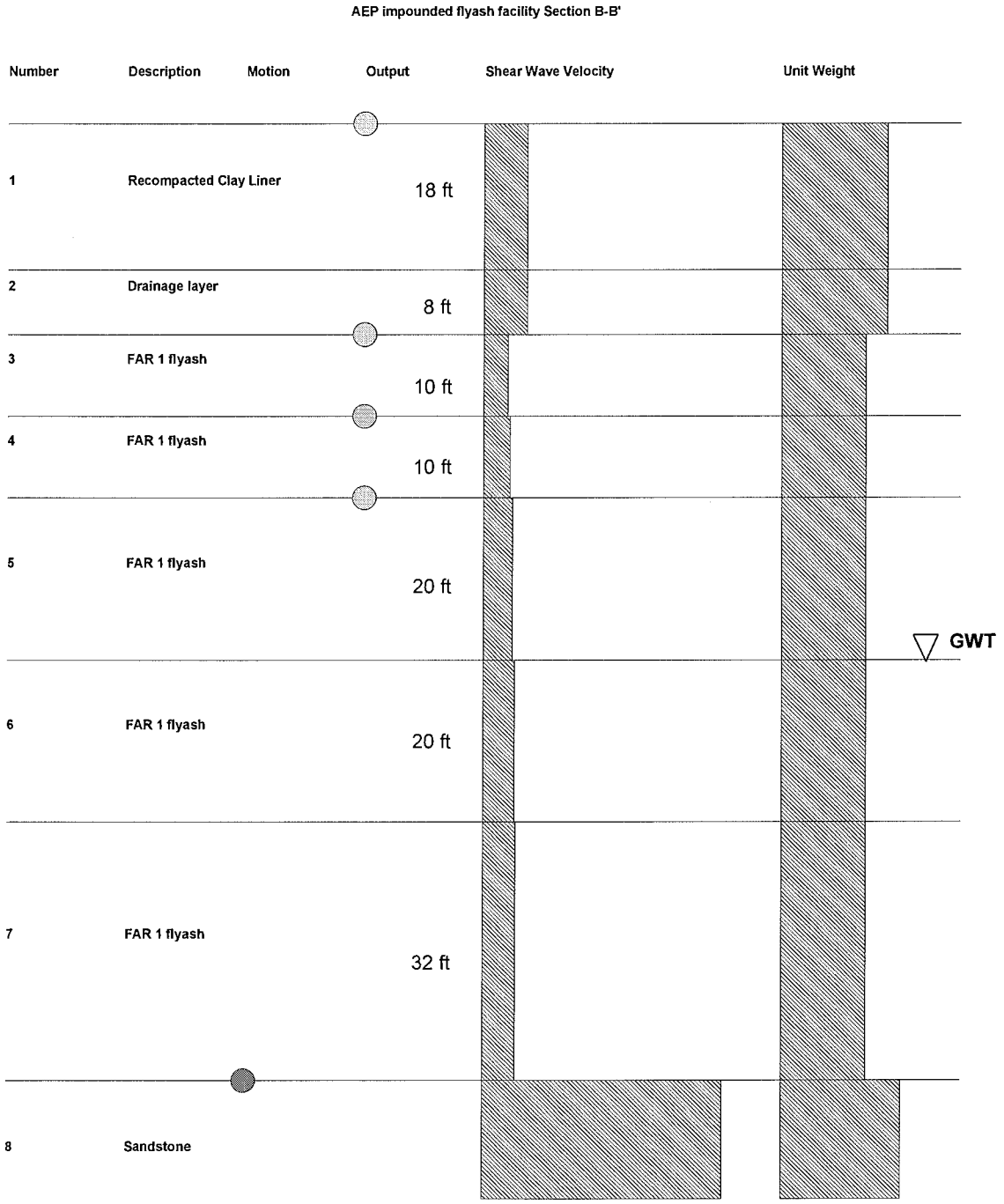

Figure 3.2 Soil Profile B-B'

Two natural earthquake input motions, El Centro and Taft, were selected to represent the design bedrock motion for the site. Each input motion includes a suite of seismological parameters (e.g., peak acceleration, time step, cut off frequency). The peak accelerations of the input motions were scaled to match the design acceleration specified by AEP as 0.08g and 0.15g.

Eight analyses were performed with two selected input motions and design peak acceleration (Table 3.3). Output from the program included the time histories of acceleration, velocity, displacement, shear strain, and shear stress on the top three fly ash layers and ground surface. The positions of output are shown as green circles in Figures 3.1 and 3.2.

Table 3.3 Input Earthquake Motions

Analysis #	Site Profile	Earthquake Input Motion	Peak Acceleration
A1	A-A'	Taft	0.08 g
A2	A-A'	Taft	0.15 g
A3	A-A'	El centro	0.08 g
A4	A-A'	El centro	0.15 g
B1	B-B'	Taft	0.08 g
B2	B-B'	Taft	0.15 g
B3	B-B'	El centro	0.08 g
B4	B-B'	El centro	0.15 g

The common cyclic stress approach was used for liquefaction potential evaluation. In the cyclic stress approach, the earthquake-induced loading is compared with liquefaction resistance of the soil expressed in terms of cyclic shear stresses (Kramer, 1996). The transient and irregular time history of earthquake-induced shear stresses obtained from the ground response analyses were converted into an equivalent series of uniform stress cycles in order to compare with the cyclic strength determined in laboratory tests. Based on the work of Seed et al. (1975a), the equivalent number of uniform stress cycles (N_{equ}) was determined by counting the stress cycles with amplitude greater than 65% of the peak cyclic shear stress ($\tau_{\max}$) for a particular shear stress time history as:

$$\tau_{cyc} = 0.65\tau_{\max} \tag{3.3}$$

Although different stress levels have been developed (e.g., Halder and Tang, 1981), 65% is most commonly used (Kramer, 1996). The uniform shear stress is typically normalized by the initial overburden stress to produce a cyclic stress ratio (CSR):

$$CSR = \frac{\tau_{cyc}}{\sigma_0'} \tag{3.4}$$

Earthquakes generally produce shear stresses in different directions. Pyke et al. (1975) showed that multidirectional shaking can cause pore water pressure to increase more rapidly than single unidirectional shaking. Seed et al. (1975b) suggested that the CSR required to produce initial liquefaction in field was about 10% less than the laboratory obtained values. Therefore, equivalent number of uniform stress cycles and corrected CSR' were compared with the liquefaction resistance obtained from laboratory tests expressed in cyclic strength curves as:

$$CSR' = 1.1CSR \tag{3.5}$$

The ground response analyses results are summarized in Table 3.4. The predicted maximum the cyclic stress ratio of 0.14 was obtained from the analysis on the B-B' profile with Taft earthquake input motion at a peak acceleration of 0.15 g.

Table 3.4 Summary of the Results from Ground Response Analyses

Parameters	Layer #	depth(ft)	σ_0'(psf)	τ_{max}(psf)	τ_{cyc} (psf)	N_{equ}	CSR	CSR'
A-A'	3	18	2250	310	202	4	0.09	0.10
Taft	4	28	3250	436	283	4	0.09	0.10
a_{max}=0.08g	5	38	4250	536	348	4	0.08	0.09
A-A'	3	18	2250	397	258	6	0.11	0.13
Taft	4	28	3250	556	361	6	0.11	0.12
a_{max}=0.15g	5	38	4250	682	443	6	0.10	0.12
A-A'	3	18	2250	279	181	8	0.08	0.09
El Centro	4	28	3250	382	248	8	0.08	0.08
a_{max}=0.08g	5	38	4250	458	298	8	0.07	0.08
A-A'	3	18	2250	386	251	6	0.11	0.12
El Centro	4	28	3250	536	348	6	0.11	0.12
a_{max}=0.15g	5	38	4250	655	426	6	0.10	0.11
B-B'	3	26	3250	407	265	6	0.08	0.09
Taft	4	36	4250	500	325	6	0.08	0.08
a_{max}=0.08g	5	46	5250	541	352	6	0.07	0.07
B-B'	3	26	3250	620	403	5	0.12	0.14
Taft	4	36	4250	755	491	5	0.12	0.13
a_{max}=0.15g	5	46	5250	806	524	5	0.10	0.11
B-B'	3	26	3250	393	255	6	0.08	0.09
El Centro	4	36	4250	494	321	5	0.08	0.08
a_{max}=0.08g	5	46	5250	552	359	6	0.07	0.08
B-B'	3	26	3250	552	359	8	0.11	0.12
El Centro	4	36	4250	647	421	8	0.10	0.11
a_{max}=0.15g	5	46	5250	717	466	8	0.09	0.10

3.2 Laboratory Tests

3.2.1 Cyclic Triaxial Tests

Figure 3.3 shows the cyclic strength curves derived from the laboratory cyclic triaxial tests (See Table 3.5). As can be seen, the number of loading cycles to produce liquefaction decreases with increasing shear stress ratio and with decreasing density. This relationship between the numbers of cycles to liquefaction, density and cyclic stress ratio is also presented in Figure 3.4. Figure 3.5 compares the design earthquake loading predicted from the numerical analysis with the cyclic strength curves obtained from laboratory tests. In Figures 3.3 and 3.5, the solid lines demonstrate suggested curves for 20 psi effective confining pressure for three different relative densities of 85%, 95%, and 105%. The laboratory test results also indicated that the initial confining stress has a noticeable effect on the liquefaction behavior of fly ash material. When the samples with the same density were tested under the same CSR, the samples with lower effective confining stress level demonstrated higher liquefaction resistance. The two dashed lines in Figures 3.3 and 3.5 show the suggested curves for the test results from the samples with 95% relative density and consolidated at 10 and 50 psi confining pressure, respectively. Therefore, the most critical earthquake loading for liquefaction is the combination of high CSR, high initial confining stress and high equivalent number of cycles.

The predicted CSRs and the corresponding equivalent number of cycles (See Table 3.4) are plotted as open black circles in Figure 3.5. As can be seen, all the calculated earthquake loadings were below the cyclic strength curve of samples with 95% relative density which is the typical relative density in the field based on the subsurface investigation information. In other words, the cyclic loading caused by the design earthquakes was lower than the cyclic strength of the fly ash material. The factor of safety depends on the density, CSR and initial confining pressure.

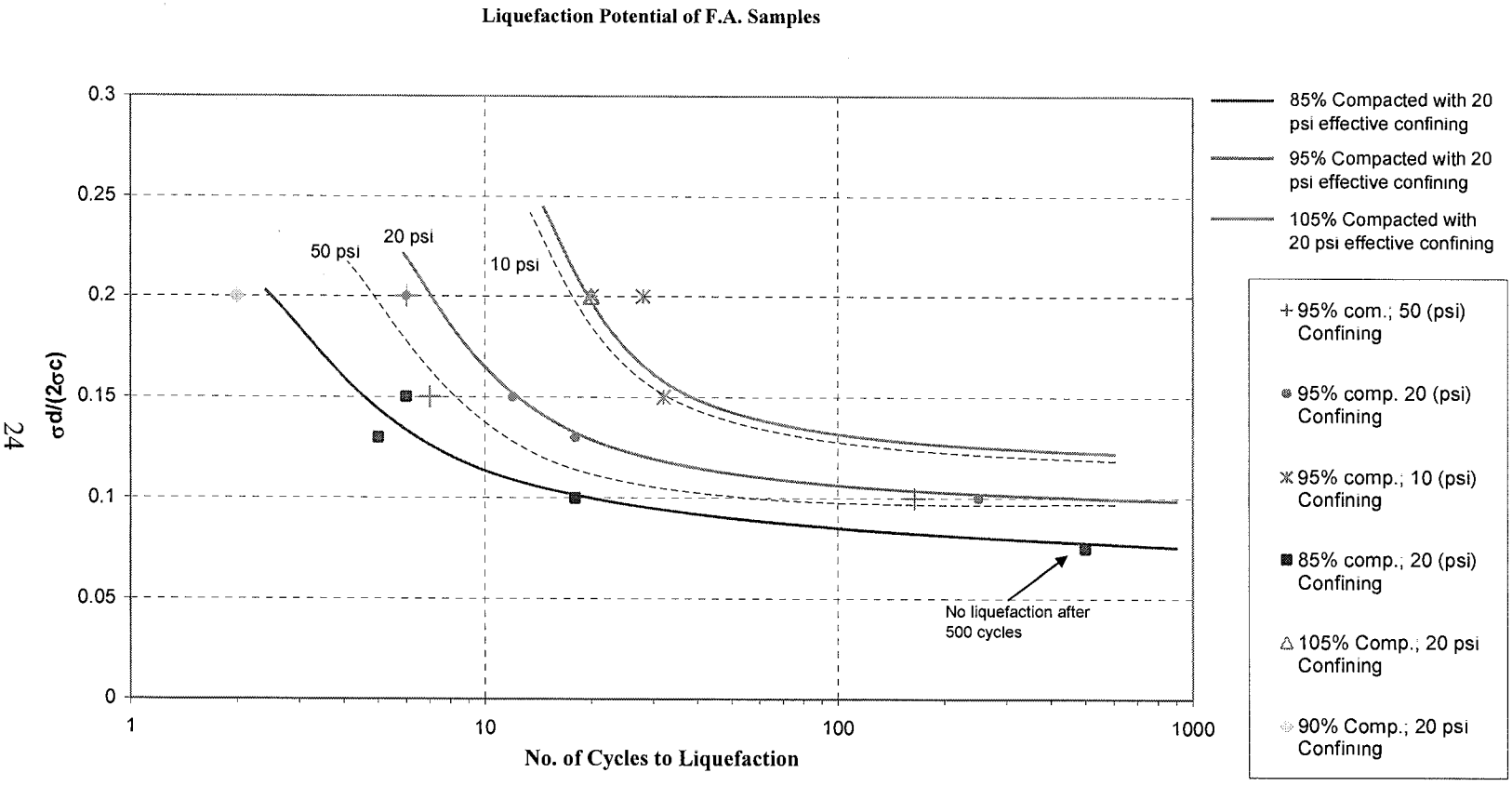

Figure 3.3 Cyclic Strength Curves from Laboratory Tests

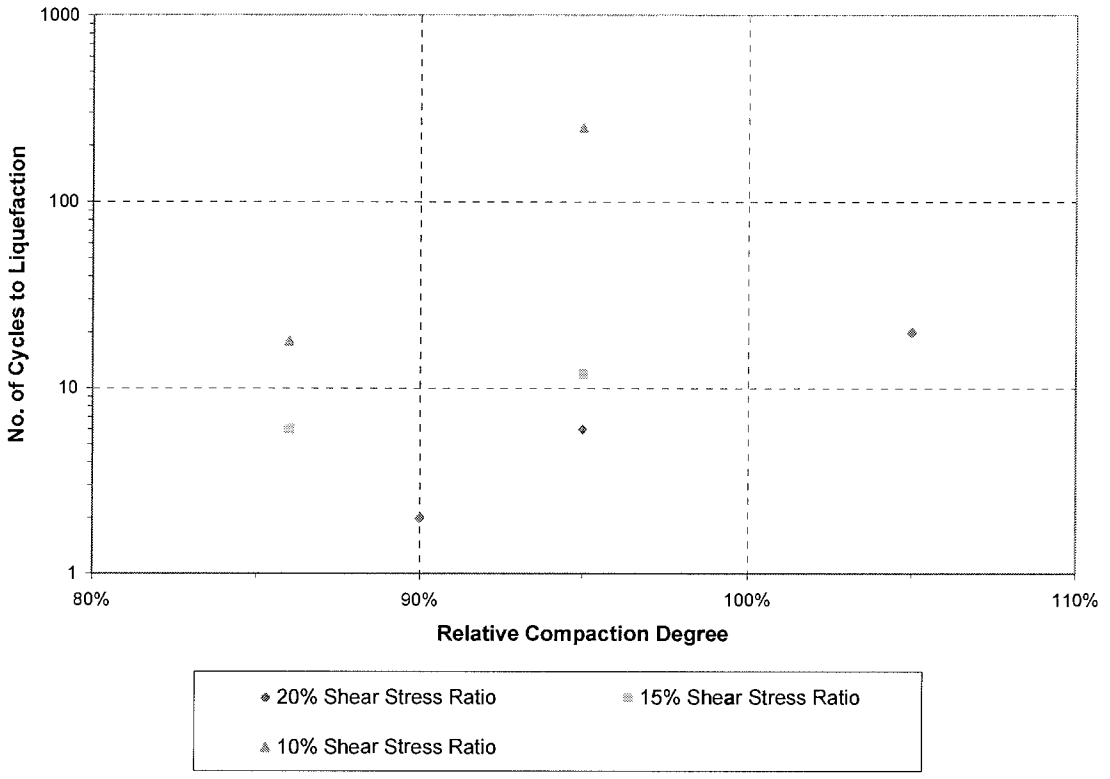

Figure 3.4 Effects of Density and Cyclic Shear Stress Ratio on Number of Cycles to Liquefaction

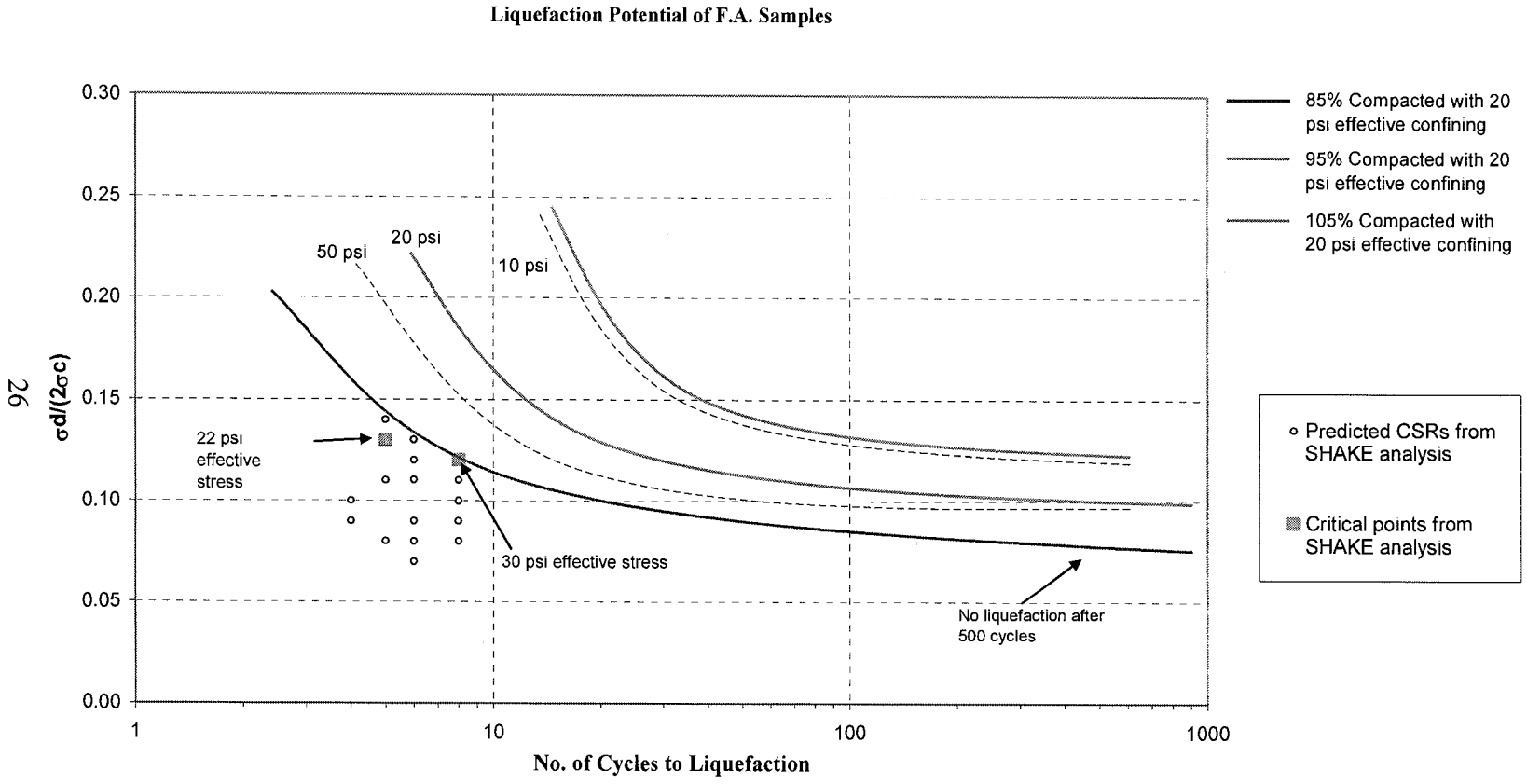

Figure 3.5 Comparison of Design Earthquake Loading and Cyclic Strength Curves

Table 3.5 Summary of Cyclic Triaxial Test Condition and Results

Sample ID	Initial Compaction	Confining Stress (psi)	Shear Stress Ratio	No. of Cycles to Liqu.	Loading Frequency (Hz)	Compaction Method	Notes
85P-10-10	87%	10	10%	N.L.	0.5	Pouring	Didn't liquefy after 500 cycles
85C-20-10	86%	20	10%	18	0.5	Wet tamp	
85C-20-8	87%	20	7.5%	>500	0.5	Wet tamp	
85C-20-15	86%	20	15%	6	0.5	Wet tamp	Due to excessive deformation post liquefaction CU wasn't conducted
85C-20-13	85%	20	13%	5	0.5	Wet tamp	
90C-20-20	89%	20	20%	2	0.5	Wet tamp	
95C-20-10	95%	20	10%	250	0.5	Wet tamp	
95C-10-20a	95%	10	20%	28	0.5	Wet tamp	Due to excessive deformation post liquefaction CU wasn't conducted
95C-10-20b	95%	10	20%	20	0.5	Wet tamp	
95C-50-20	95%	50	20%	6	0.5	Wet tamp	Due to excessive deformation post liquefaction CU wasn't conducted
95C-50-10	95%	50	10%	165	0.5	Wet tamp	
95C-20-15	95%	20	15%	12	1.0	Wet tamp	Due to excessive deformation post liquefaction CU wasn't conducted
95P-20-10	95%	20	10%	N.L.	0.5	Pouring	Didn't liquefy after 500 cycles
95C-50-15	95%	50	15%	7	0.5	Wet tamp	Due to excessive deformation post liquefaction CU wasn't conducted
95C-10-15	95%	10	15%	32	0.5	Wet tamp	
95C-20-20	95%	20	20%	6	0.5	Wet tamp	Excessive deformation after cyclic test- CU done
95C-20-13	95%	20	13%	18	0.5	Wet tamp	
105C-20-20	104%	20	20%	20	0.5	Wet tamp	

3.2.2 Initial and Post Liquefaction CU Tests

Table 3.6 presents a summary of post liquefaction undrained shear test results. In order to perform post-liquefaction CU tests, efforts were made to stop the cyclic tests as soon as the liquefaction occurred to prevent excess sample deformation. However, as shown in Table 3.6, there were six cases when liquefaction happened so dramatically that the sample was severely deformed and it had to be discarded because it was too much deformed to conduct a CU test on it.

The post-liquefaction CU test was performed after the sample was re-consolidated at the initial effective confining stress. In one case (Sample 95C-50-10) sample pore water pressure increased by 5 psi with closed drainage lines before the beginning of undrained shear test. This increase is likely caused by secondary consolidation of the sample under relatively high effective pressure of 50 psi. In general, for most cases the pore water pressure slightly increased (1 psi or less) within 2 to 3 minutes after the drainage lines were closed. Figures 3.6 and 3.7 show examples of two typical deviator stress versus axial strain trends for these samples. The first trend shows a clear initial peak in shear strength at relatively low axial strains (less than 2%). At relatively high axial strains, the shear strength exhibited an increasing trend and it often exceeded the initial peak. The second one does not have a clear peak point and as the axial strain increases the excess pore pressure becomes negative. This trend was commonly observed for samples with higher confining pressures or samples with higher relative density.

Table 3.6 Summary of Post Liquefaction Undrained Shear Test Results

Sample ID	Effective Confining Pressure (psi)	Total No. of Cycles applied	Max Axial Strain Experienced	Undrained Shear Strength						
				Peak Shear Strength			5% Axial Strain		10% Axial Strain	
				τ (psi)	Comp. Axial Strain	Δu (psi)	τ (psi)	Δu (psi)	τ (psi)	Δu (psi)
85P-10-10	10	500	0.036%		No peak		56.1	-26.7	58.2	-25.9
85C-20-10	20	23	-1.1%		No peak		6.5	6.1	9.1	2.4
85C-20-8	20	500	0.7%	2.6	0.49%	7.3	0.64	17.1	0.64	17.2
85C-20-13	20	9	3.6%	2.2	0.54%	7.9	2.1	15.4	4.4	12.4
90C-20-20	20	5	2.2%	3.2	1.15%	11.052	3.2	13.8	3.5	-2.6
95P-20-10	20	500	0.04%		No peak		23.5	-13.4	28.2	-22.8
95C-10-15	10	39	6.3%		No peak		3	5.3	7.1	-0.8
95C-10-20b	10	32	1.3%		No peak		9.7	1.8	9.9	1.8
95C-20-20	20	12	3.9%	1.5	0.64%	10.3	16.5	0.7	15.5	1.1
95C-20-13	20	24	2.9%	2.8	2.00%	11.9	2.1	14.3	2.9	13.4
95C-50-10	50	171	-2.5%		No peak		44.4	-5.1	52.6	-16.3
105C-20-20	20	28	-1.4%		No peak		30.6	-25.8	37.7	-40.9

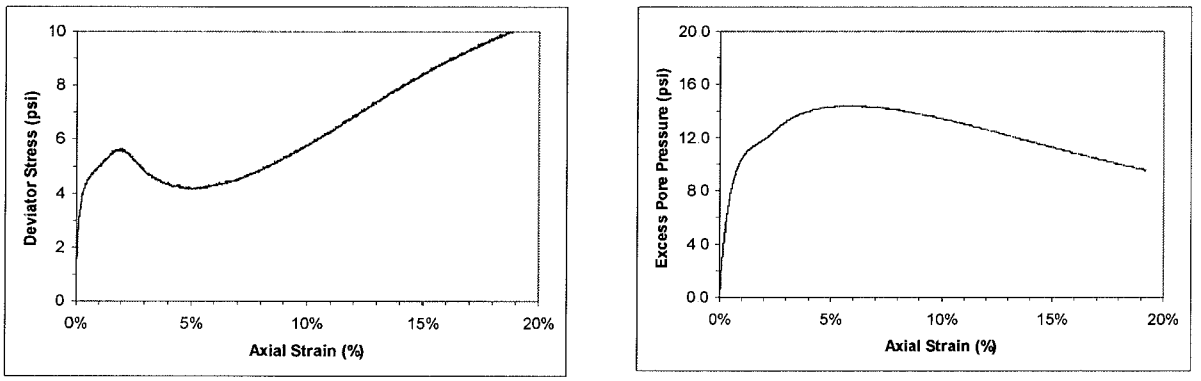

Figure 3.6 Post liquefaction undrained shear test for sample 95C-20-13. (The deviator stress versus axial strain curve shows a peak at relatively low axial strain. For high axial strains the shear strength keeps increasing.)

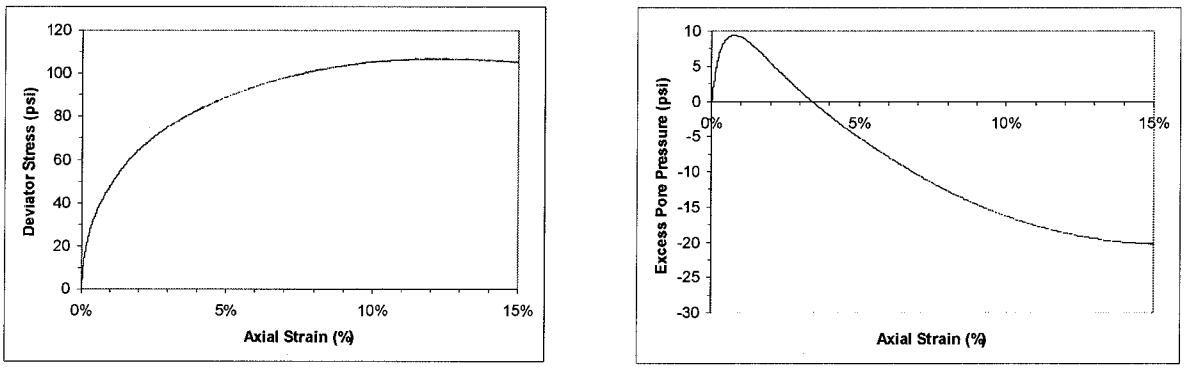

Figure 3.7 Post liquefaction undrained shear test for sample 95C-50-10. (The deviator stress versus axial strain curve does not show a clear peak.)

Table 3.6 also shows the maximum shear strain each sample had experienced during cyclic loading or after the cycles was stopped and the load frame piston returned to the reference position (seating load), as well as the total number of cycles applied. It should be mentioned that the total number of cycles may be greater than the number of cycles to liquefaction presented in Table 3.5 because in most cases cyclic loading was continued for a few cycles after liquefaction point.

Initial Undrained Shear Strength versus Post Liquefaction Shear Strength

Table 3.6 presents a summary of post liquefaction undrained shear test results. Table 3.7 shows initial undrained shear strengths for samples which were not exposed to any cyclic loading (before earthquake condition). Comparison of the values presented in the two tables indicates that in most cases the static undrained shear strength have moderately to highly increased after liquefaction. However there are some exceptions, namely 95C-20-20 and 95C-20-18. For those samples with an initial peak (the pattern presented in Figure 3.5), the post-liquefaction shear strength exhibited an increasing trend for high axial strains, whereas the initial shear strength of the samples approached a residual value and remained almost constant.

Influence of Cyclic Test Variables on Post Liquefaction Shear Strength

The pouring method resulted in samples with significantly higher post liquefaction shear strength. Recall from the previous section that these samples did not liquefy. As expected, the shear strength of the samples prepared by wet tamping increases as the initial compaction degree increases. In general the undrained shear test results exhibit a large scatter, making it difficult to find a trend between testing conditions and post-liquefaction shear strength values.

Table 3.7 Summary of Initial Undrained Shear Test Results†

Sample ID	Back Pressure Prior to Test (psi)	Undrained Shear Strength						
		Peak Shear Strength			5% Axial Strain		10% Axial Strain	
		τ (psi)	Comp. Axial Strain	Δu (psi)	τ (psi)	Δu (psi)	τ (psi)	Δu (psi)
85C-50-CU	20							
90C-20-CU	20							
95C-20-CU	20	3.51	0.8%	9.6	1.02	16.5	0.54	17.5
105C-20-CD	20							

† Note: Test results will be completed in the final version of the report.

Chapter 4 Summary and Conclusions

4.1 Summary

In this study, the liquefaction potential of impounded fly ash material was investigated. Eighteen cyclic triaxial tests (ASTM D5311) were performed on reconstituted samples with different relative density, confining stress, and shear stress ratio. The cyclic shear strength of the fly ash material was presented graphically in terms of cyclic strength curves which show the relationship between density, cyclic stress amplitude, and number of cycles to liquefaction. After cyclic triaxial tests, most of the samples were reconsolidated to the initial effective confining stress and subjected to consolidated undrained (CU) triaxial tests (ASTM 4767) to determine the static undrained shear strength of the fly ash. Additional four CU tests (one for each relative density) were performed to determine the initial static undrained shear strength.

The design seismic loading in terms of cyclic stress ratio and equivalent number of cycles were obtained from ground response analyses using SHAKE. The liquefaction potential of the fly ash material was evaluated based on the comparison of the cyclic strength and design earthquake loading.

4.2 Conclusions

The following conclusions can be made based on the laboratory testing and numerical analysis results:

1. The cyclic loading imposed by the design earthquakes was founded to be lower than the cyclic strength of the fly ash material. The factor of safety depends on the dry unit weight, cyclic stress ratio, and initial confining pressure.
2. The number of loading cycles to produce liquefaction decreases with increasing shear stress ratio and with decreasing dry unit weight.
3. When the samples with the same dry unit weight were tested under the same cyclic stress ratio, the samples with lower effective confining stress level demonstrated higher liquefaction resistance.
4. Typically, the post-liquefaction strength was found to be higher than the initial strength when the cyclic tests were stopped soon after liquefaction without excessive sample deformation.
5. The post-liquefaction undrained shear strength was found to be unrelated to the laboratory testing conditions. This may be due to the inability of being able to stop further cyclic loading right after liquefaction occurs.
6. Sample preparation method was also found to have great effect on the cyclic strength. The samples prepared with wet pouring method exhibited higher liquefaction resistance.

List of References

1. ASTM Designation: ASTM D5311, "*Standard Test Method for Load Controlled Cyclic Triaxial Strength of Soil*", Annual Book of ASTM Standards, 2004, pp. 1167-1176.
2. ASTM Designation: D698, "*Standard Test Method for Laboratory Compaction Characteristics of Soil Using Standard Effort*", Annual Book of ASTM Standards, 2002, pp. 78-85.
3. ASTM Designation: 4767, "Standard Test Method for Consolidated Undrained Triaxial Compression Test for Cohesive Soils", Annual Book of ASTM Standards, 2004, pp. 913-925.
4. Kramer, S.L. (1996). *Geotechnical Earthquake Engineering*, Prentice Hall, Inc., Upper Saddle River, New Jersey, 653 pp.
5. Seed, H. B. and I. M. Idriss "Soil Moduli and Damping Factors for Dynamic Response Analysis". Report No. UCB/EERC-70/10, Earthquake Engineering Research Center, University of California, Berkeley, 1970.
6. Burger, H. R., *Exploration Geophysics of the Shallow Subsurface*, Prentice Hall: Englewood Cliffs, NJ, 1992.
7. Seed, H.B., K. Mori and C.K. Chan, "Influence of Seismic History on the Liquefaction Characteristics of Sands", Report No. UCB/EERC-75/25, Earthquake Engineering Research Center, University of California, Berkeley, 1975a.
8. Seed, H.B., K.L. Lee, I.M. Idriss and F.I. Makdisi, "The Slides in the San Fernando Dams During the Earthquake of February 9, 1971 ", Journal of Geotechnical Engineering Division, ASCE, Vol. 101, No. GT7, pp. 651-688, 1975b.

9. Haldar, A., and W.H. Tang, "Statistical Study of Uniform Cycles in Earthquake Motion", Journal of the Geotechnical Engineering Division, ASCE, Vol. 107, No. GT5, pp. 577-589, 1981.

10. Pyke, R., H.B. Seed and C.K. Chan, "Settlement of Sands under Multidirectional Shaking", Journal of the Geotechnical Engineering Division, Vol. 101, No. GT4, pp. 379-398, 1975.

Appendix A

Laboratory Results

Table A.1 Summary of Post Liquefaction Undrained Shear Test Results

Sample ID	Initial Compaction	Confining Stress (psi)	Shear Stress Ratio	No. of Cycles to Liqu.	Loading Frequency (Hz)	Compaction Method
85P-10-10	87%	10	10%	N.L.	0.5	Pouring
85C-20-10	86%	20	10%	18	0.5	Wet tamp
85C-20-8	87%	20	7.5%	>500	0.5	Wet tamp
85C-20-15	86%	20	15%	6	0.5	Wet tamp
85C-20-13	85%	20	13%	5	0.5	Wet tamp
90C-20-20	89%	20	20%	2	0.5	Wet tamp
95C-20-10	95%	20	10%	250	0.5	Wet tamp
95C-10-20a	95%	10	20%	28	0.5	Wet tamp
95C-10-20b	95%	10	20%	20	0.5	Wet tamp
95C-50-20	95%	50	20%	6	0.5	Wet tamp
95C-50-10	95%	50	10%	165	0.5	Wet tamp
95C-20-15	95%	20	15%	12	1	Wet tamp
95P-20-10	95%	20	10%	N.L.	0.5	Pouring
95C-50-15	95%	50	15%	7	0.5	Wet tamp
95C-10-15	95%	10	15%	32	0.5	Wet tamp
95C-20-20	95%	20	20%	6	0.5	Wet tamp
95C-20-13	95%	20	13%	18	0.5	Wet tamp
105C-20-20	104%	20	20%	20	0.5	Wet tamp

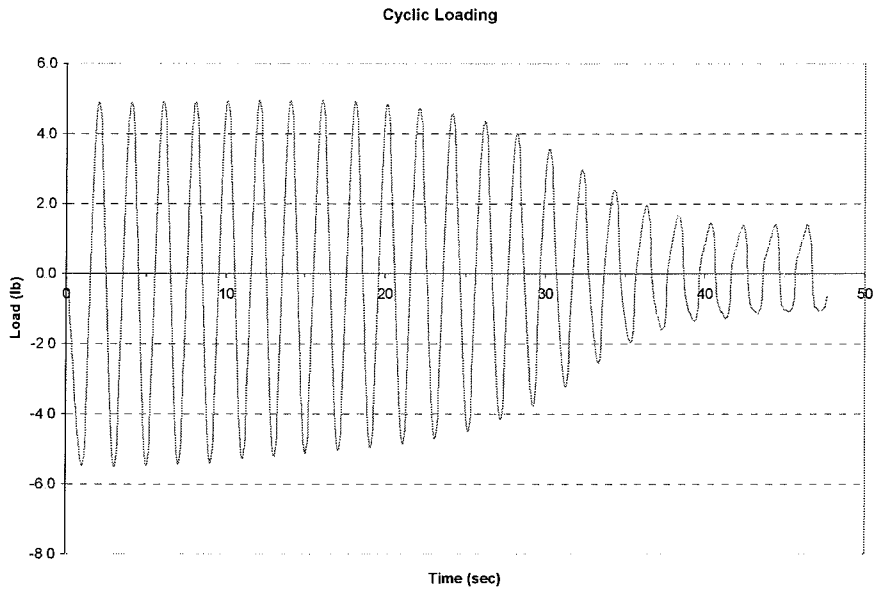

Figure A.1. 85C-20-10 cyclic loading

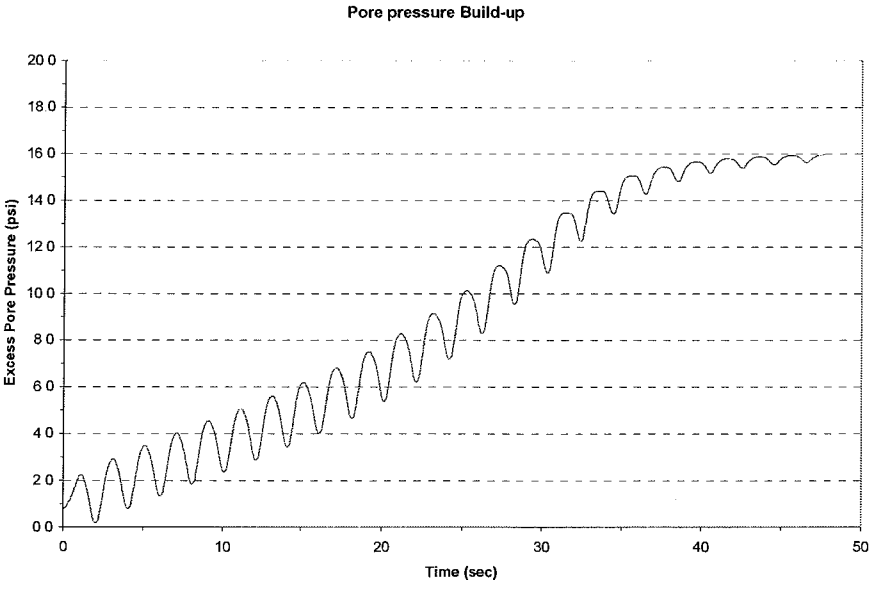

Figure A.2. 85C-20-10 pore water pressure build up

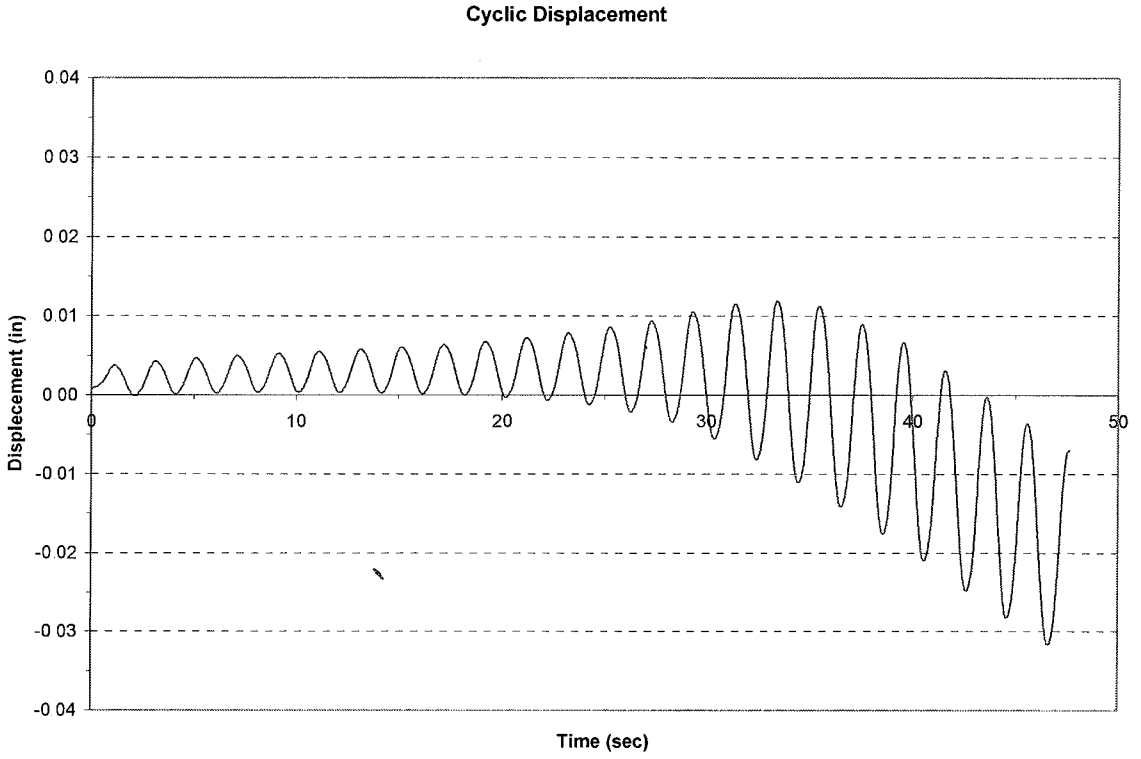

Figure A.3. 85C-20-10 cyclic displacement

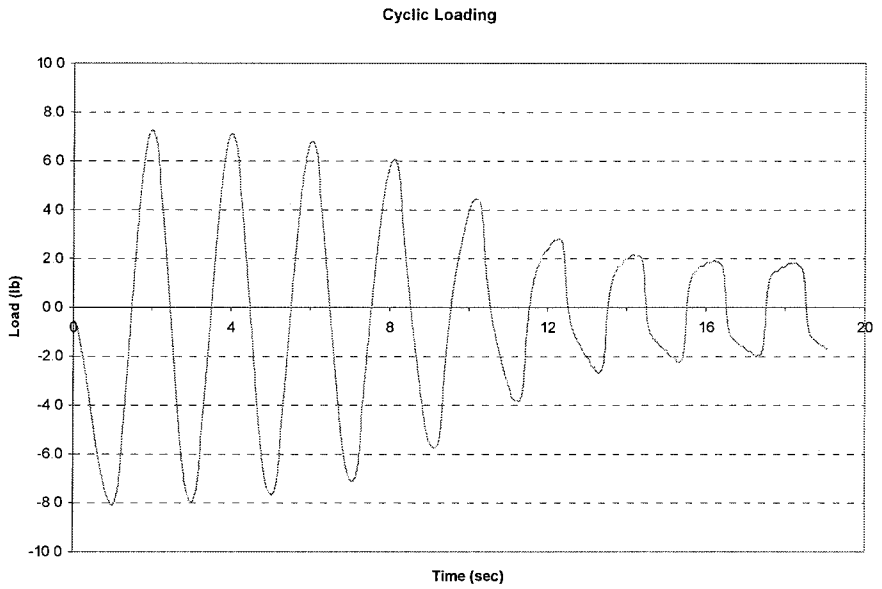

Figure A.4. 85C-20-15 cyclic loading

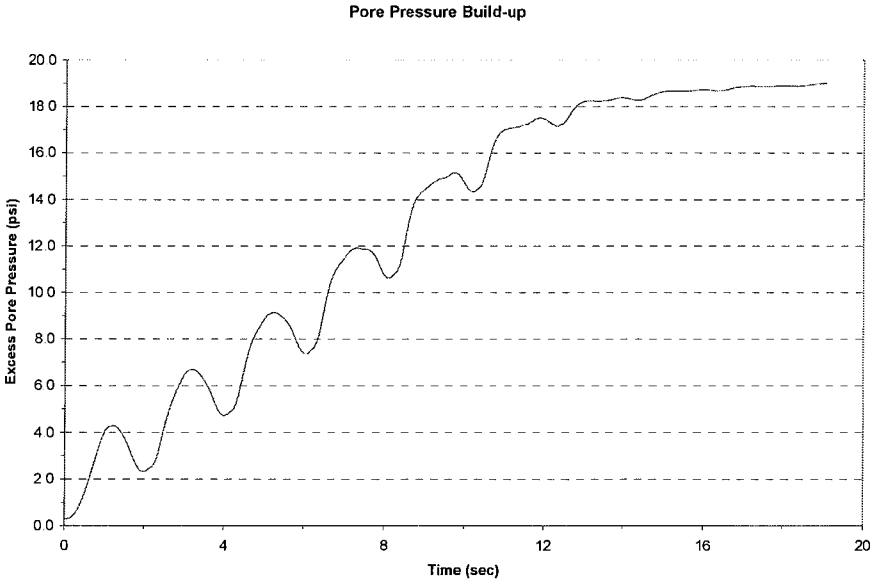

Figure A.5. 85C-20-15 pore water pressure build up

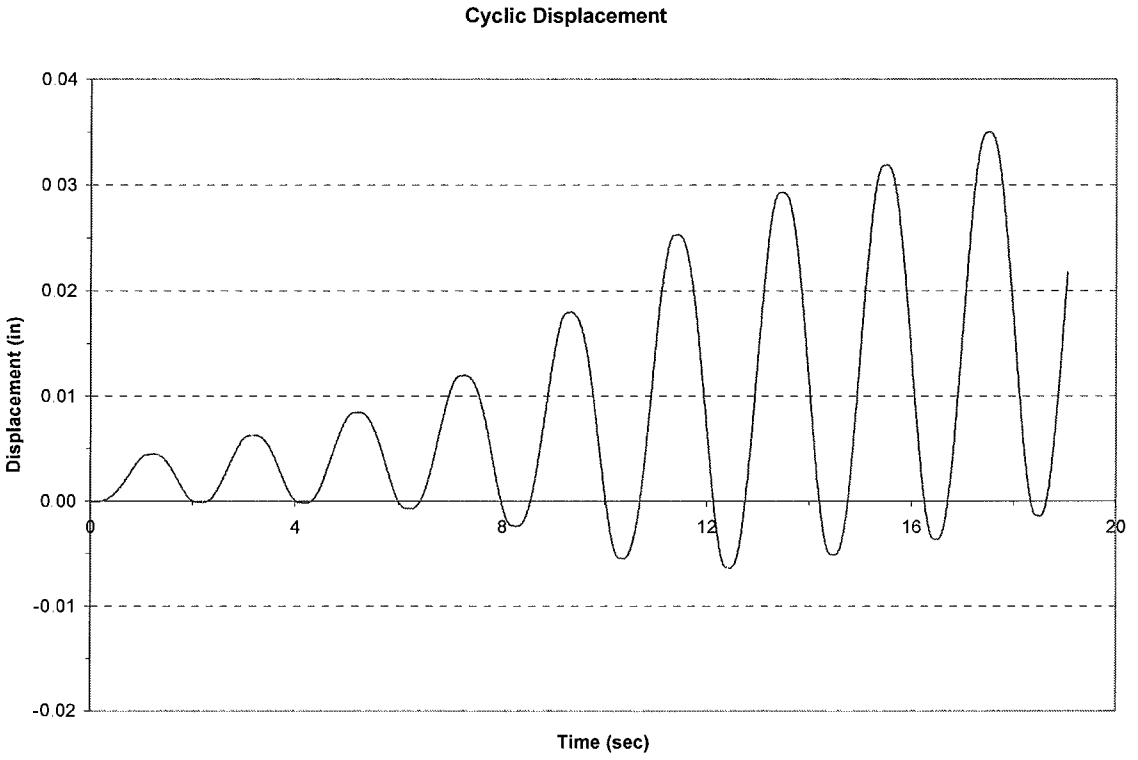

Figure A.6. 85C-20-15 cyclic displacement

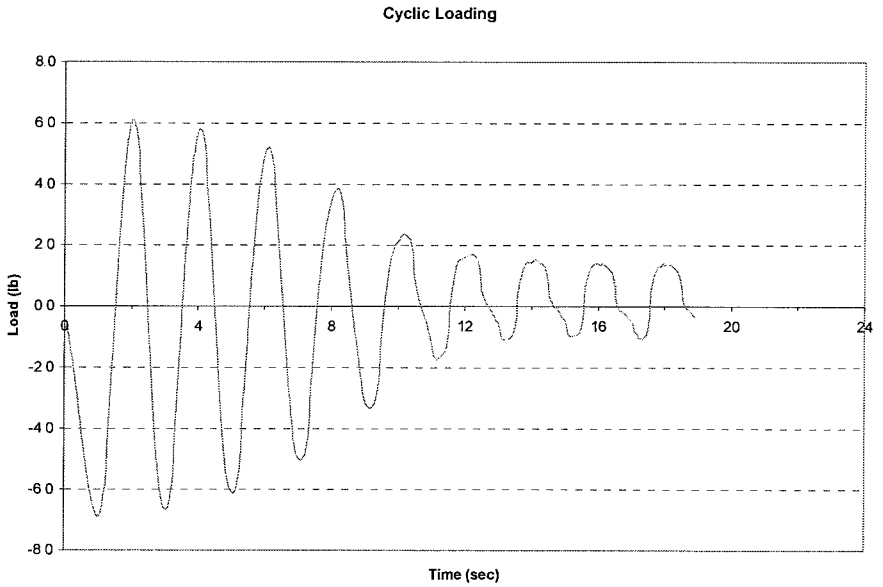

Figure A.7. 85C-20-13 cyclic loading

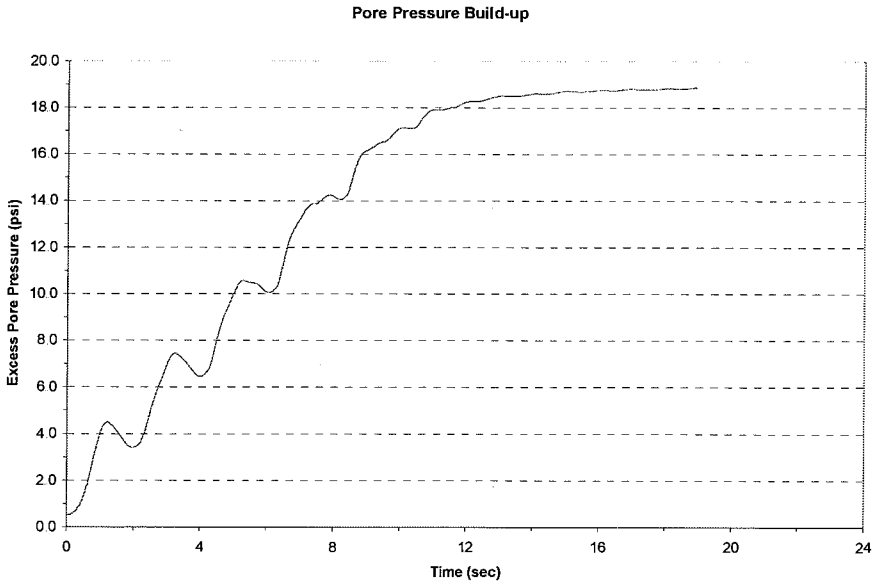

Figure A.8. 85C-20-13 pore water pressure build up

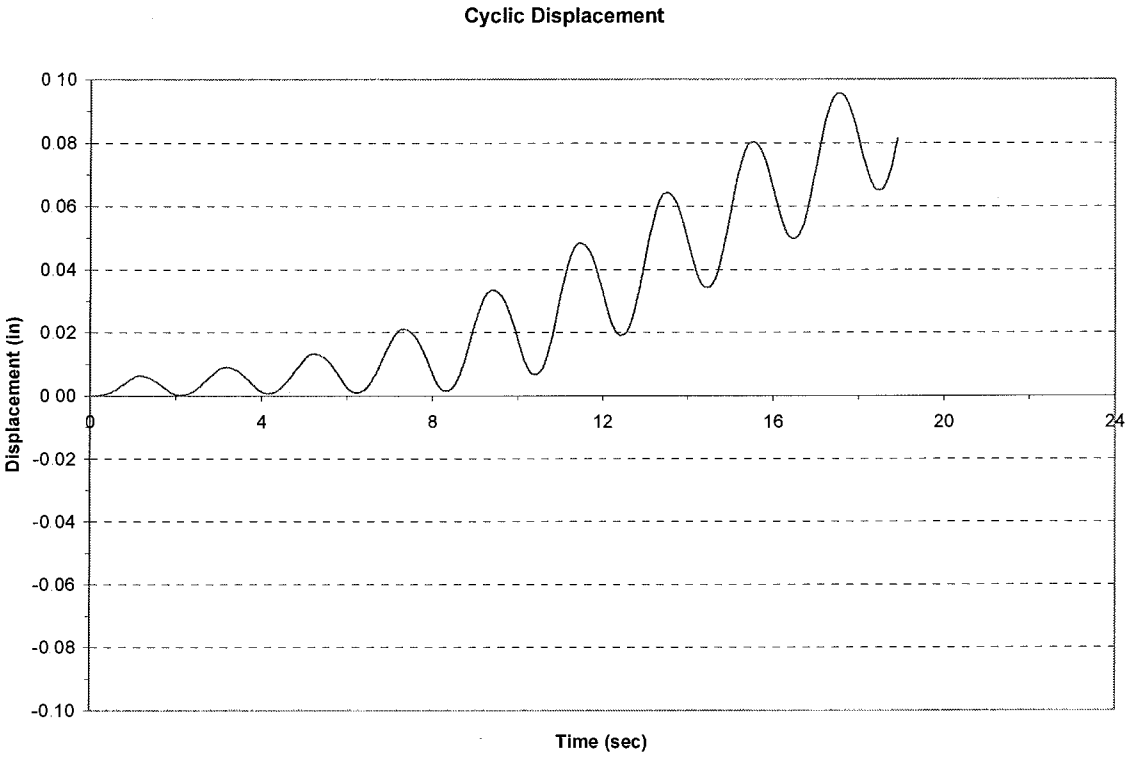

Figure A.9. 85C-20-13 cyclic displacement

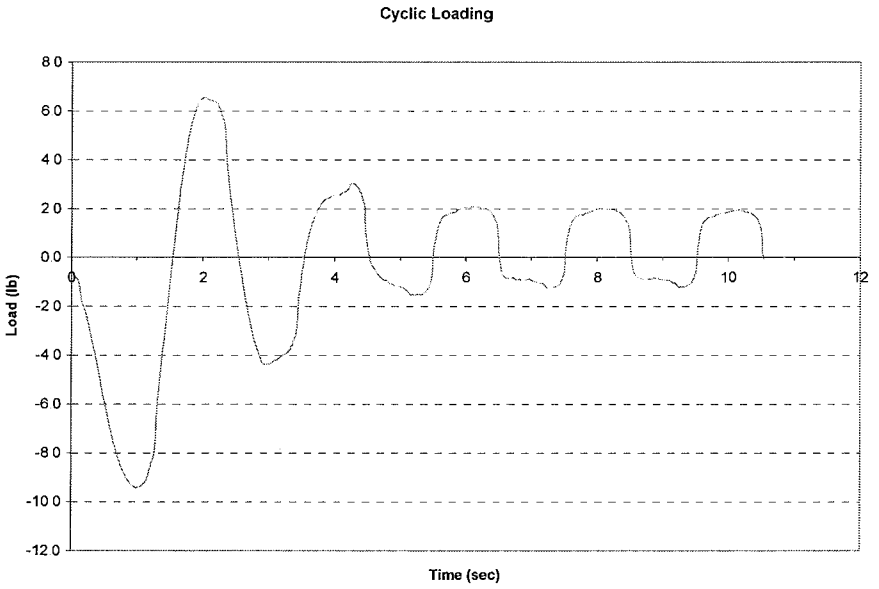

Figure A.10. 90C-20-20 cyclic loading

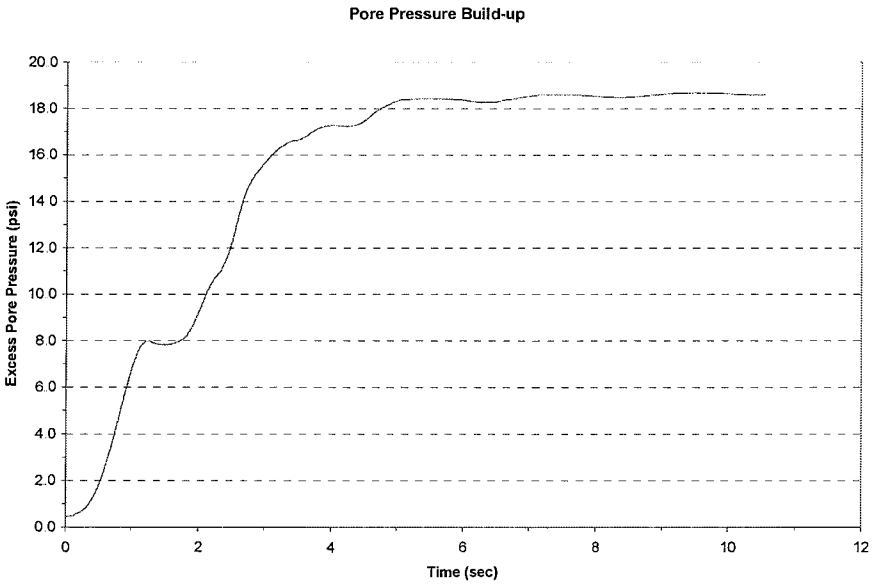

Figure A.11. 90C-20-20 pore water pressure build up

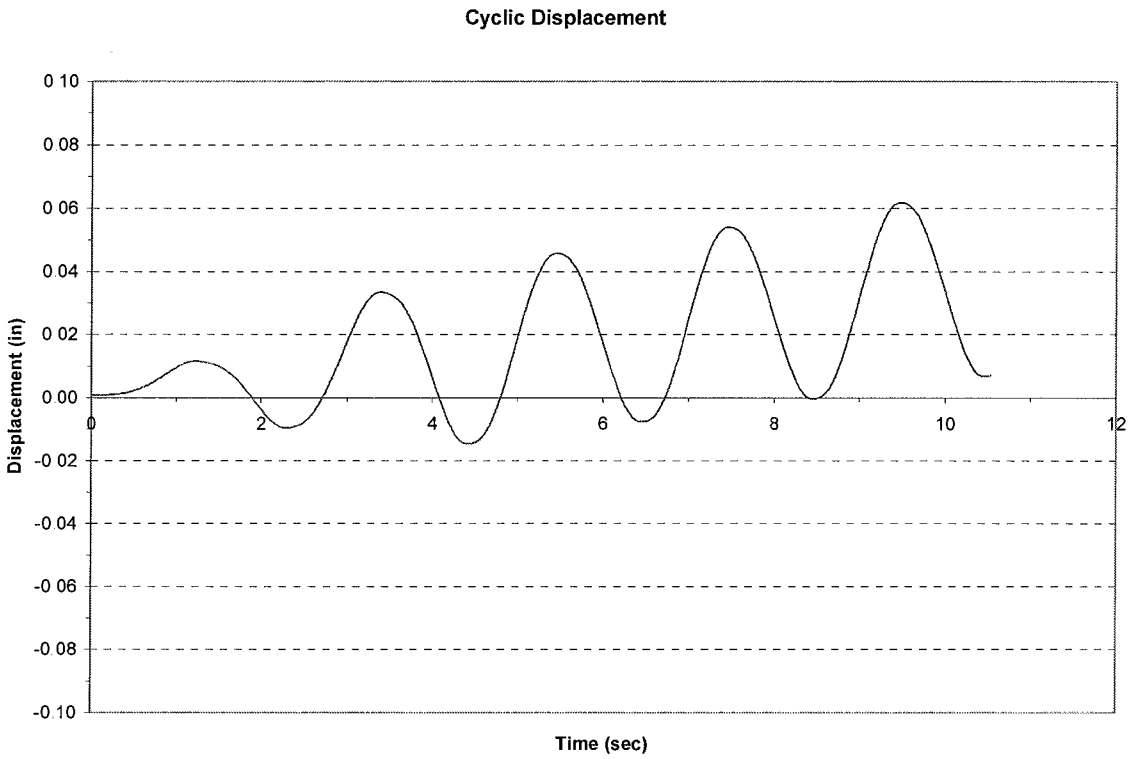

Figure A.12. 90C-20-20 cyclic displacement

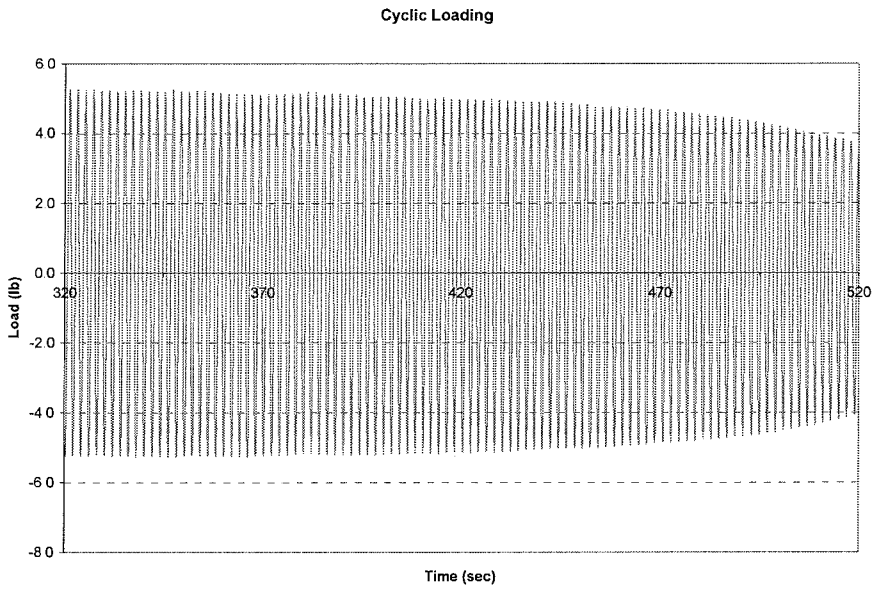

Figure A.13. 95C-20-10 cyclic loading. Cycles160 to 260 are presented

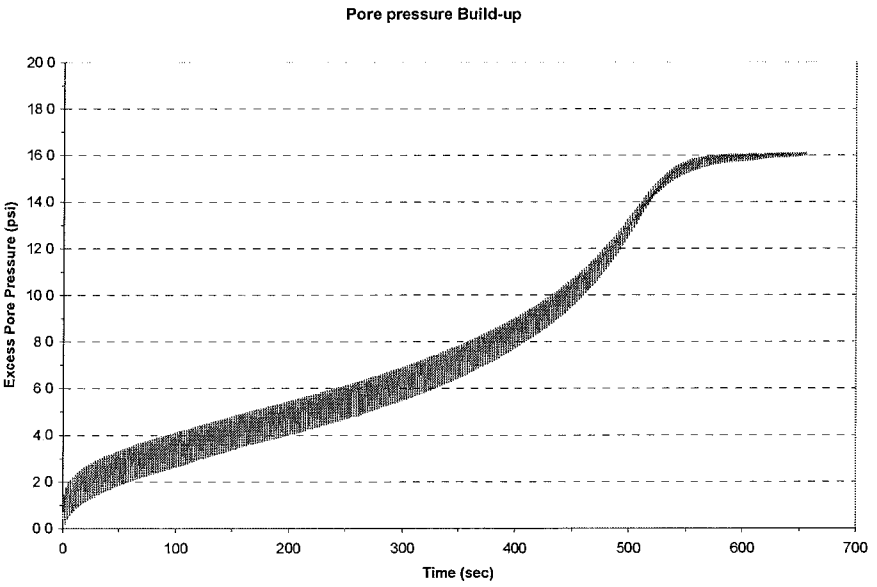

Figure A.14. 95C-20-10 pore water pressure build up

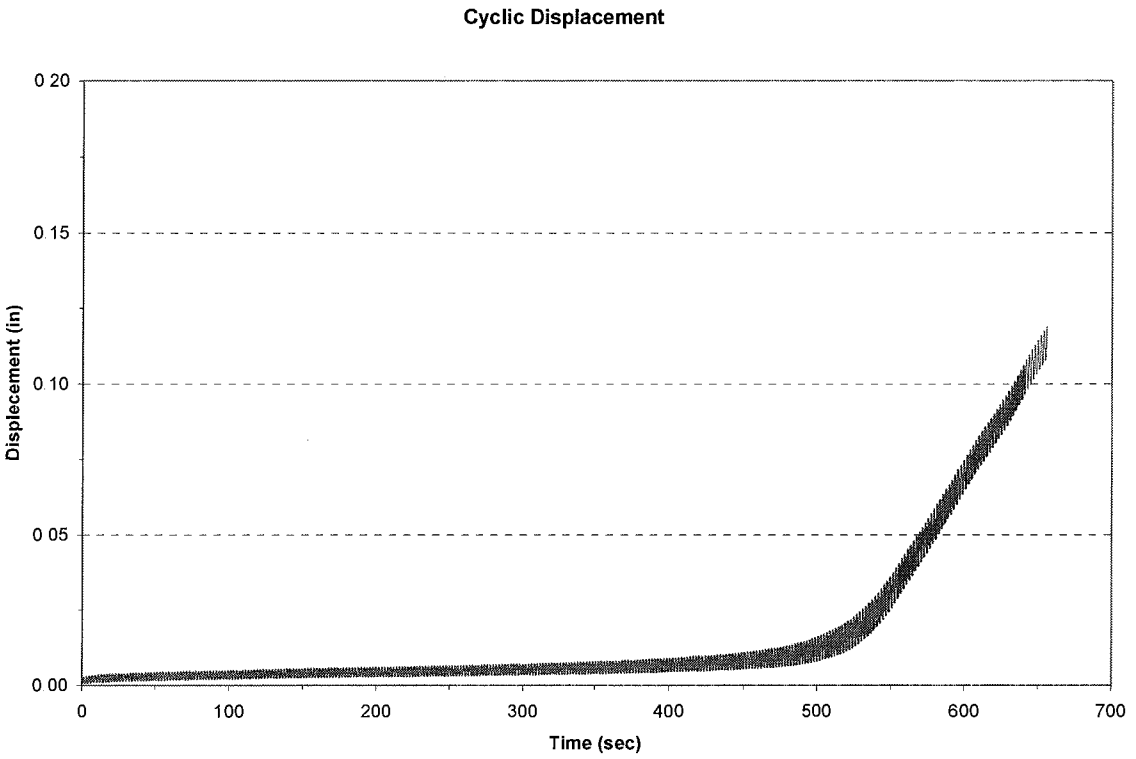

Figure A.15. 95C-20-10 cyclic displacement

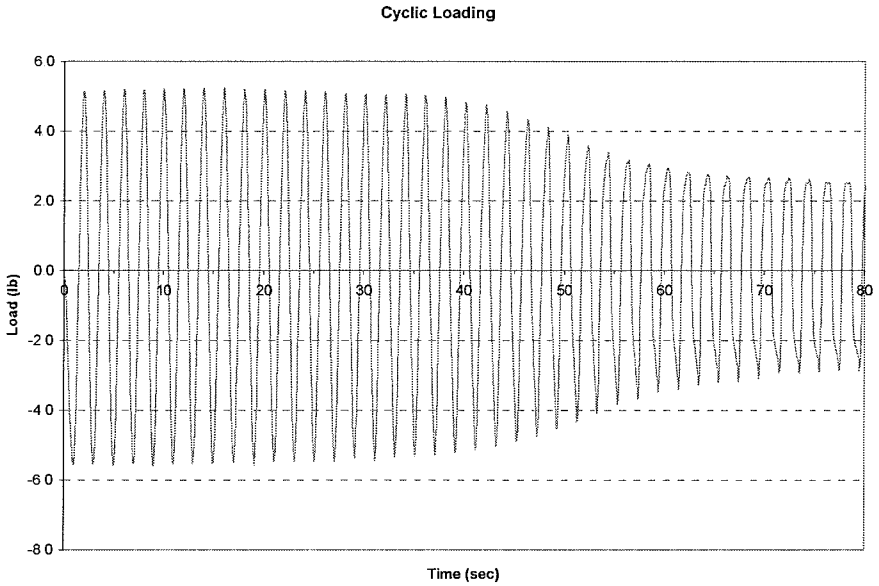

Figure A.16. 95C-10-20a cyclic loading

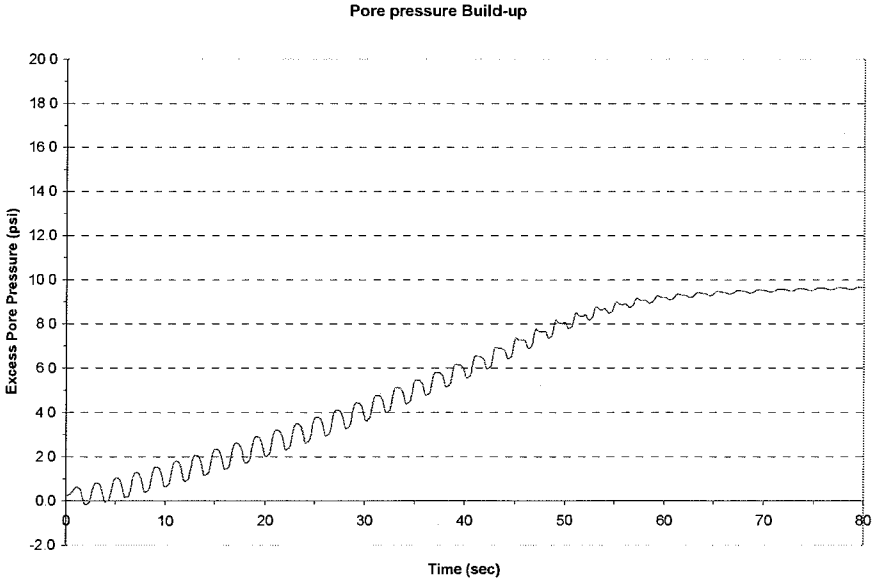

Figure A.17. 95C-10-20a pore water pressure build up

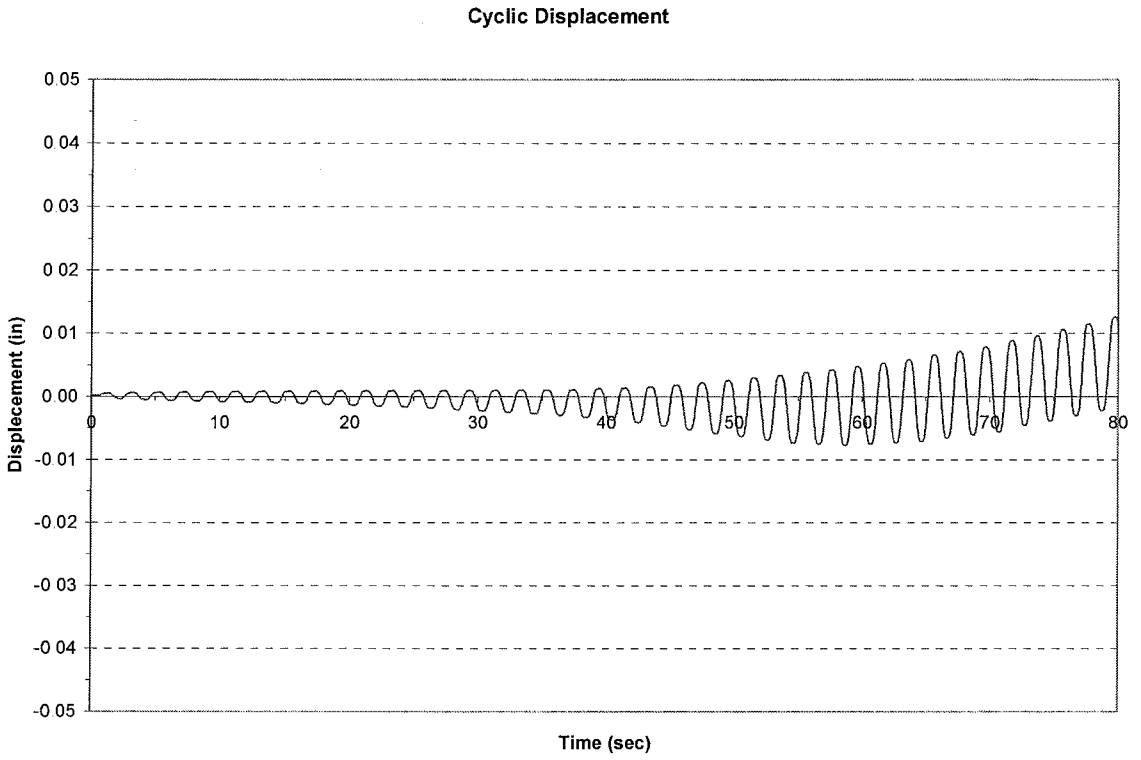

Figure A.18. 95C-10-20a cyclic displacement

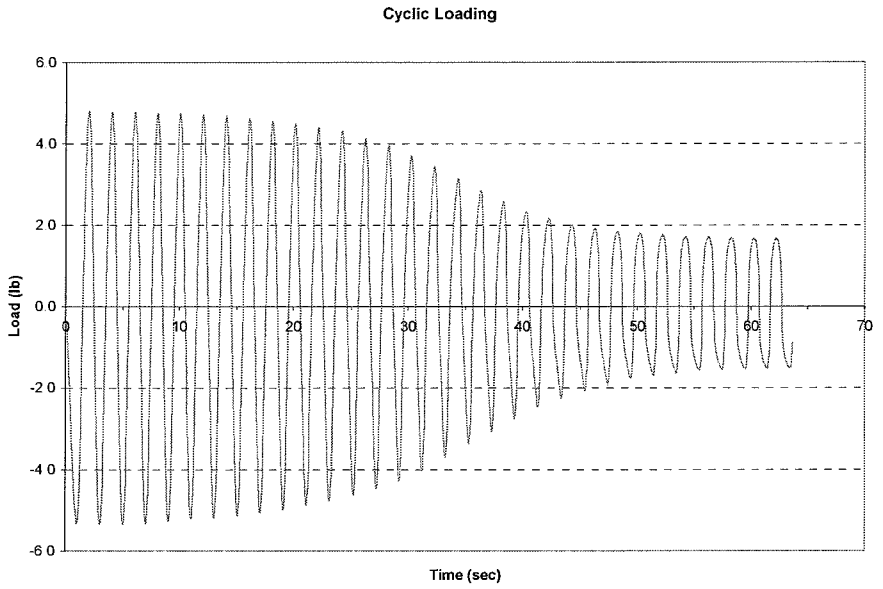

Figure A.19. 95C-10-20b, Cyclic loading

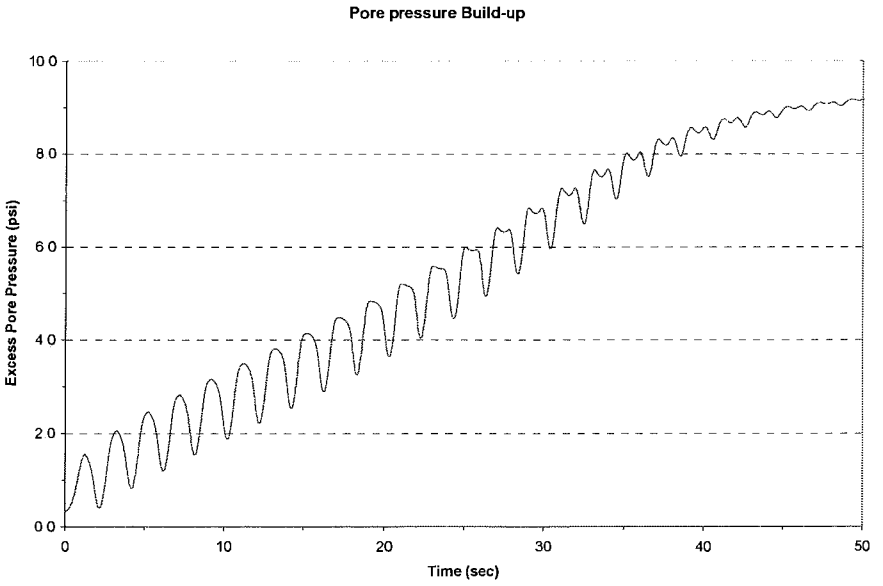

Figure A.20. 95C-10-20b pore water pressure build up

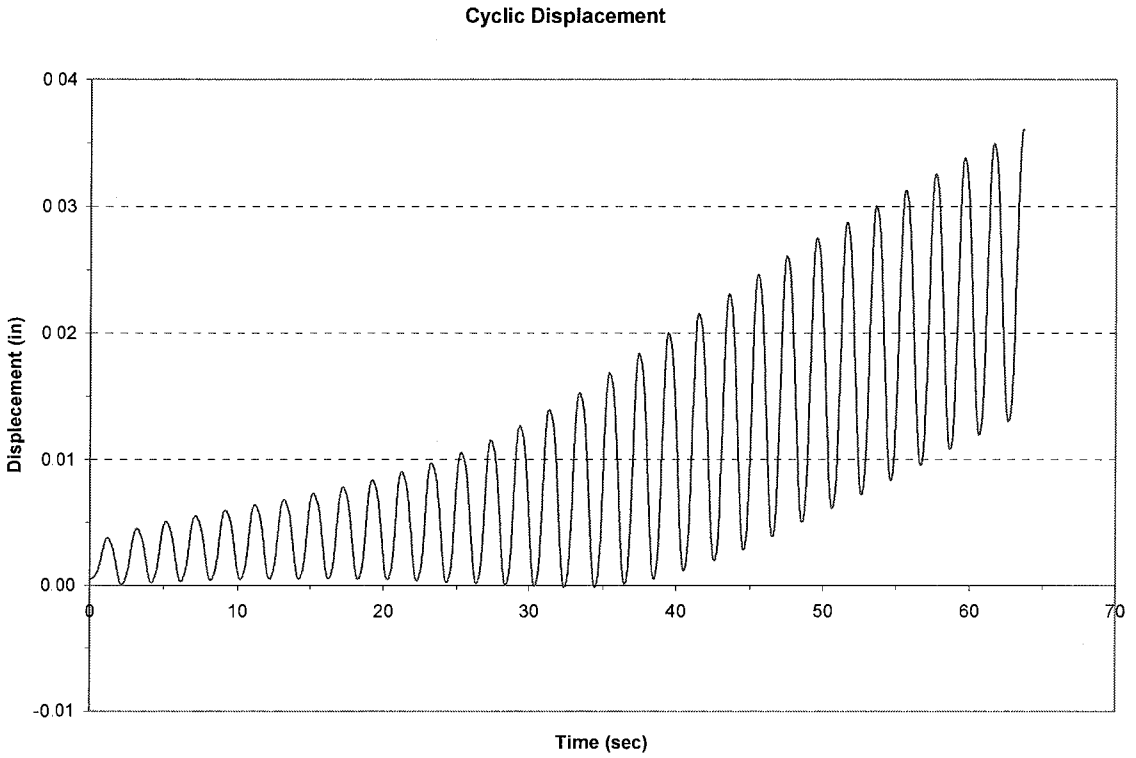

Figure A.21. 95C-10-20b, Cyclic displacement

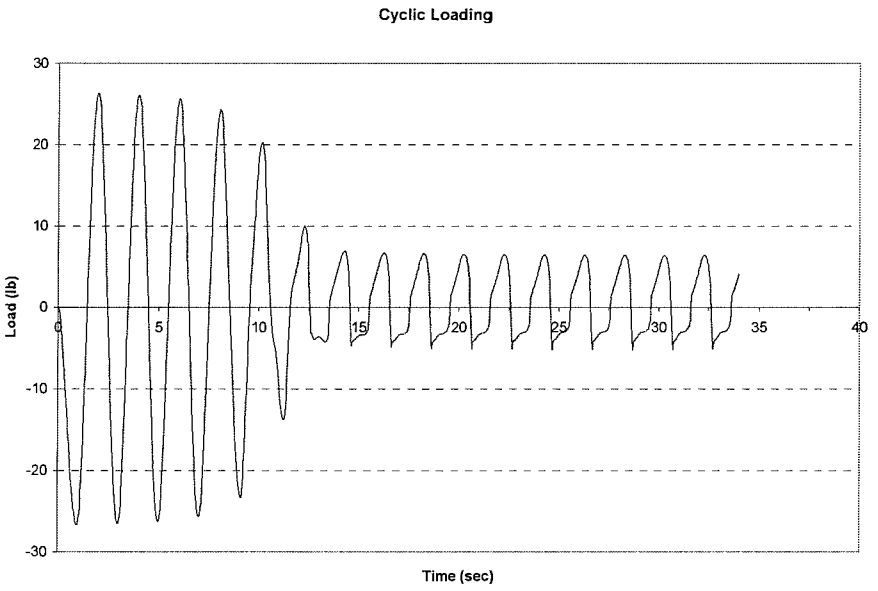

Figure A.22. 95C-50-20 cyclic loading

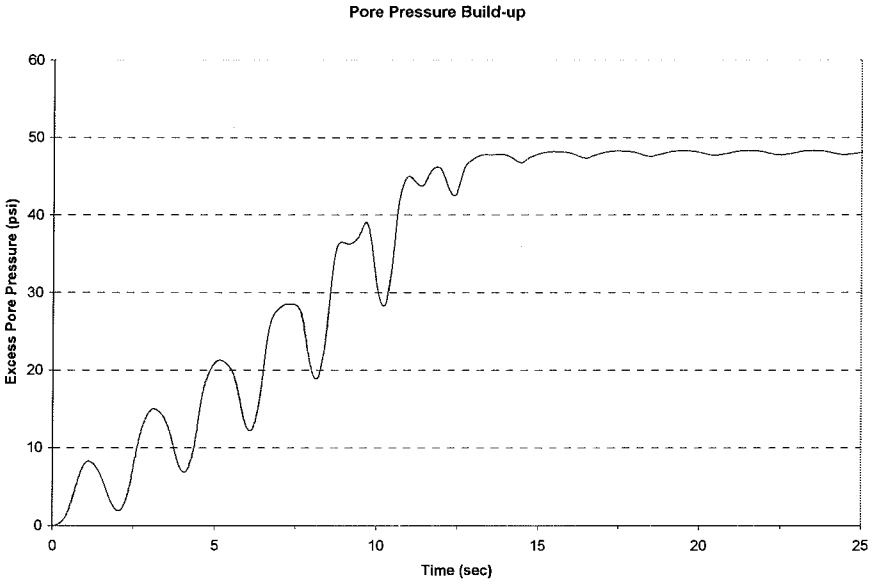

Figure A.23. 95C-50-20 pore water pressure build up

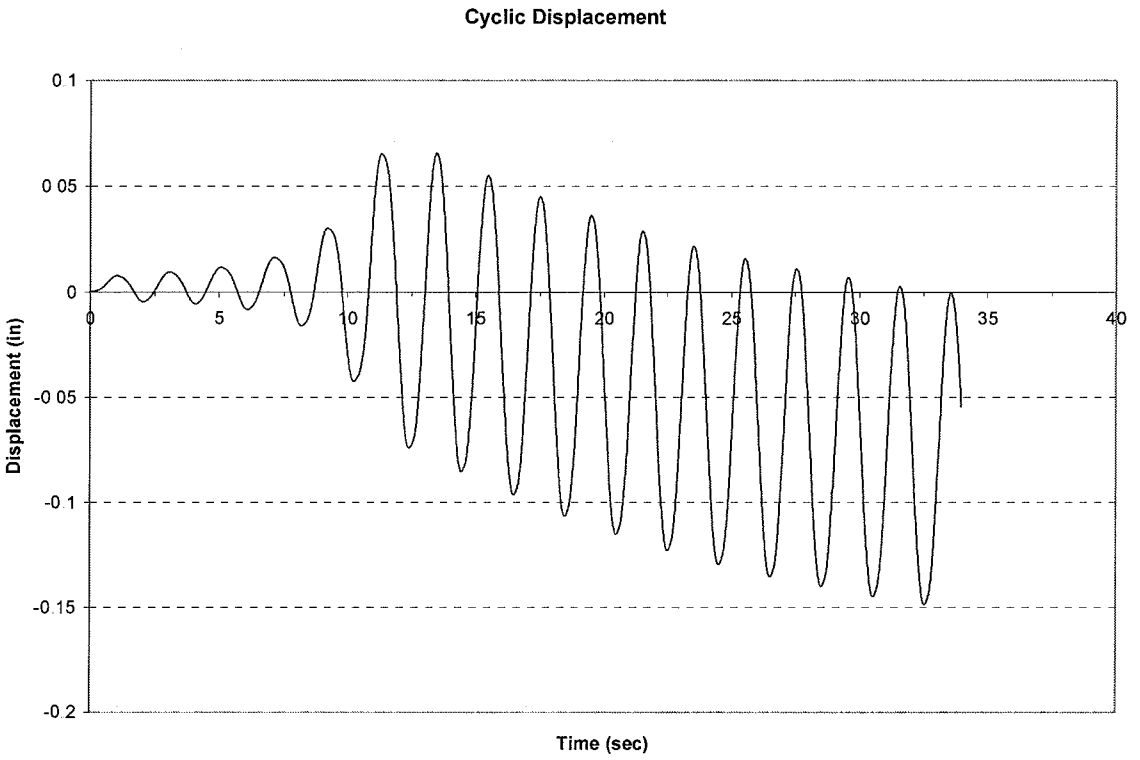

Figure A.24. 95C-50-20 cyclic displacement

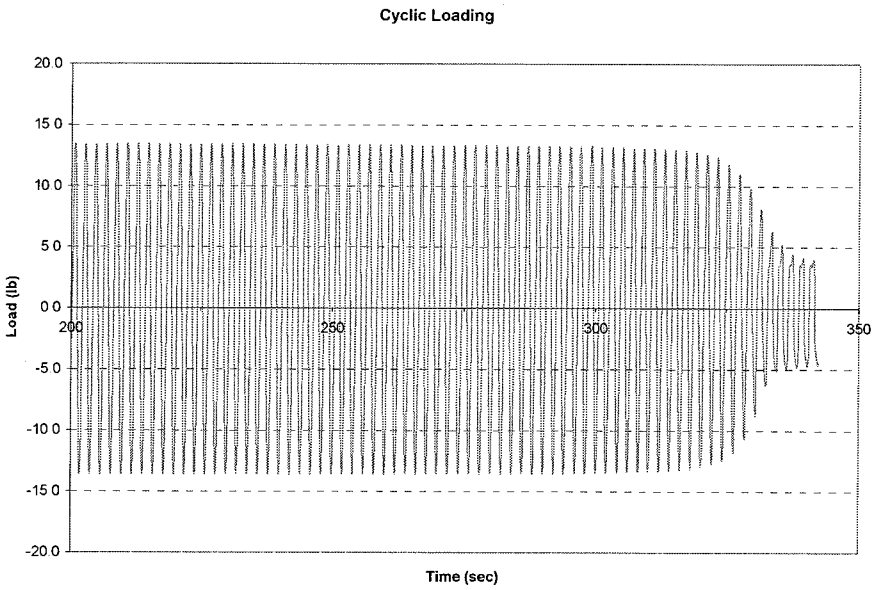

Figure A.25. 95C-50-10 cyclic loading

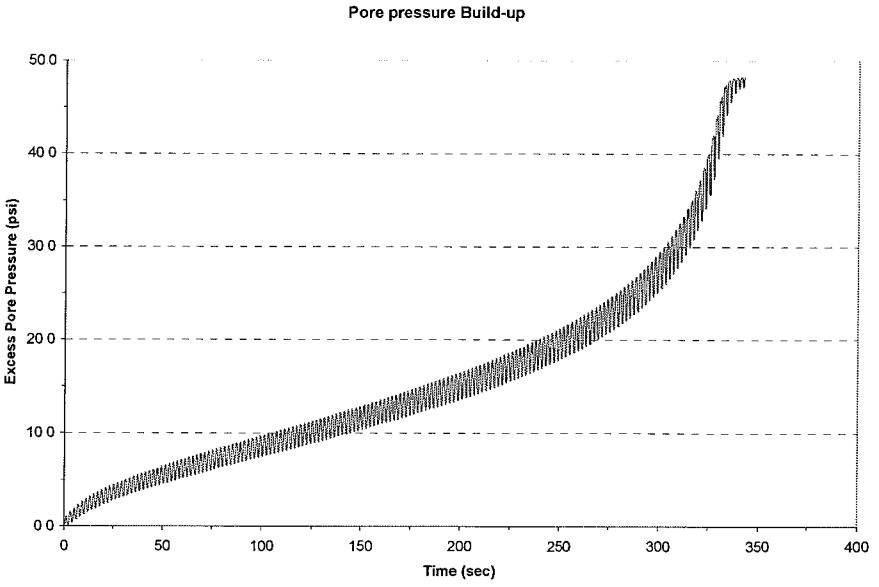

Figure A.26. 95C-50-10 pore water pressure build up

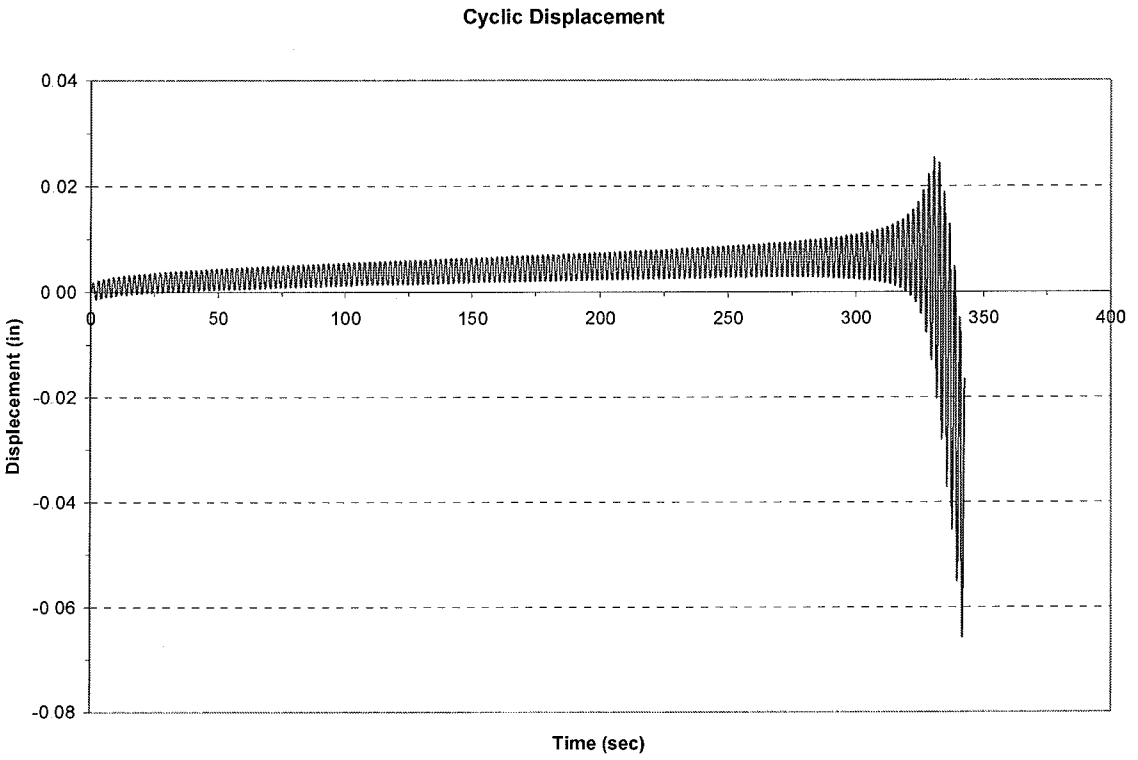

Figure A.27. 95C-50-10 cyclic displacement

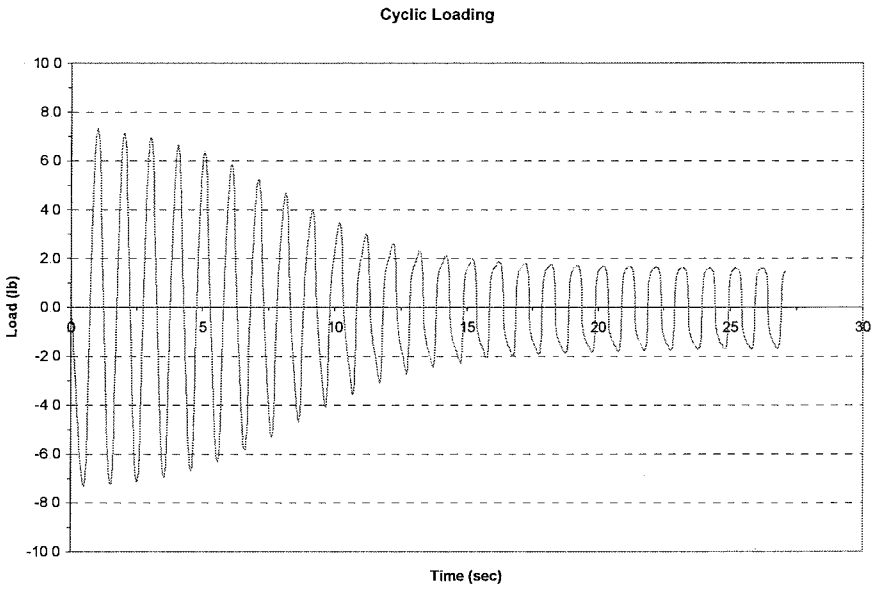

Figure A.28. 95C-20-15 cyclic loading

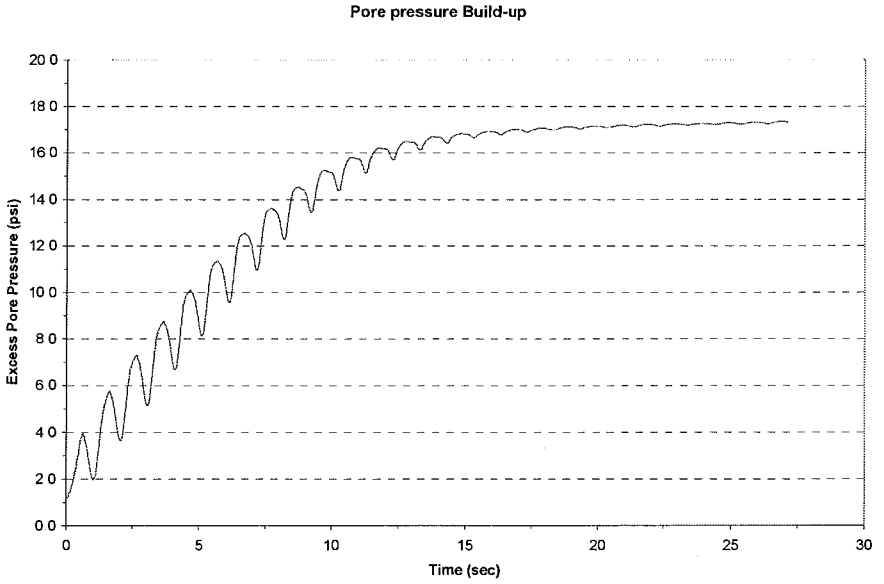

Figure A.29. 95C-20-15 pore water pressure build up

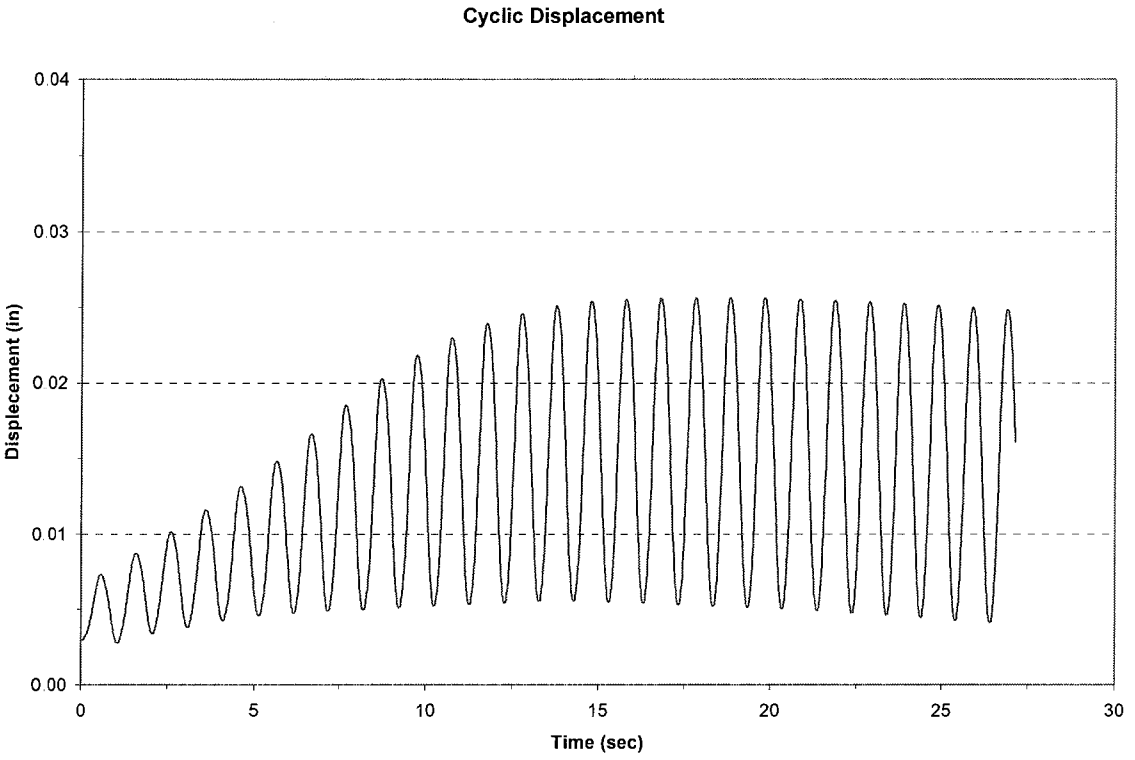

Figure A.30. 95C-20-15 cyclic displacement

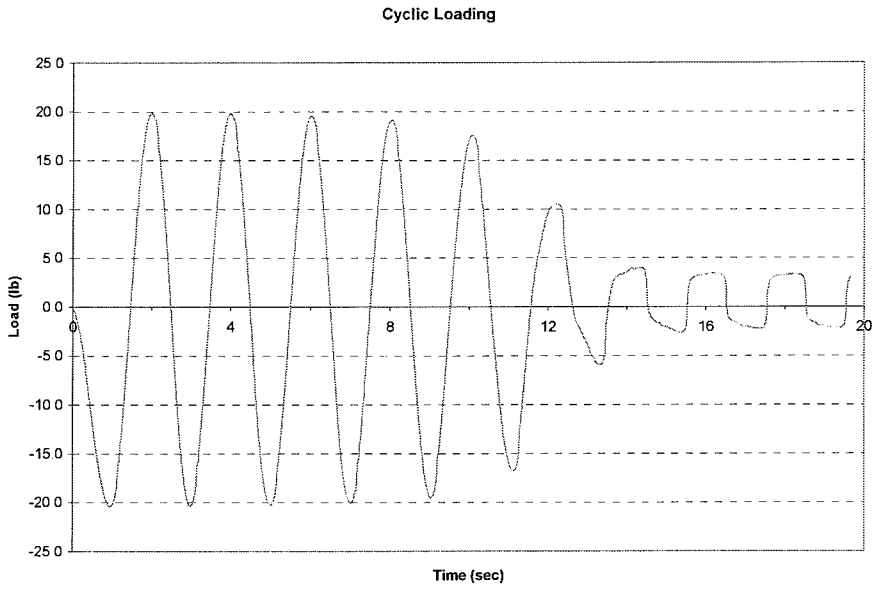

Figure A.31. 95C-50-15 cyclic loading

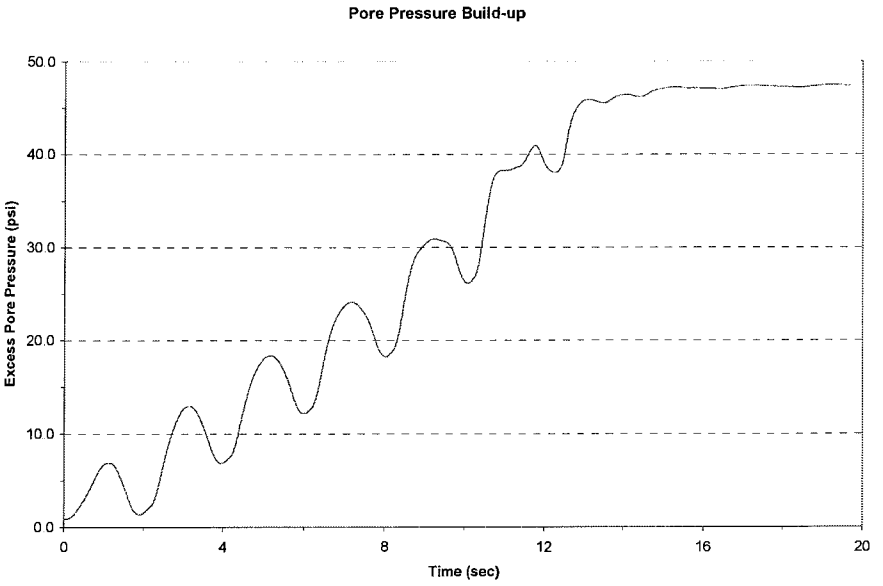

Figure A.32. 95C-50-15 pore water pressure build up

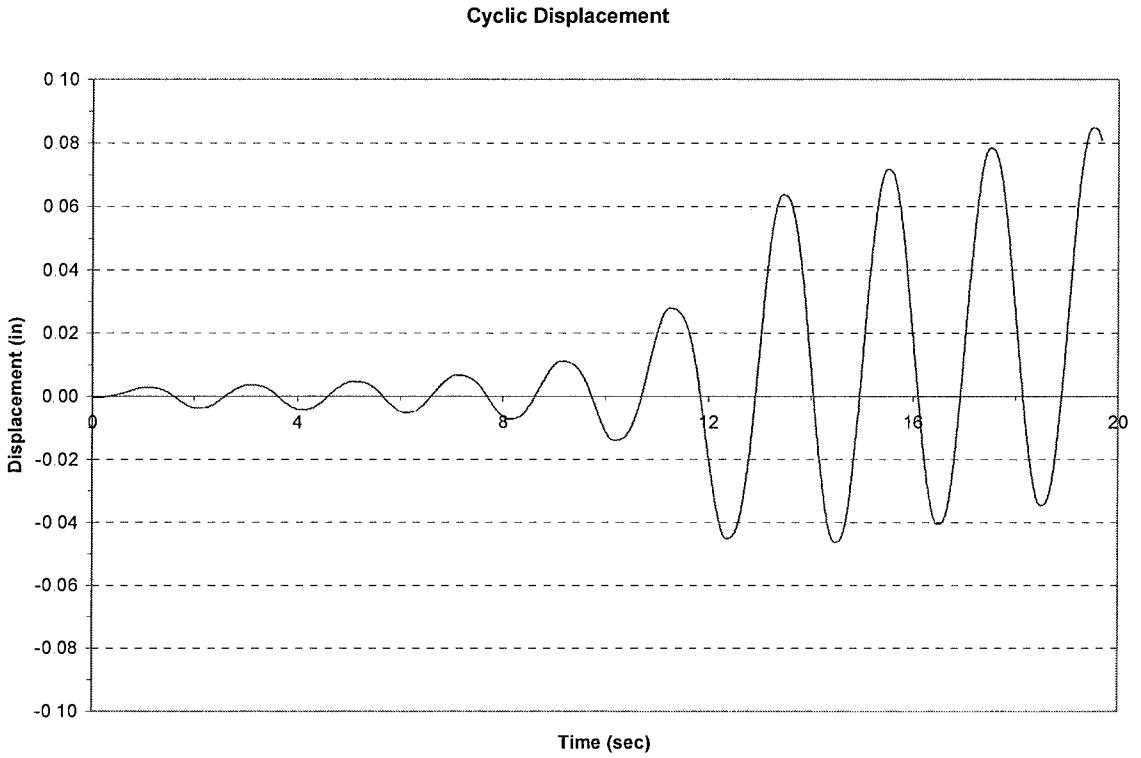

Figure A.33. 95C-50-15 cyclic displacement

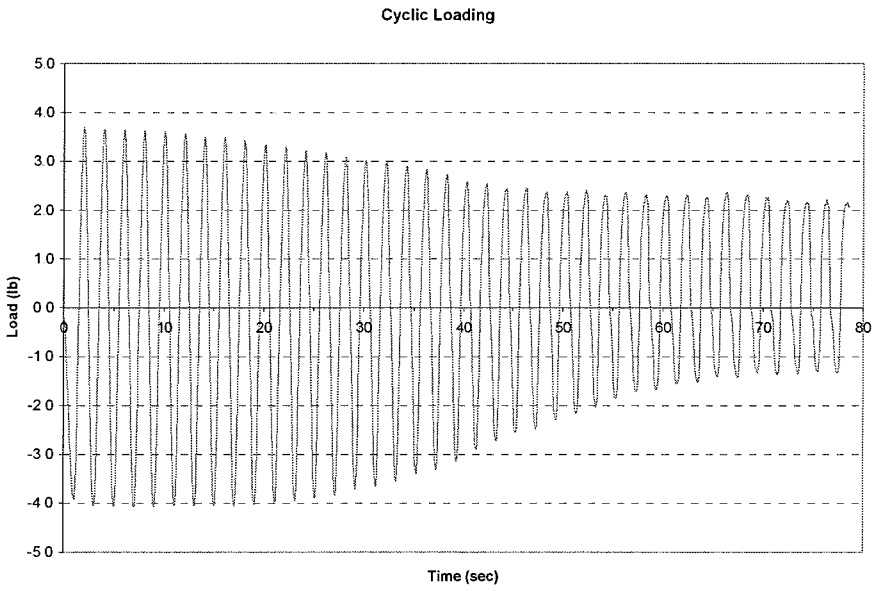

Figure A.34. 95C-10-15 cyclic loading

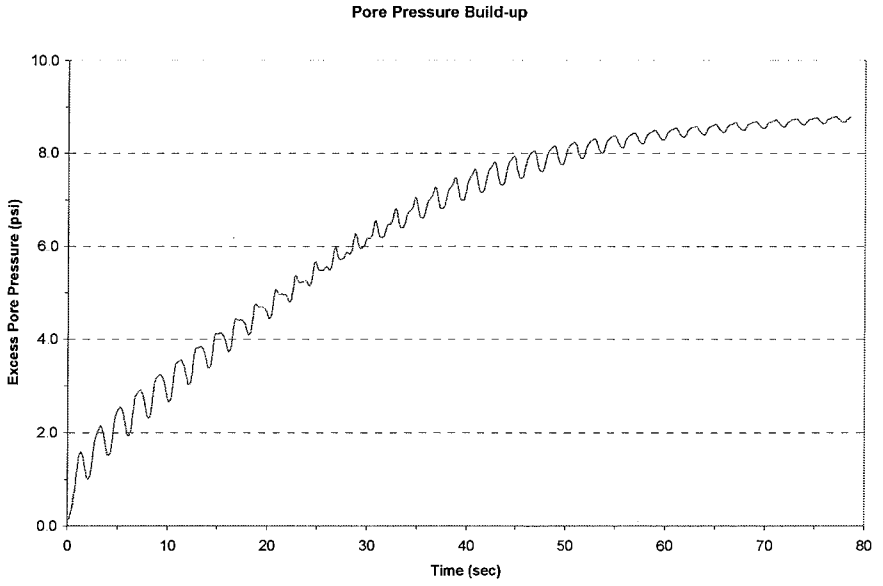

Figure A.35. 95C-10-15 pore water pressure build up

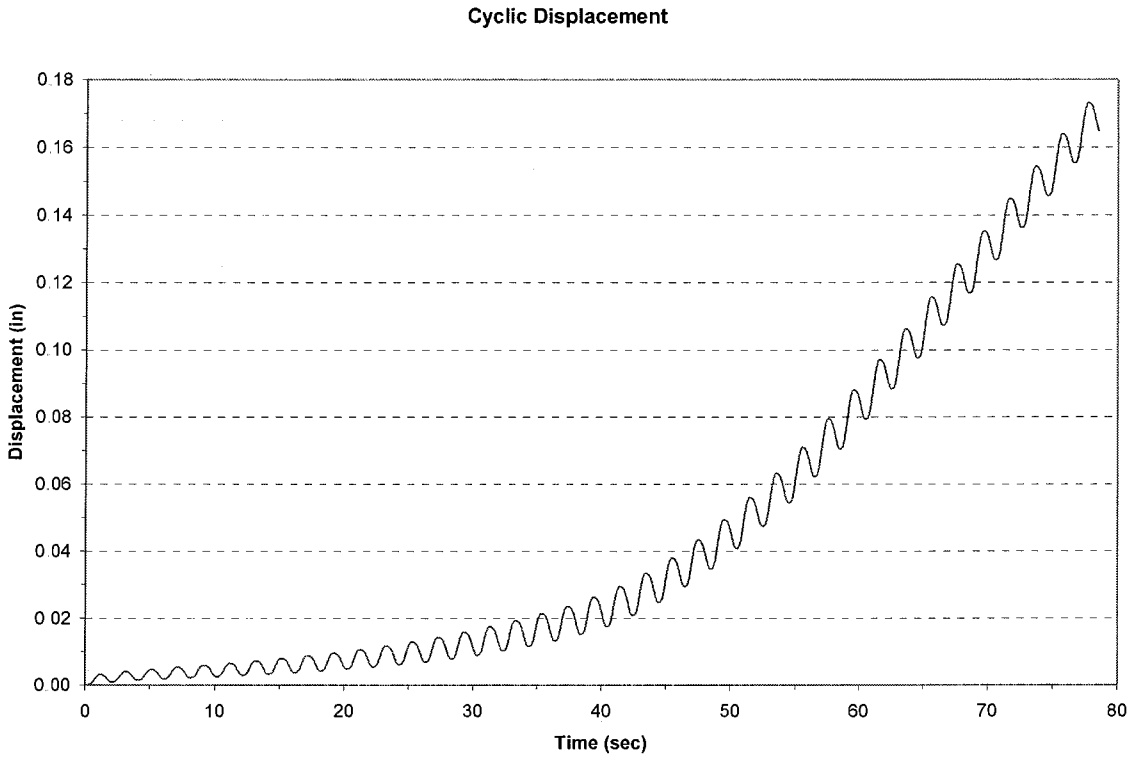

Figure A.36. 95C-10-15 cyclic displacement

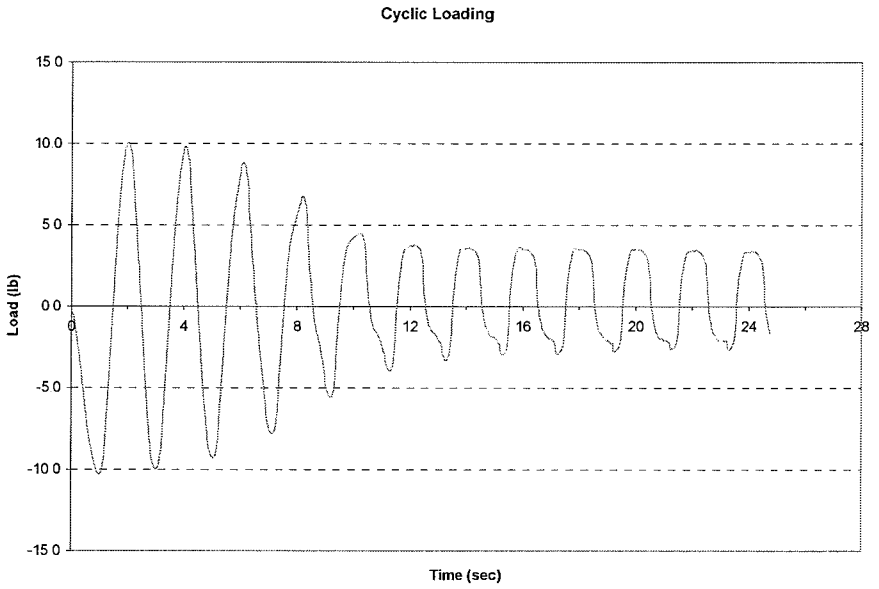

Figure A.37. 95C-20-20 cyclic loading

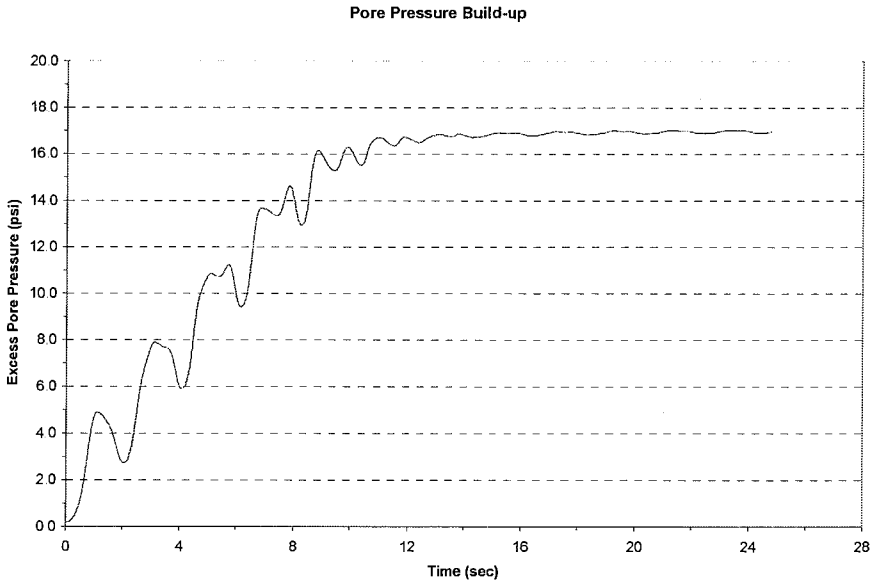

Figure A.38. 95C-20-20 pore water pressure build up

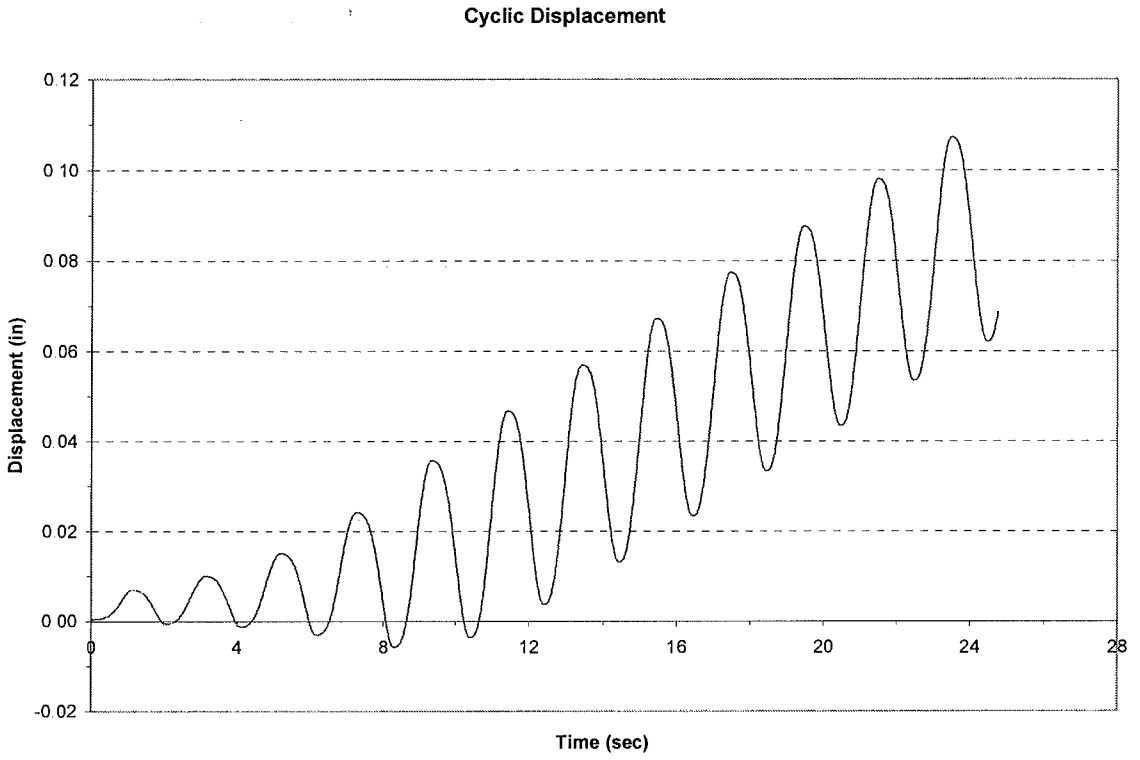

Figure A.39. 95C-20-20 cyclic displacement

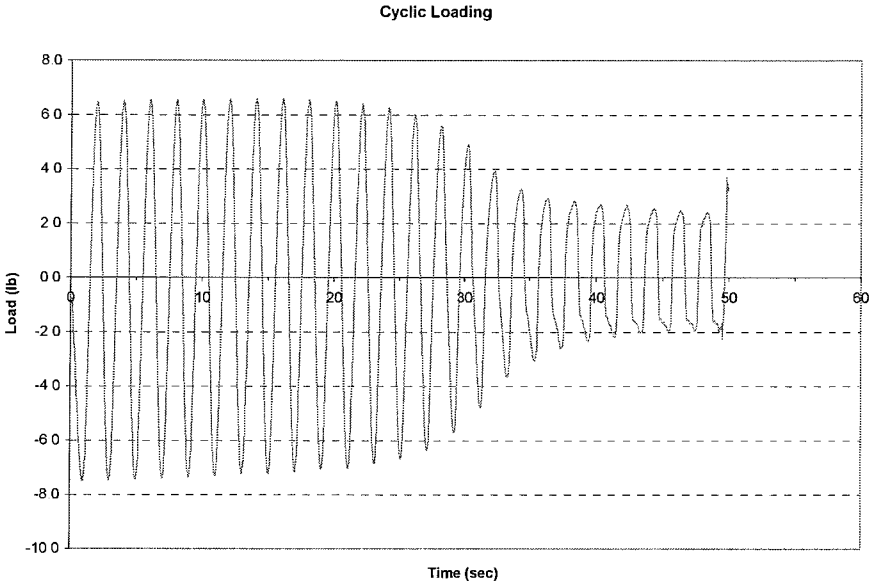

Figure A.40. 95C-20-13 cyclic loading

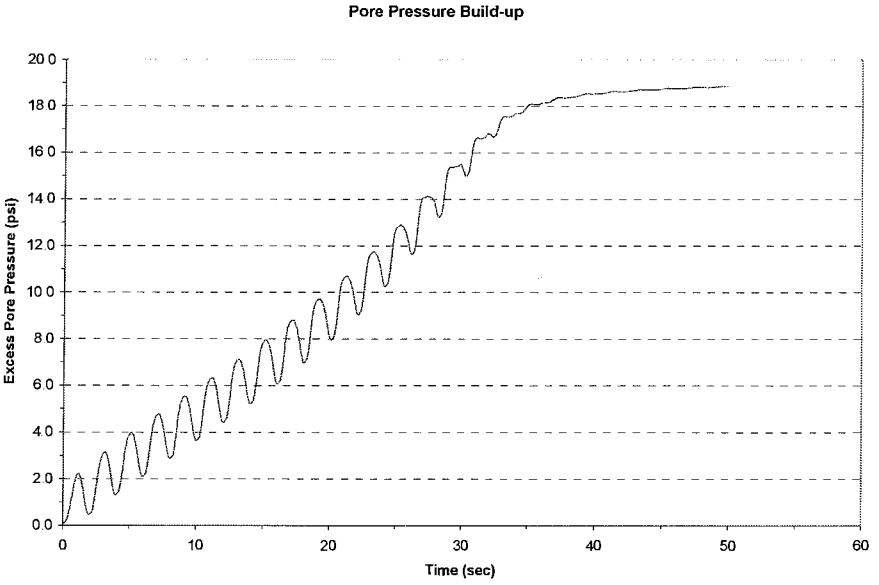

Figure A.41. 95C-20-13 pore water pressure build up

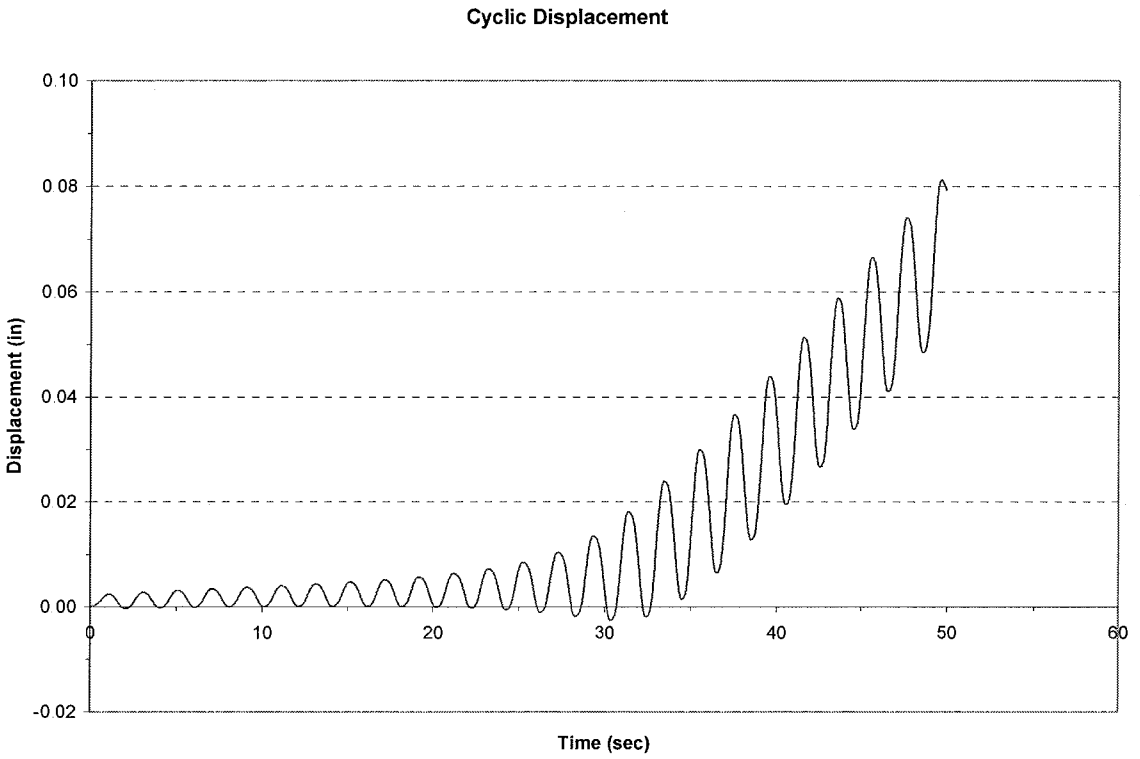

Figure A.42. 95C-20-13 cyclic displacement

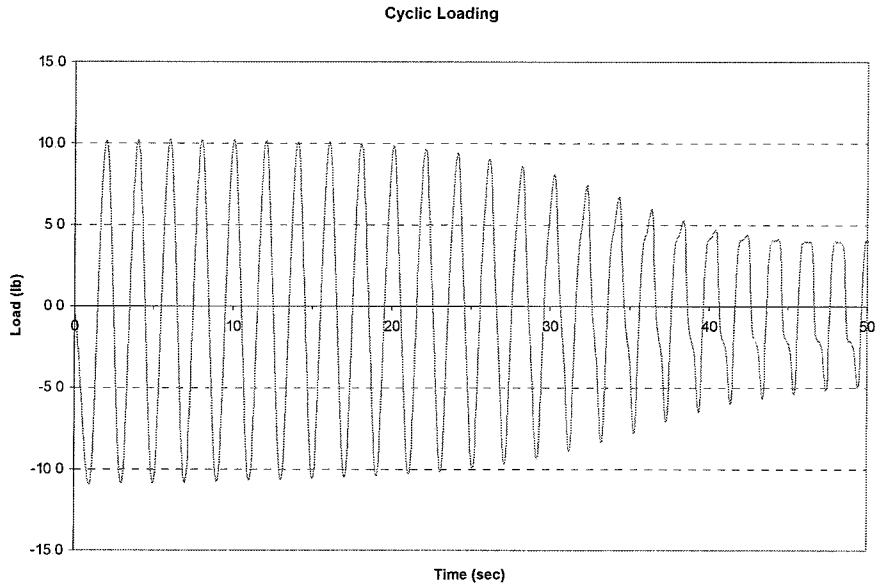

Figure A.43. 105C-20-20 cyclic loading

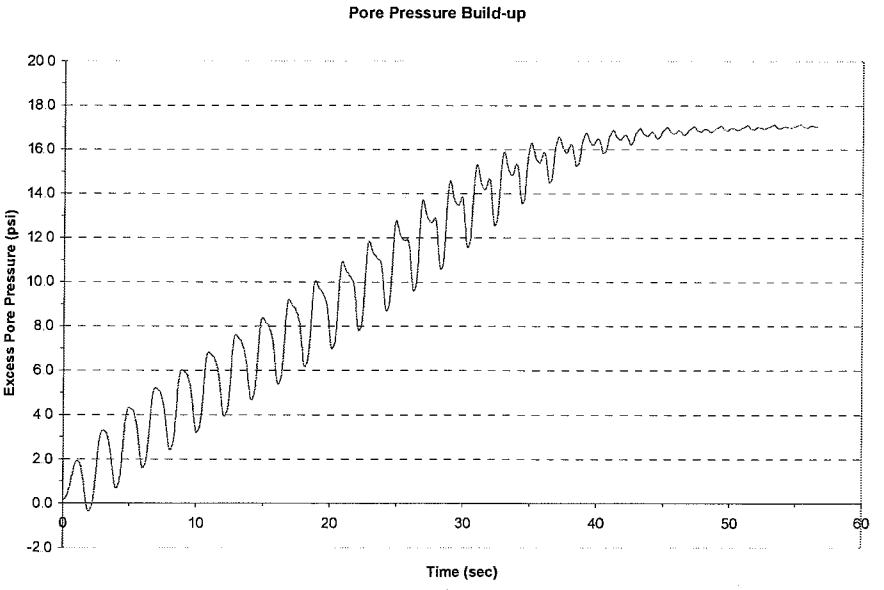

Figure A.44. 105C-20-20 pore water pressure build up

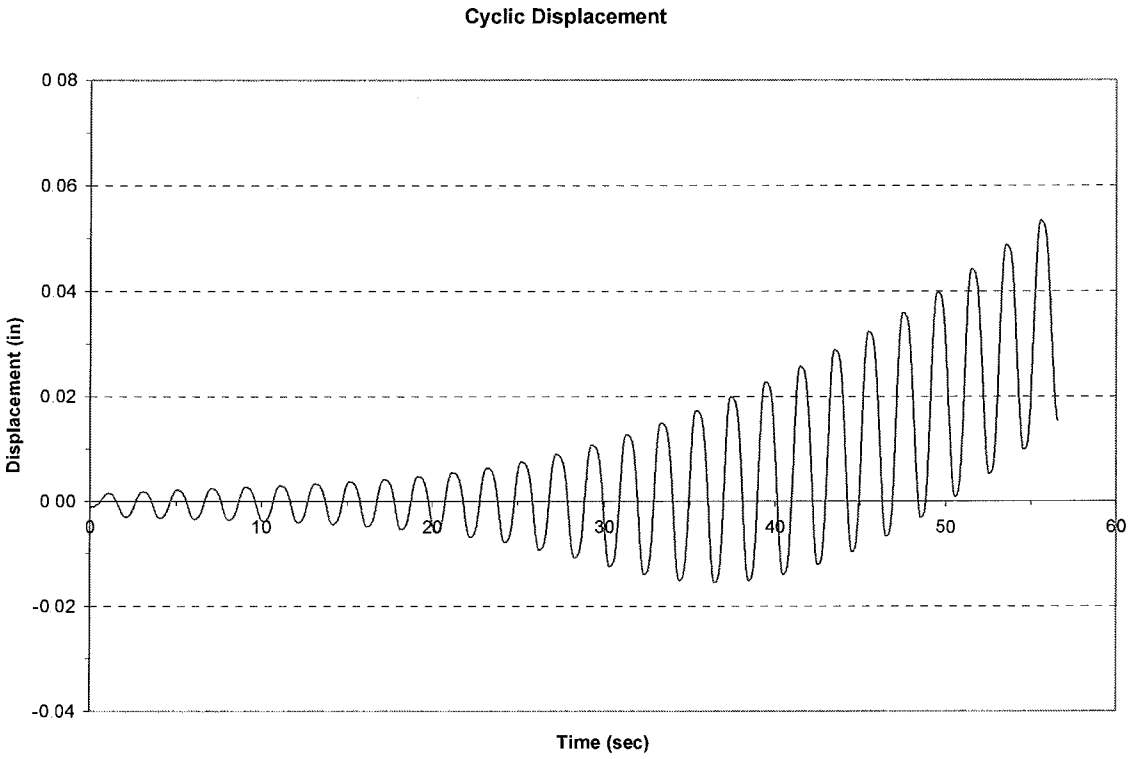

Figure A.45. 105C-20-20 cyclic displacement

Appendix B

Ground Response Analysis Results

1. Analysis A-1: Section A-A' with Input Motion TAFT (a_{max}=0.08g)

Soil Profile

Profile Name: AEP impounded fly ash facility Section A-A'

Water Table: 86.00 ft

Number of Layers: 10

Input Motion

Number of Motions: 1

Number of Iterations: 5

Strain Ratio: 0.65

Tolerance: 5.00%

File Name	No of Acc. Values	Max. Acc. (g)	Time Step (sec)	Cuttoff Freq. (Hz)	No of Fourier Terms	Layer	Outcrop
D:\EDUSHAKE\TAFT.EQ	4220	**0.080**	0.020	20.00	8192	10	No

Output Locations

Layer No	Depth (ft)	Outcrop
1	0.00	No
3	18.00	No
4	28.00	No
5	38.00	No

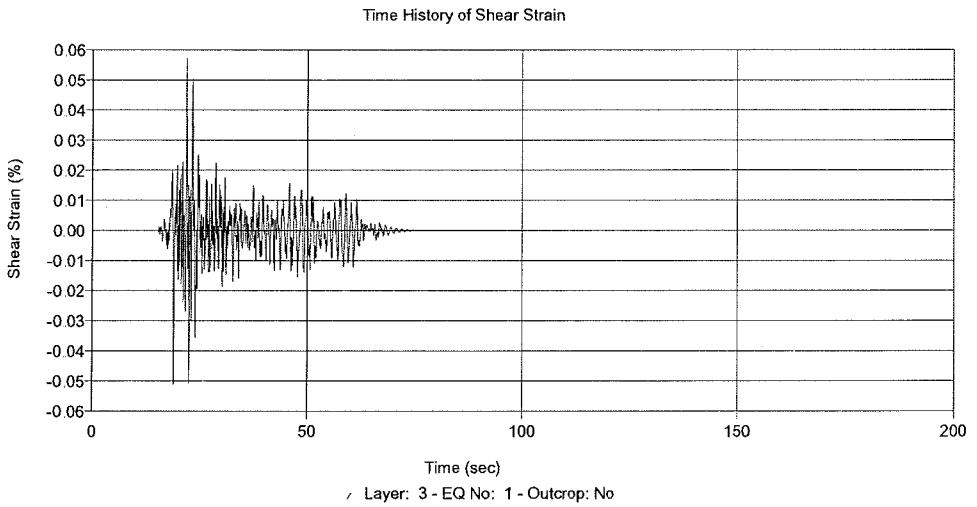
Time History of Shear Strain
Shear Strain (%)
0.06
0.05
0.04
0.03
0.02
0.01
0.00
-0.01
-0.02
-0.03
-0.04
-0.05
-0.06
0
50
100
150
200
Time (sec)
Layer: 3 - EQ No: 1 - Outcrop: No

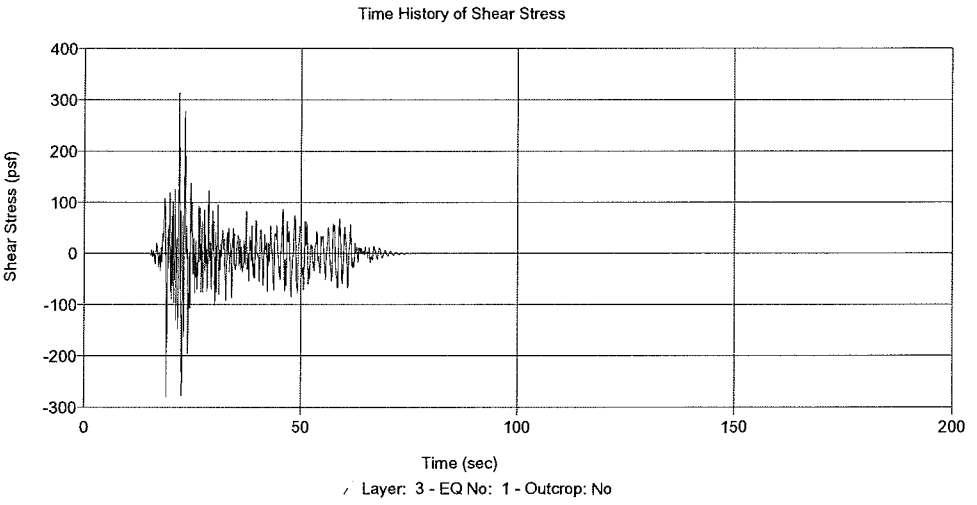
Time History of Shear Stress
Shear Stress (psf)
400
300
200
100
0
-100
-200
-300
0
50
100
150
200
Time (sec)
Layer: 3 - EQ No: 1 - Outcrop: No

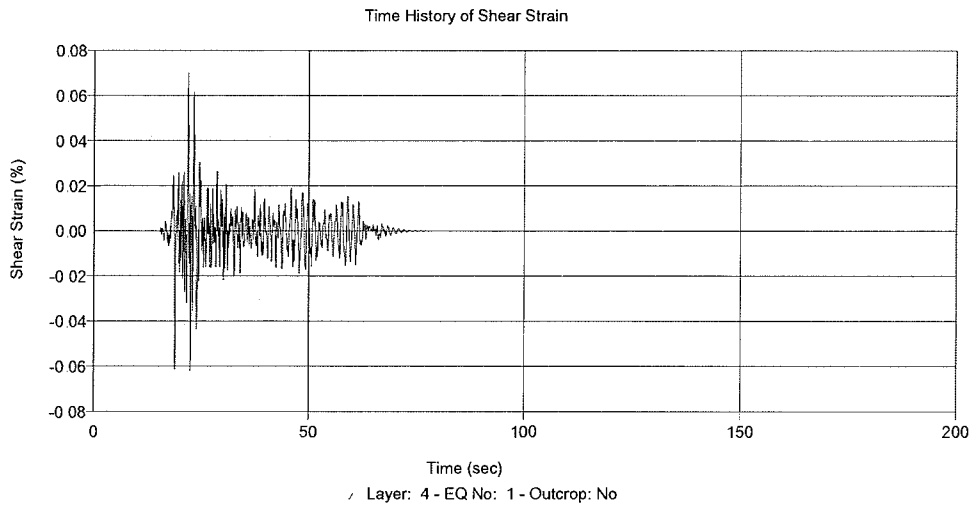
Time History of Shear Strain
0.08
0.06
0.04
0.02
0.00
-0.02
-0.04
-0.06
-0.08
Shear Strain (%)
0
50
100
150
200
Time (sec)
Layer: 4 - EQ No: 1 - Outcrop: No

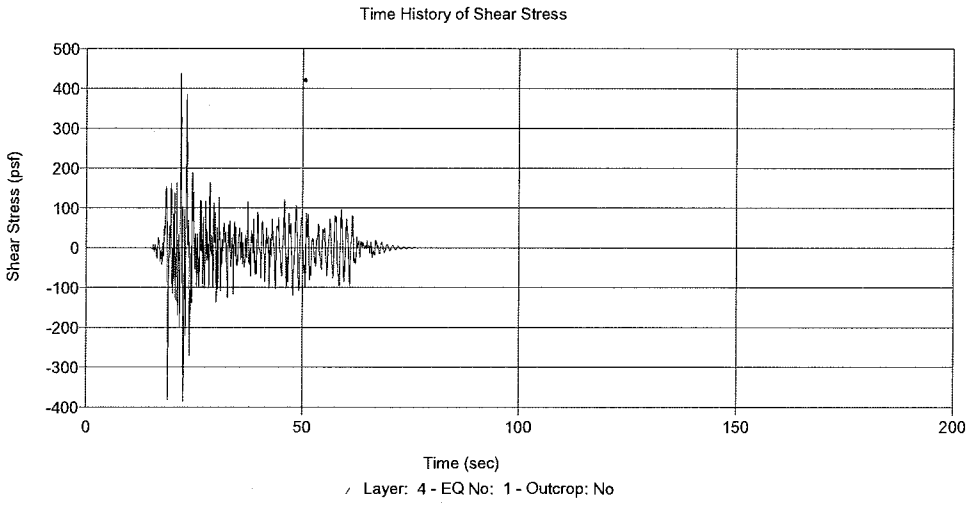
Time History of Shear Stress
500
400
300
200
100
0
-100
-200
-300
-400
Shear Stress (psf)
0
50
100
150
200
Time (sec)
Layer: 4 - EQ No: 1 - Outcrop: No

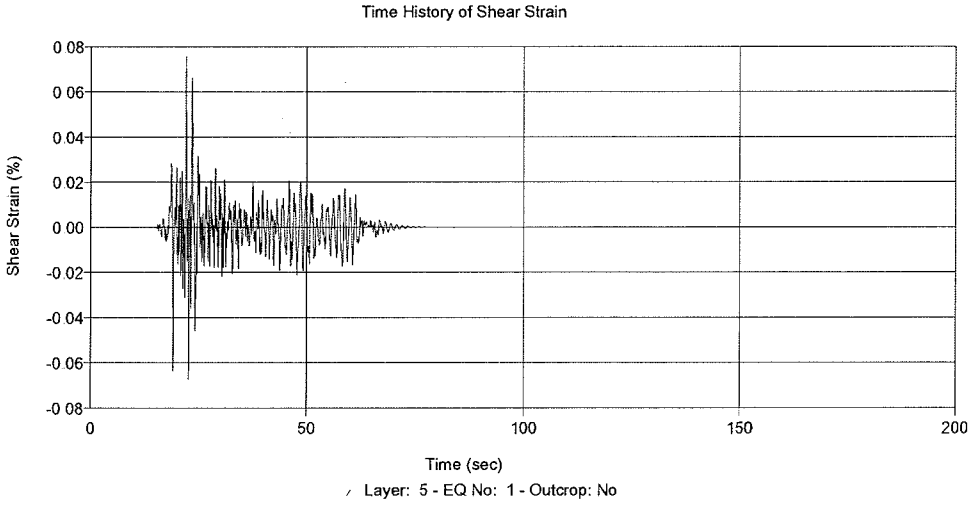
Time History of Shear Strain
0 08
0 06
0 04
0 02
0 00
-0 02
-0 04
-0 06
-0 08
Shear Strain (%)
0
50
100
150
200
Time (sec)
Layer: 5 - EQ No: 1 - Outcrop: No

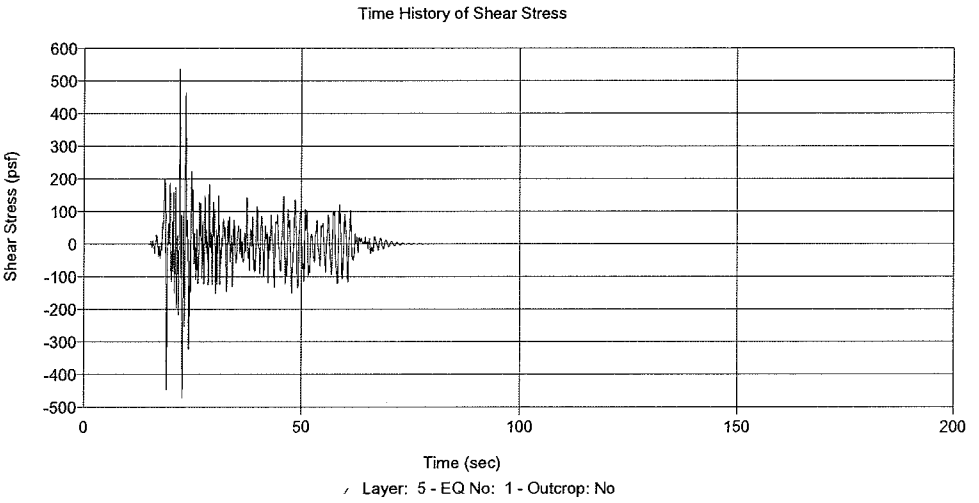
Time History of Shear Stress
600
500
400
300
200
100
0
-100
-200
-300
-400
-500
Shear Stress (psf)
0
50
100
150
200
Time (sec)
Layer: 5 - EQ No: 1 - Outcrop: No

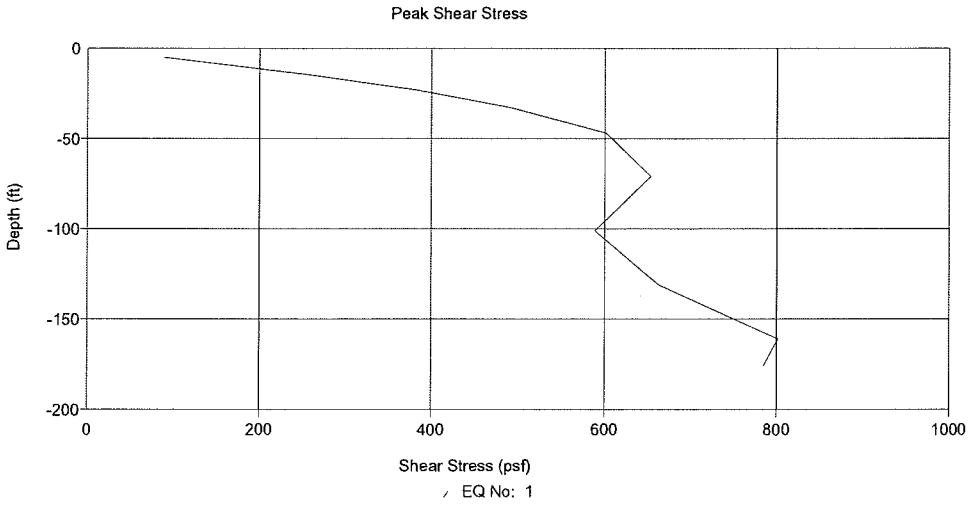
Peak Shear Stress
0
-50
-100
-150
-200
Depth (ft)
0
200
400
600
800
1000
Shear Stress (psf)
EQ No: 1

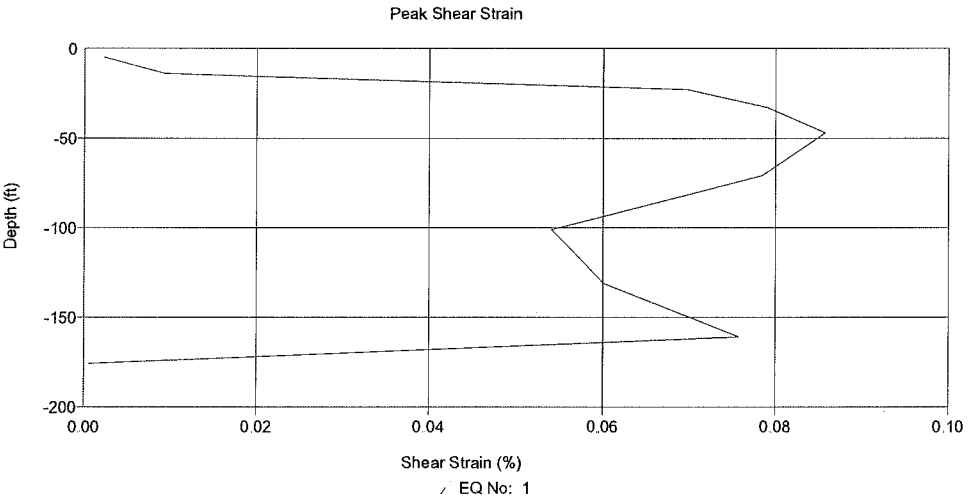
Peak Shear Strain
0
-50
-100
-150
-200
Depth (ft)
0.00
0.02
0.04
0.06
0.08
0.10
Shear Strain (%)
EQ No: 1

2. Analysis A-2: Section A-A' with Input Motion TAFT (a_{max}=0.15g)

Input Motion

Number of Motions: 1

Number of Iterations: 5

Strain Ratio: 0.65

Tolerance: 5.00%

File Name	No of Acc. Values	Max. Acc. (g)	Time Step (sec)	Cuttoff Freq. (Hz)	No of Fourier Terms	Layer	Outcrop
D:\EDUSHAKE\TAFT.E Q	4220	**0.150**	0.020	20.00	8192	10	No

Output Locations

Layer No	Depth (ft)	Outcrop
1	0.00	No
3	18.00	No
4	28.00	No
5	38.00	No

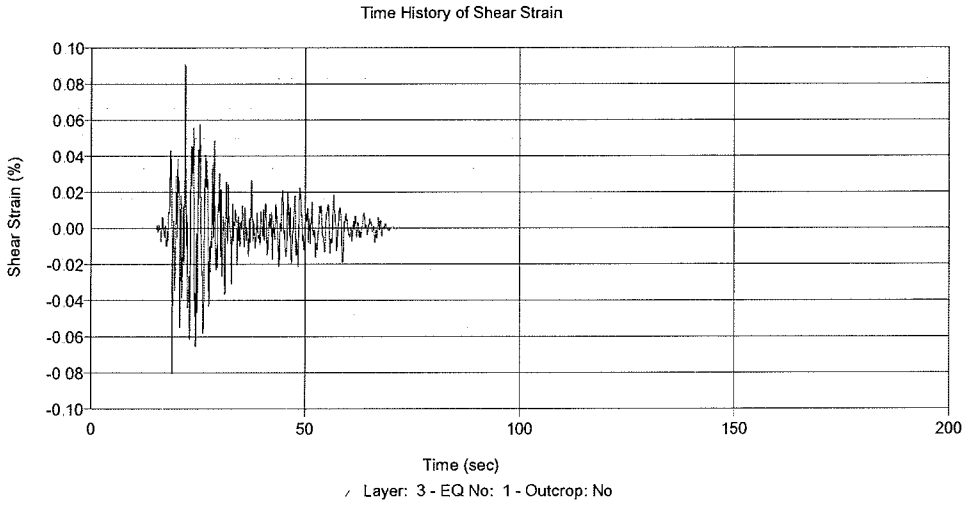
Time History of Shear Strain
0.10
0.08
0.06
0.04
0.02
0.00
-0.02
-0.04
-0.06
-0.08
-0.10
Shear Strain (%)
0
50
100
150
200
Time (sec)
Layer: 3 - EQ No: 1 - Outcrop: No

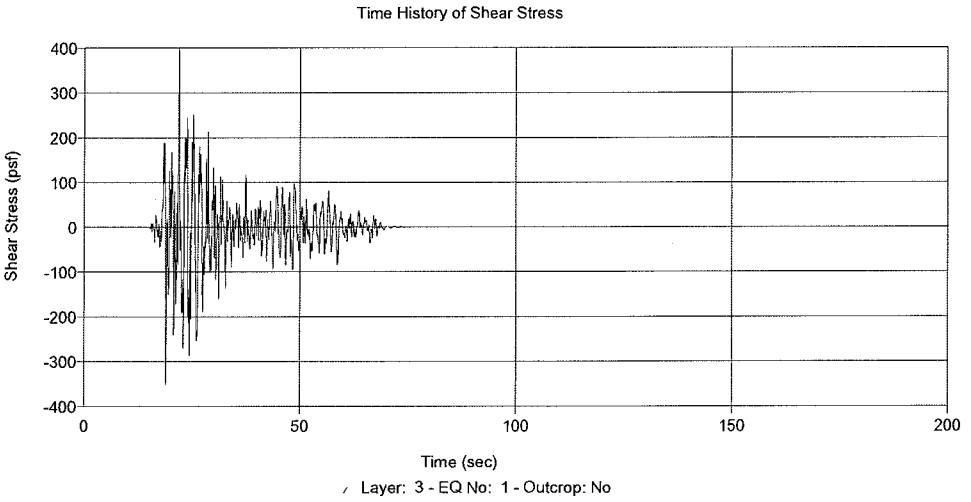
Time History of Shear Stress
400
300
200
100
0
-100
-200
-300
-400
Shear Stress (psf)
0
50
100
150
200
Time (sec)
Layer: 3 - EQ No: 1 - Outcrop: No

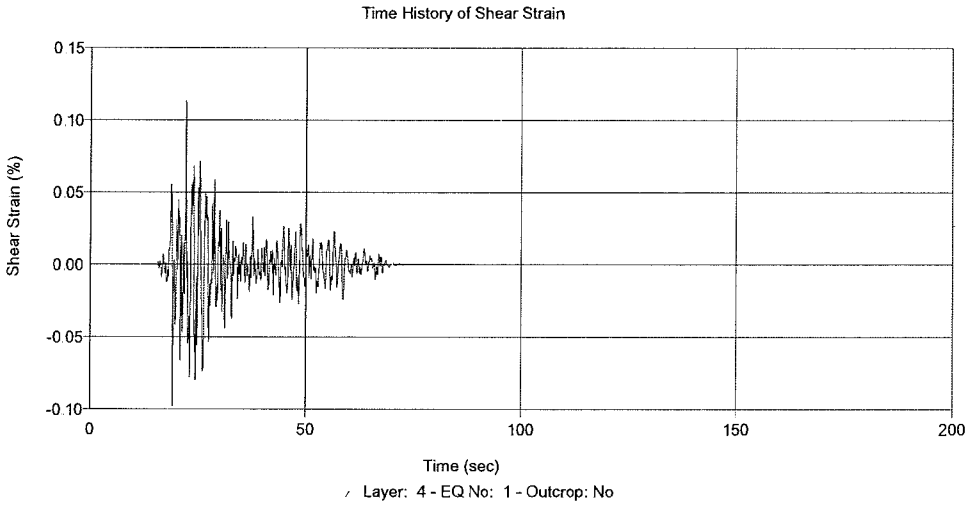
Time History of Shear Strain
0.15
0.10
0.05
0.00
-0.05
-0.10
Shear Strain (%)
0
50
100
150
200
Time (sec)
Layer: 4 - EQ No: 1 - Outcrop: No

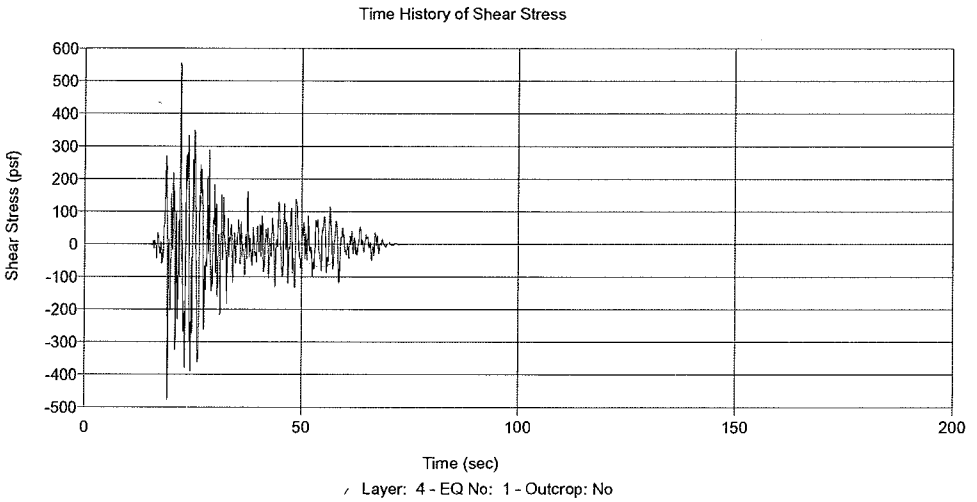
Time History of Shear Stress
600
500
400
300
200
100
0
-100
-200
-300
-400
-500
Shear Stress (psf)
0
50
100
150
200
Time (sec)
Layer: 4 - EQ No: 1 - Outcrop: No

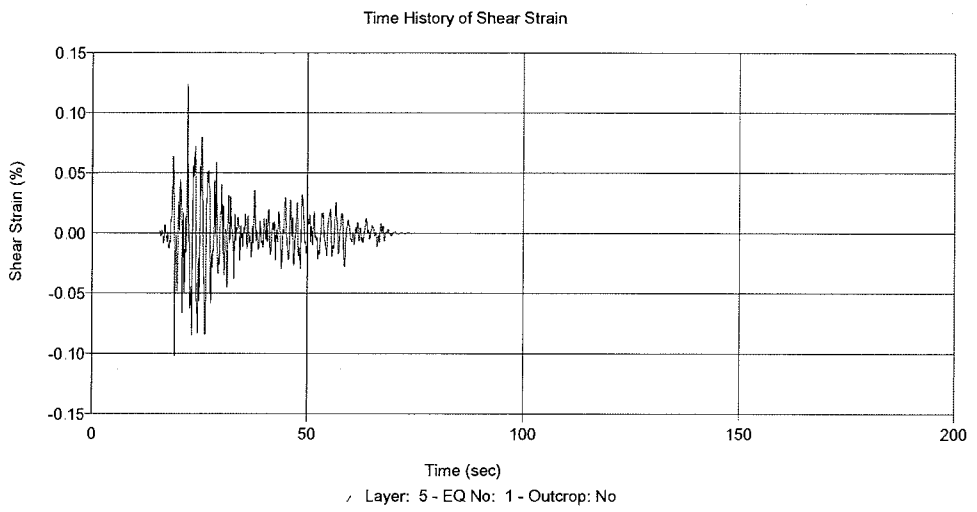
Time History of Shear Strain
0.15
0.10
0.05
0.00
-0.05
-0.10
-0.15
Shear Strain (%)
0
50
100
150
200
Time (sec)
Layer: 5 - EQ No: 1 - Outcrop: No

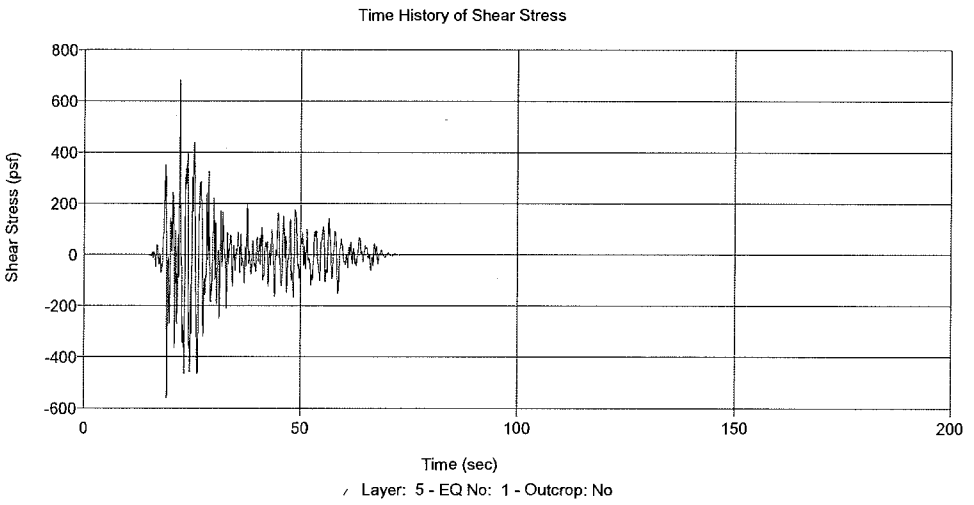
Time History of Shear Stress
800
600
400
200
0
-200
-400
-600
Shear Stress (psf)
0
50
100
150
200
Time (sec)
Layer: 5 - EQ No: 1 - Outcrop: No

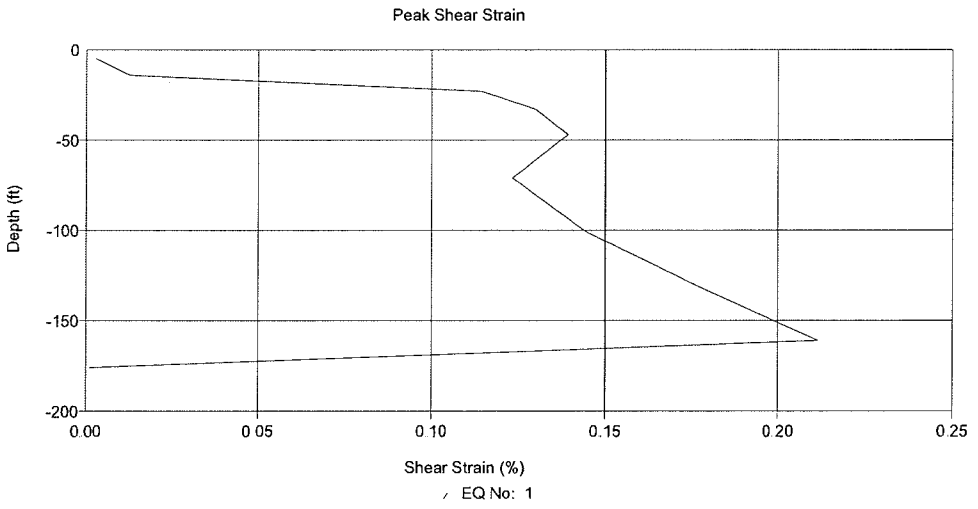
Peak Shear Strain
0
-50
-100
-150
-200
Depth (ft)
0.00
0.05
0.10
0.15
0.20
0.25
Shear Strain (%)
EQ No: 1

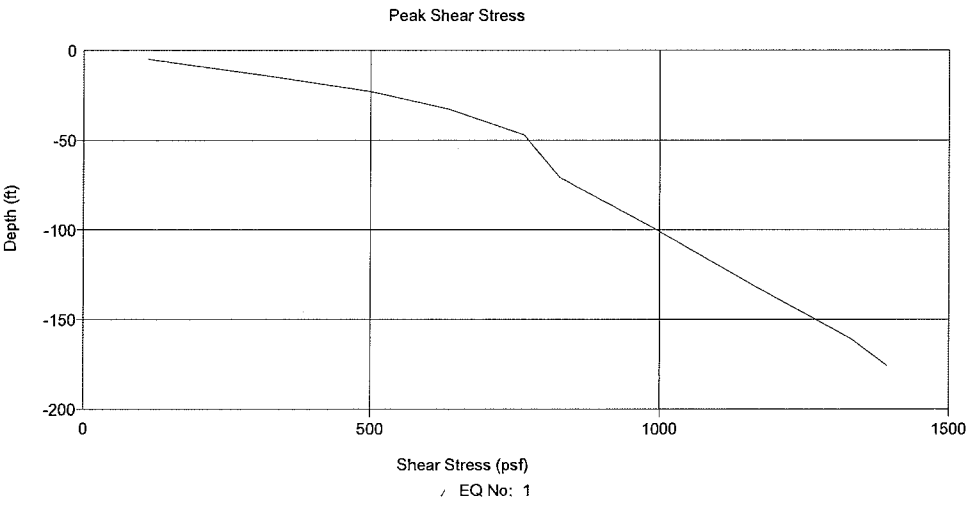
Peak Shear Stress
0
-50
-100
-150
-200
Depth (ft)
0
500
1000
1500
Shear Stress (psf)
EQ No: 1

3. Analysis A-3: Section A-A' with Input Motion El Centro (a_{max}=0.08g).

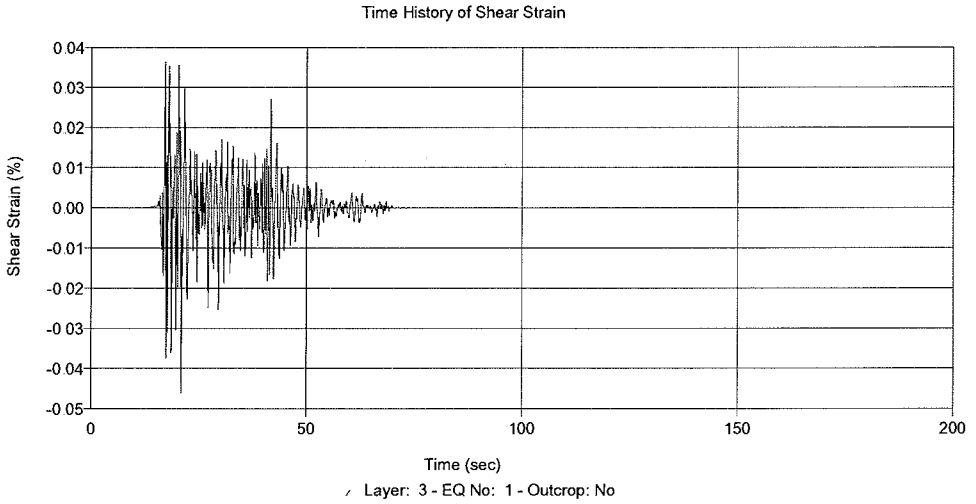

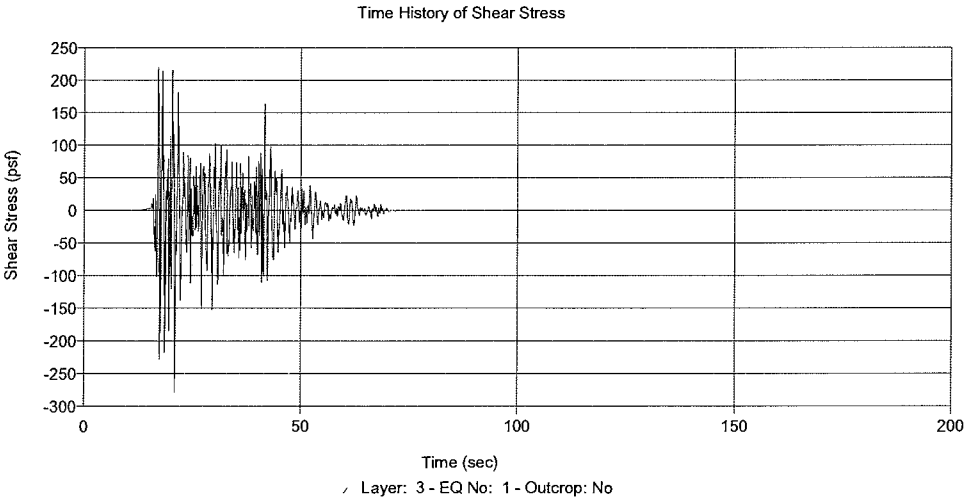

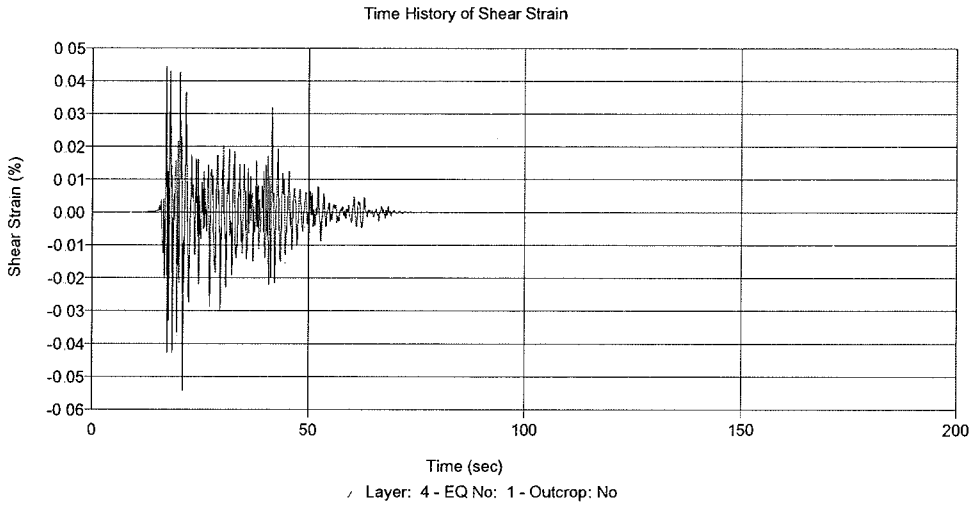
Time History of Shear Strain
0 05
0.04
0.03
0.02
0 01
0.00
-0 01
-0.02
-0 03
-0 04
-0.05
-0 06
Shear Strain (%)
0
50
100
150
200
Time (sec)
Layer: 4 - EQ No: 1 - Outcrop: No

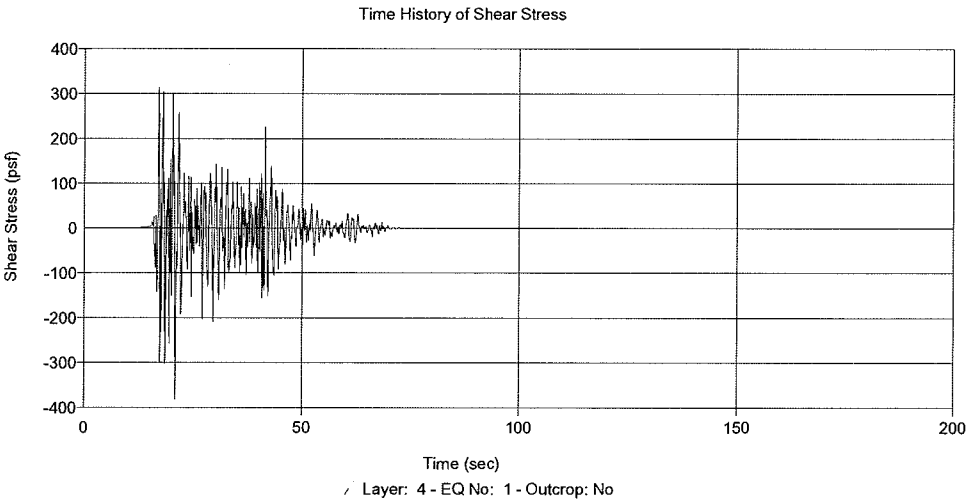
Time History of Shear Stress
400
300
200
100
0
-100
-200
-300
-400
Shear Stress (psf)
0
50
100
150
200
Time (sec)
Layer: 4 - EQ No: 1 - Outcrop: No

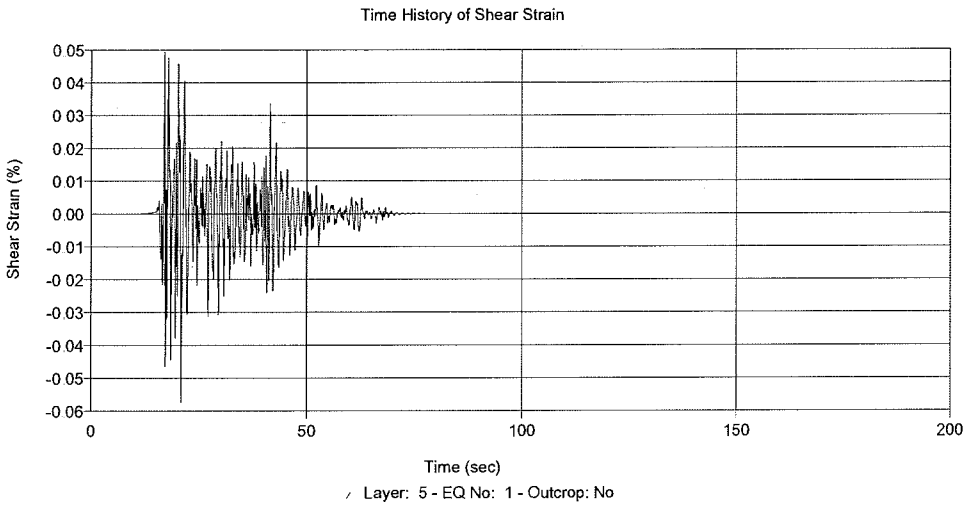
Time History of Shear Strain
Shear Strain (%)
0.05
0.04
0.03
0.02
0.01
0.00
-0.01
-0.02
-0.03
-0.04
-0.05
-0.06
0
50
100
150
200
Time (sec)
Layer: 5 - EQ No: 1 - Outcrop: No

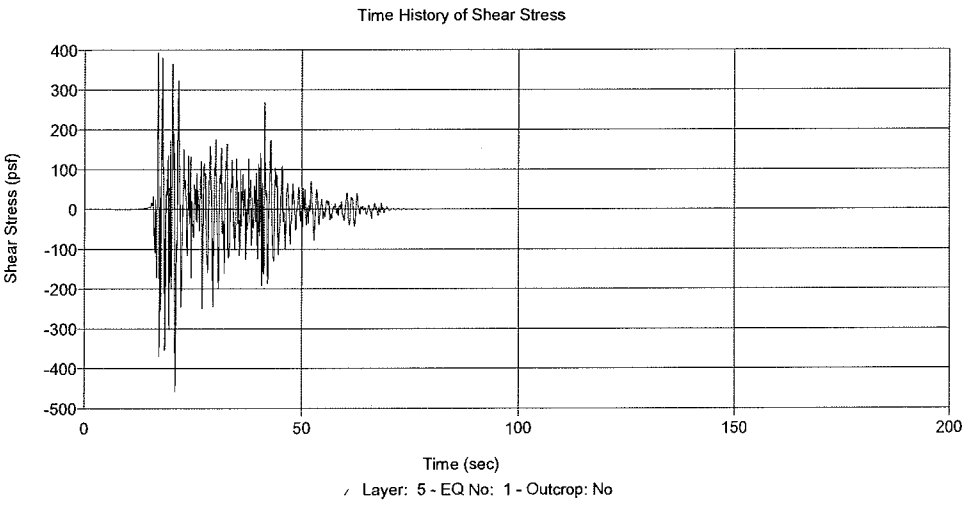
Time History of Shear Stress
Shear Stress (psf)
400
300
200
100
0
-100
-200
-300
-400
-500
0
50
100
150
200
Time (sec)
Layer: 5 - EQ No: 1 - Outcrop: No

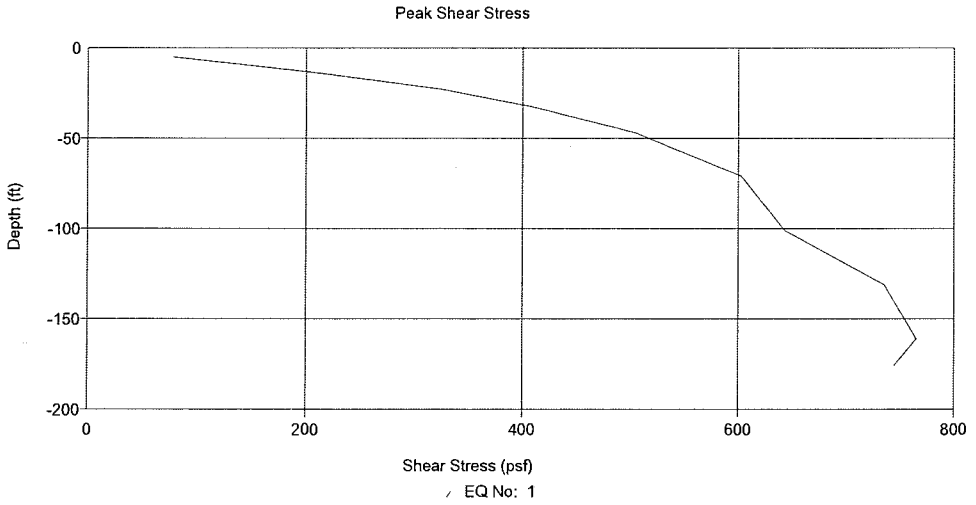
Peak Shear Stress
0
-50
-100
-150
-200
Depth (ft)
0
200
400
600
800
Shear Stress (psf)
EQ No: 1

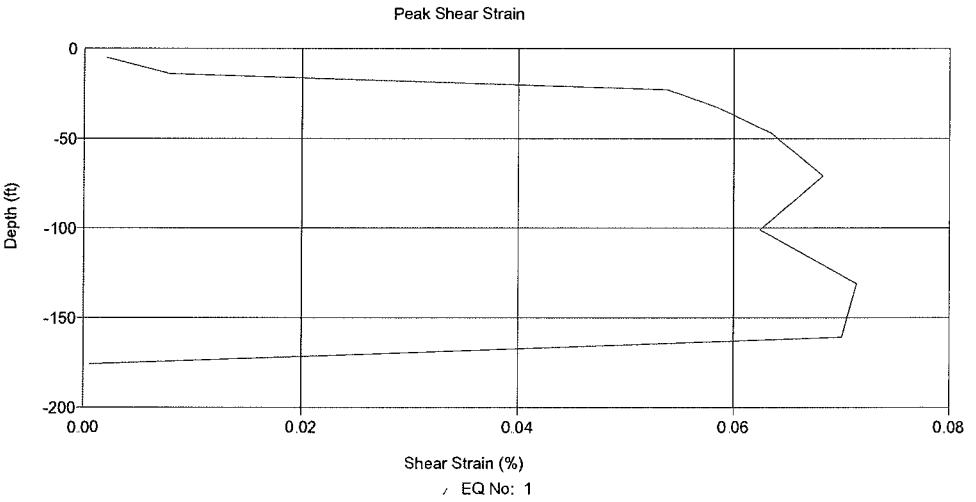
Peak Shear Strain
0
-50
-100
-150
-200
Depth (ft)
0.00
0.02
0.04
0.06
0.08
Shear Strain (%)
EQ No: 1

4. Analysis A-4: Section A-A' with Input Motion El Centro (a_{max}=0.15g).

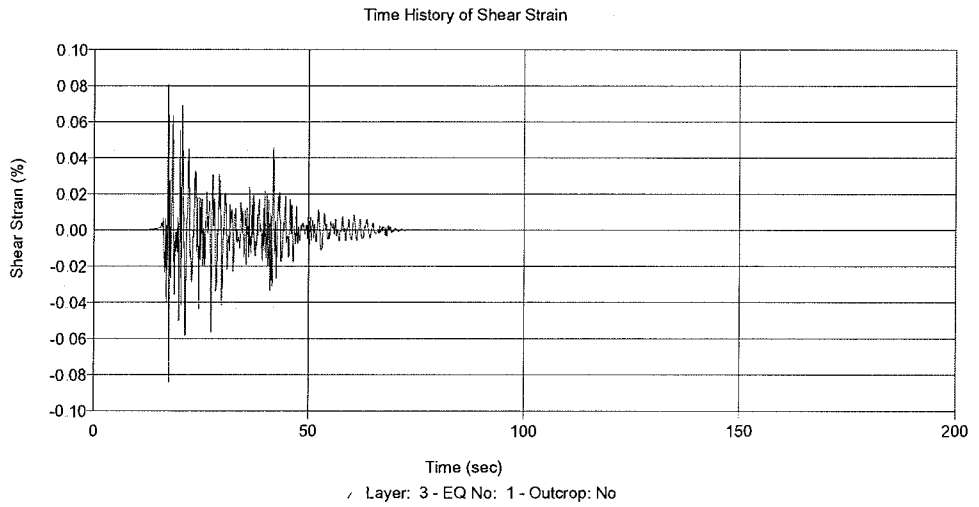

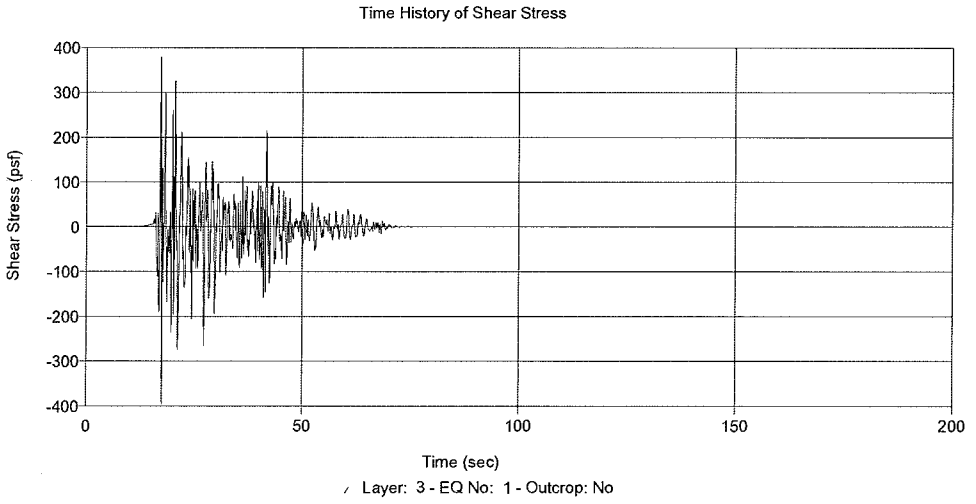

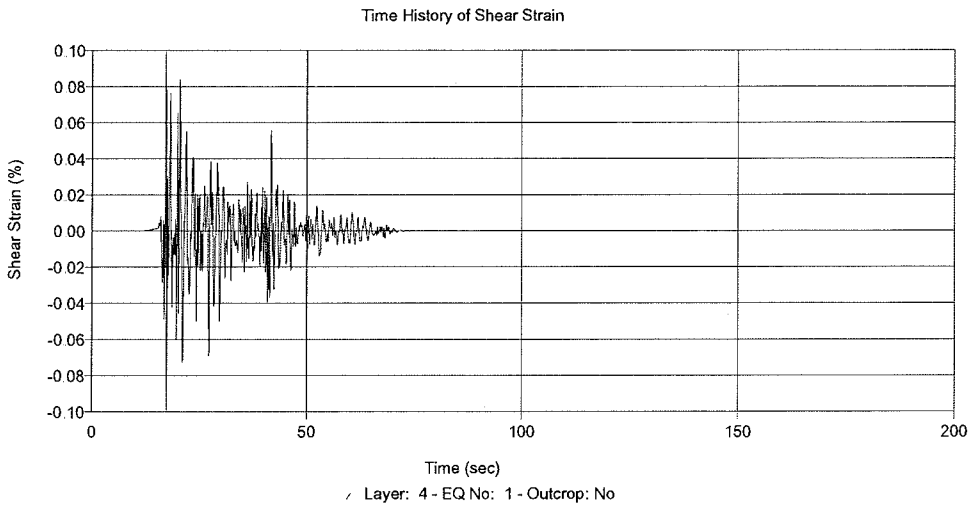
Time History of Shear Strain
Shear Strain (%)
0.10
0.08
0.06
0.04
0.02
0.00
-0.02
-0.04
-0.06
-0.08
-0.10
0
50
100
150
200
Time (sec)
Layer: 4 - EQ No: 1 - Outcrop: No

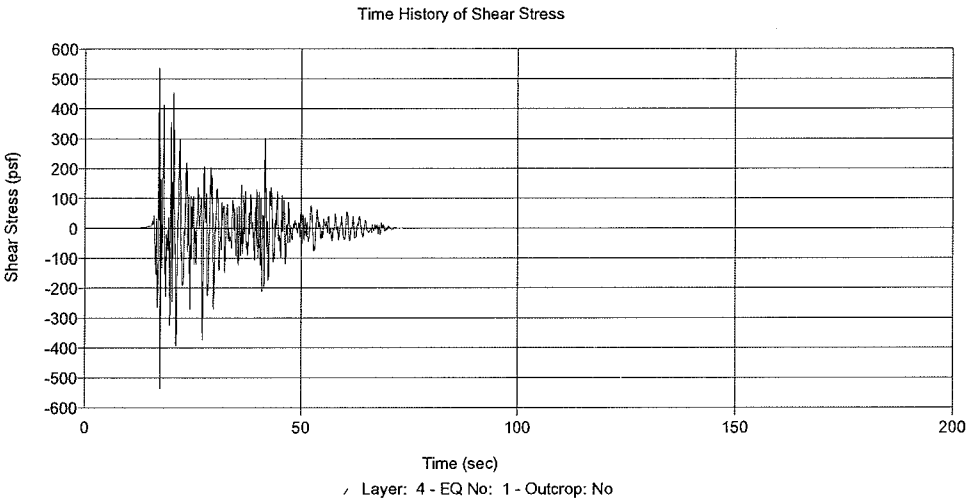
Time History of Shear Stress
Shear Stress (psf)
600
500
400
300
200
100
0
-100
-200
-300
-400
-500
-600
0
50
100
150
200
Time (sec)
Layer: 4 - EQ No: 1 - Outcrop: No

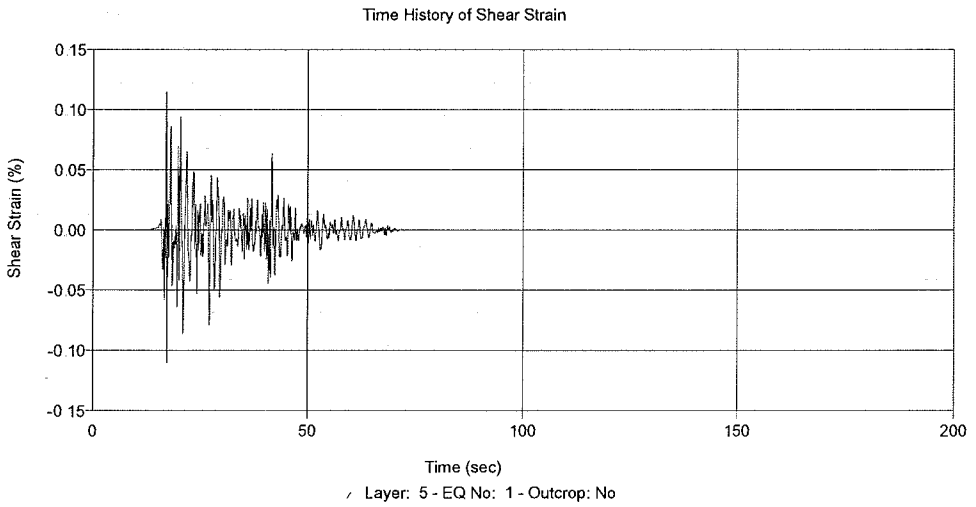
Time History of Shear Strain
0.15
0.10
0.05
0.00
-0.05
-0.10
-0.15
Shear Strain (%)
0
50
100
150
200
Time (sec)
Layer: 5 - EQ No: 1 - Outcrop: No

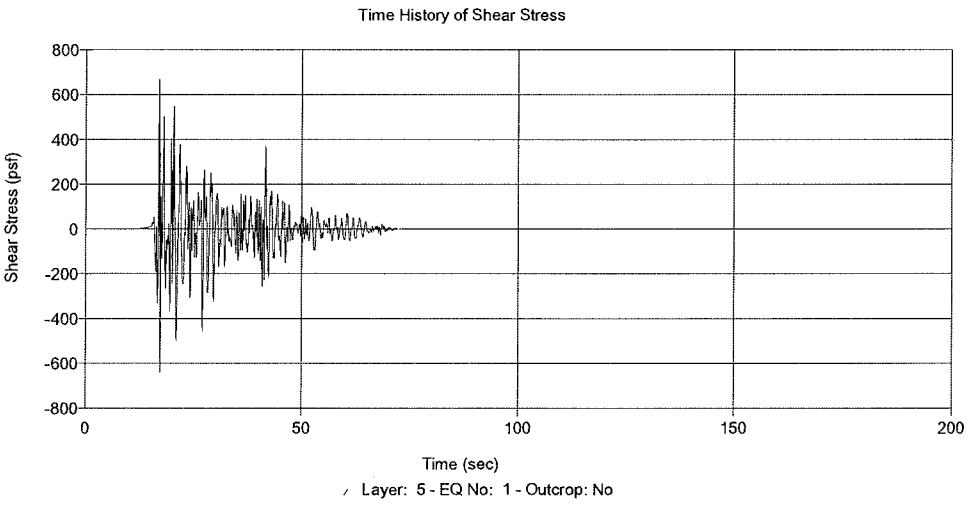
Time History of Shear Stress
800
600
400
200
0
-200
-400
-600
-800
Shear Stress (psf)
0
50
100
150
200
Time (sec)
Layer: 5 - EQ No: 1 - Outcrop: No

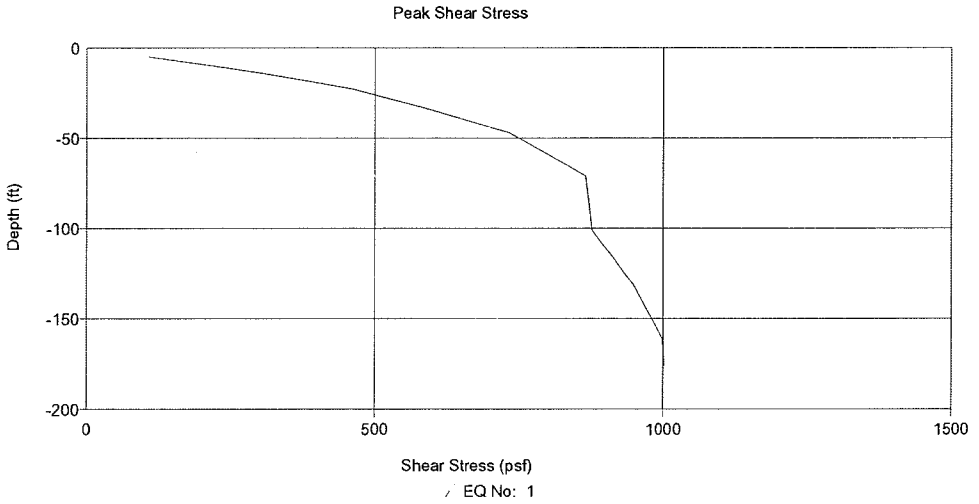

Peak Shear Strain (%)

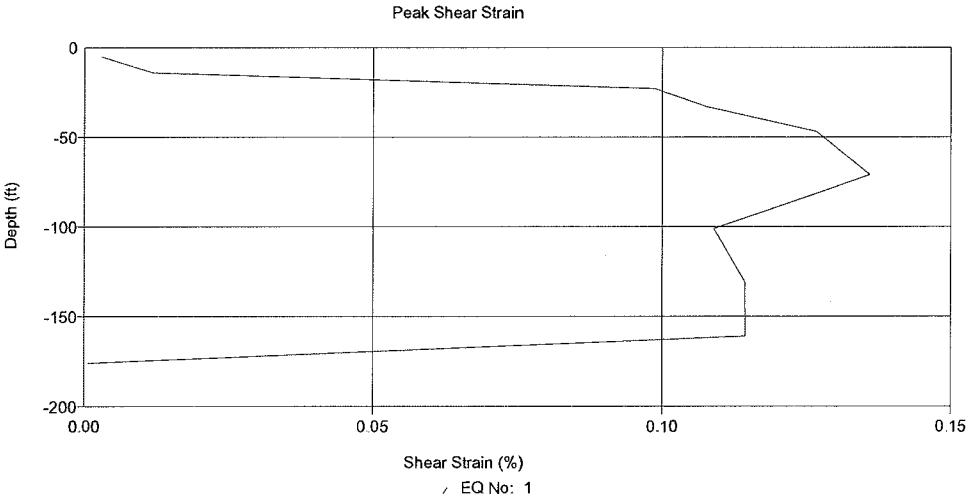

5. Analysis B-1: Section B-B' with Input Motion TAFT (a_{max}=0.08g).

Soil Profile

Profile Name: AEP impounded fly ash facility Section B-B'

Water Table: 66.00 ft

Number of Layers: 8

Input Motion

Number of Motions: 1

Number of Iterations: 5

Strain Ratio: 0.65

Tolerance: 5.00%

File Name	No of Acc. Values	Max. Acc. (g)	Time Step (sec)	Cuttoff Freq. (Hz)	No of Fourier Terms	Layer	Outcrop
D:\EDUSHAKE\TAFT.EQ	4220	**0.080**	0.020	20.00	8192	8	No

Output Locations

Layer No	Depth (ft)	Outcrop
1	0.00	No
3	26.00	No
4	36.00	No
5	46.00	No

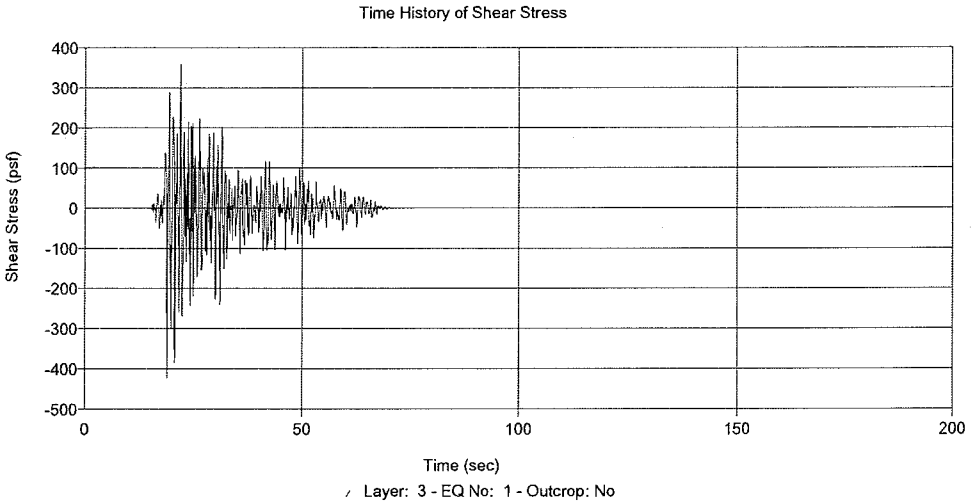
Time History of Shear Stress
Shear Stress (psf)
400
300
200
100
0
-100
-200
-300
-400
-500
0
50
100
150
200
Time (sec)
Layer: 3 - EQ No: 1 - Outcrop: No

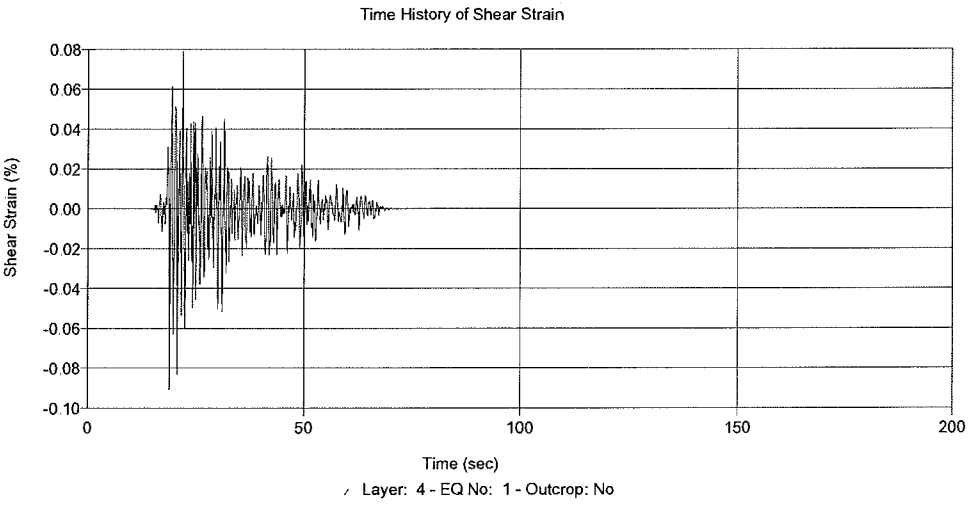
Time History of Shear Strain
Shear Strain (%)
0.08
0.06
0.04
0.02
0.00
-0.02
-0.04
-0.06
-0.08
-0.10
0
50
100
150
200
Time (sec)
Layer: 4 - EQ No: 1 - Outcrop: No

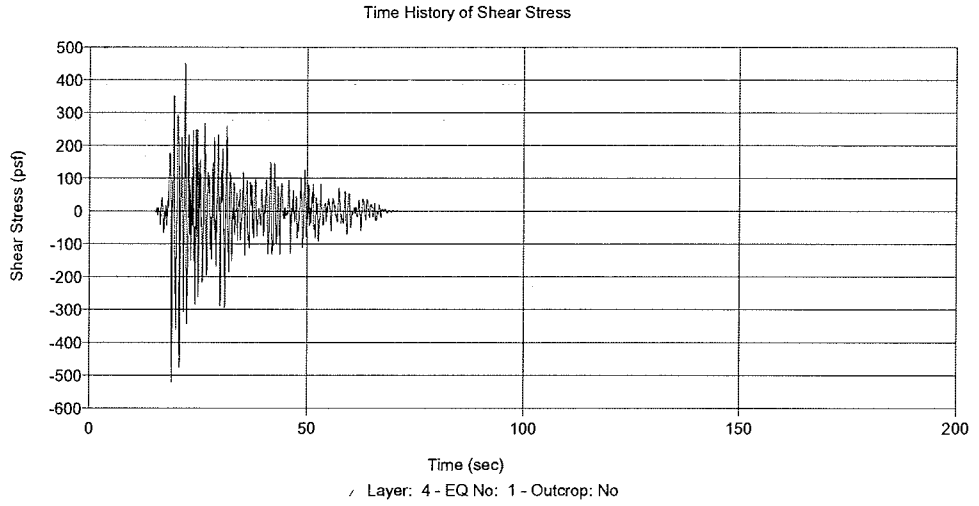
Time History of Shear Stress
Shear Stress (psf)
500
400
300
200
100
0
-100
-200
-300
-400
-500
-600
0
50
100
150
200
Time (sec)
Layer: 4 - EQ No: 1 - Outcrop: No

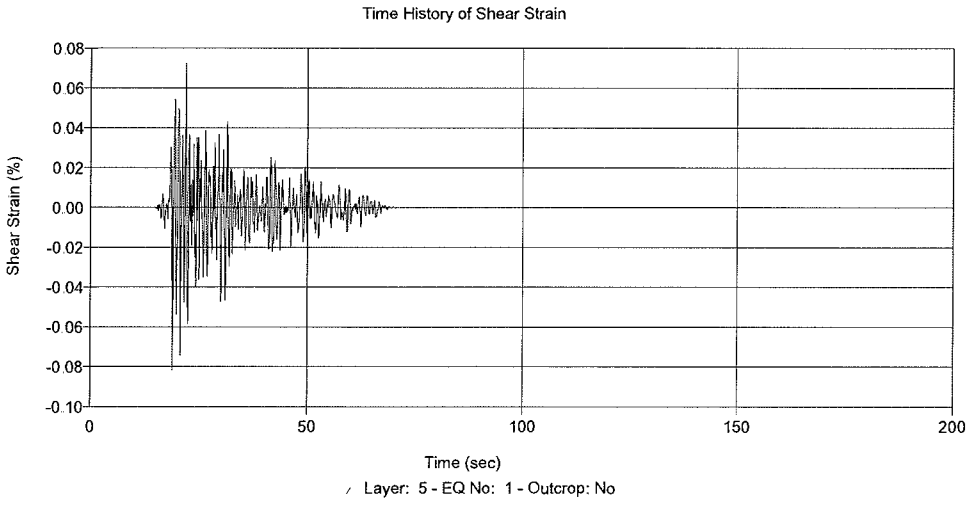
Time History of Shear Strain
Shear Strain (%)
0.08
0.06
0.04
0.02
0.00
-0.02
-0.04
-0.06
-0.08
-0.10
0
50
100
150
200
Time (sec)
Layer: 5 - EQ No: 1 - Outcrop: No

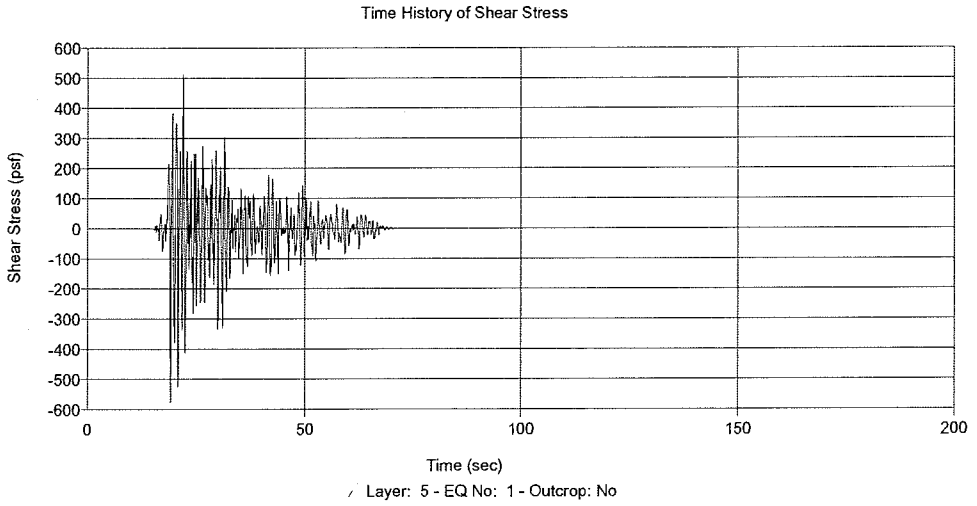

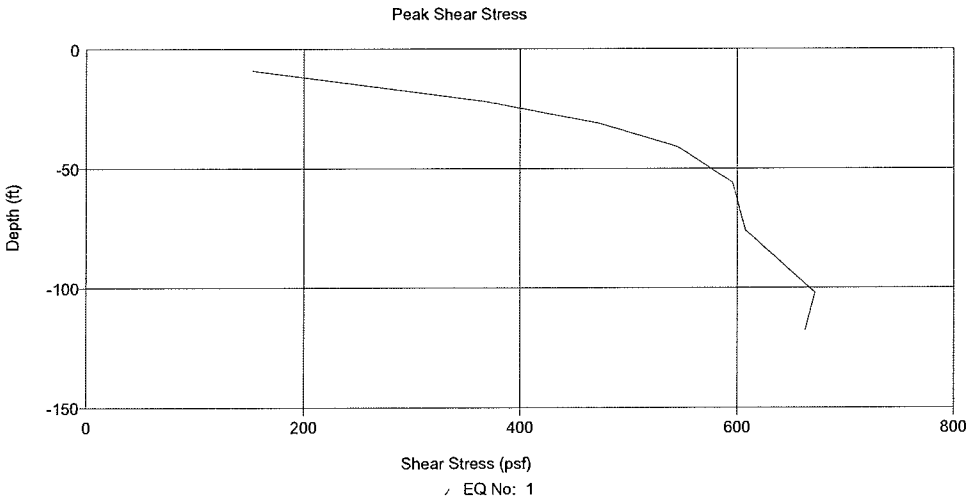

Peak Shear Strain (%)

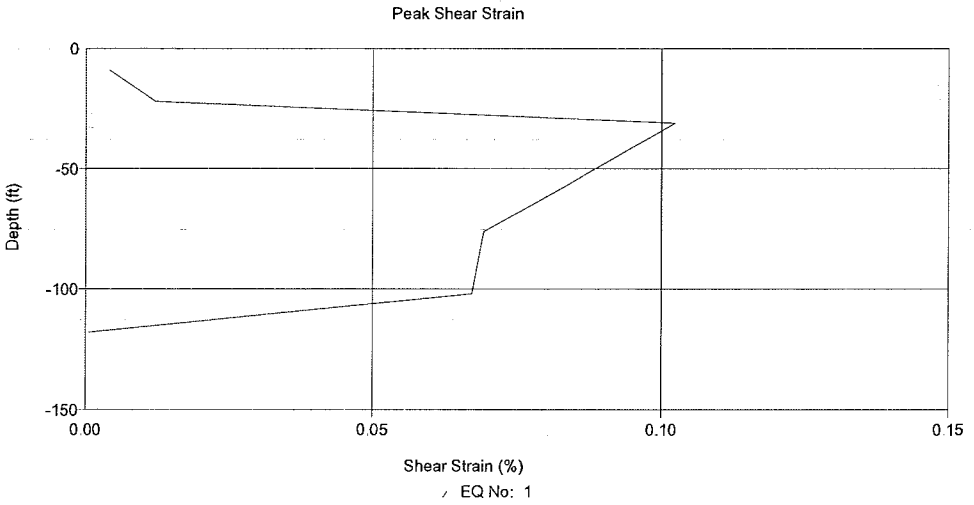
Peak Shear Strain
0
-50
-100
-150
Depth (ft)
0.00
0.05
0.10
0.15
Shear Strain (%)
EQ No: 1

6. Analysis B-2: Section B-B' with Input Motion TAFT (a_{max}=0.15g).

Input Motion

Number of Motions: 1

Number of Iterations: 5

Strain Ratio: 0.65

Tolerance: 5.00%

File Name	No of Acc. Values	Max. Acc. (g)	Time Step (sec)	Cuttoff Freq. (Hz)	No of Fourier Terms	Layer	Outcrop
D:\EDUSHAKE\TAFT.E Q	4220	0.150	0.020	20.00	8192	8	No

Output Locations

Layer No	Depth (ft)	Outcrop
1	0.00	No
3	26.00	No
4	36.00	No
5	46.00	No

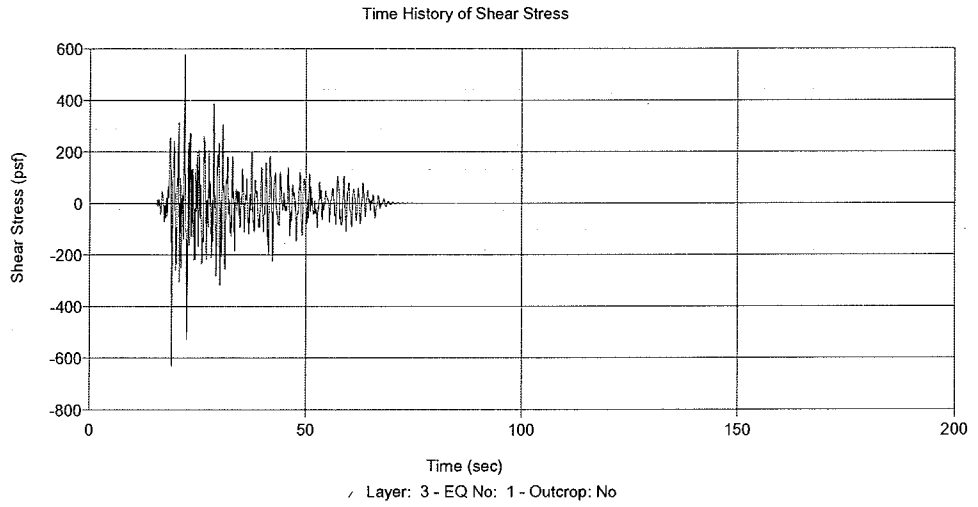
Time History of Shear Stress
600
400
200
0
-200
-400
-600
-800
Shear Stress (psf)
0
50
100
150
200
Time (sec)
Layer: 3 - EQ No: 1 - Outcrop: No

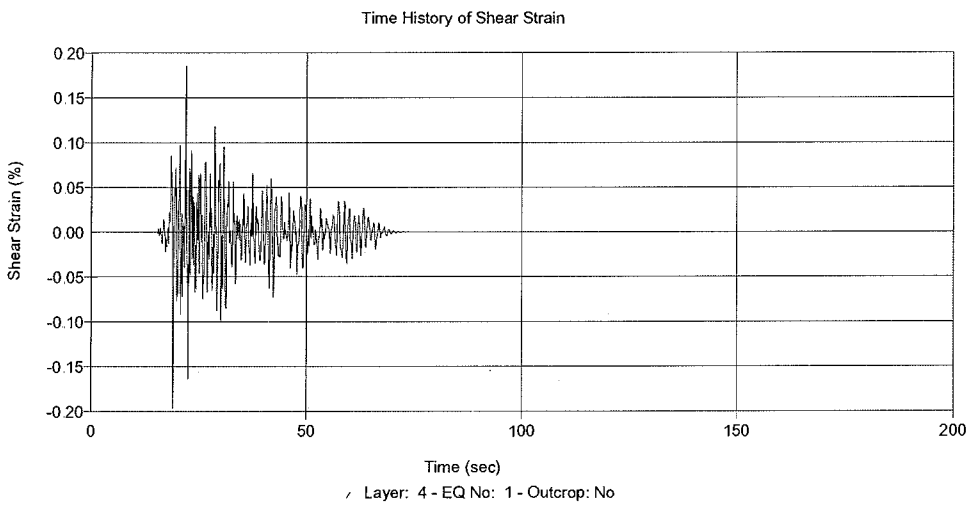
Time History of Shear Strain
0.20
0.15
0.10
0.05
0.00
-0.05
-0.10
-0.15
-0.20
Shear Strain (%)
0
50
100
150
200
Time (sec)
Layer: 4 - EQ No: 1 - Outcrop: No

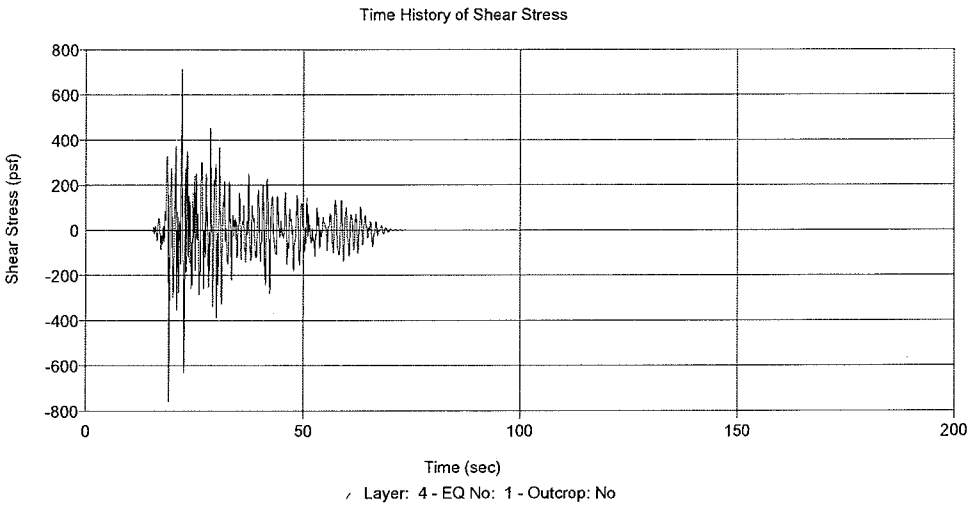
Time History of Shear Stress
800
600
400
200
0
-200
-400
-600
-800
Shear Stress (psf)
0
50
100
150
200
Time (sec)
Layer: 4 - EQ No: 1 - Outcrop: No

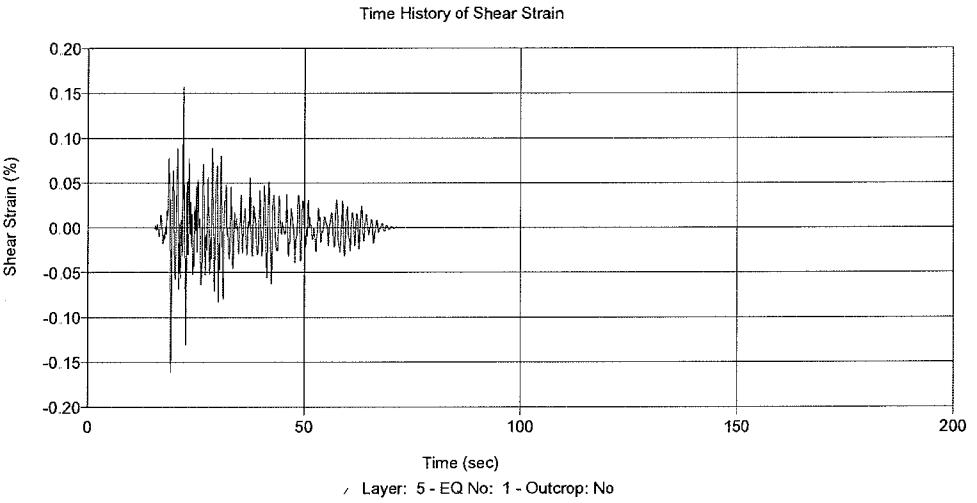
Time History of Shear Strain
0.20
0.15
0.10
0.05
0.00
-0.05
-0.10
-0.15
-0.20
Shear Strain (%)
0
50
100
150
200
Time (sec)
Layer: 5 - EQ No: 1 - Outcrop: No

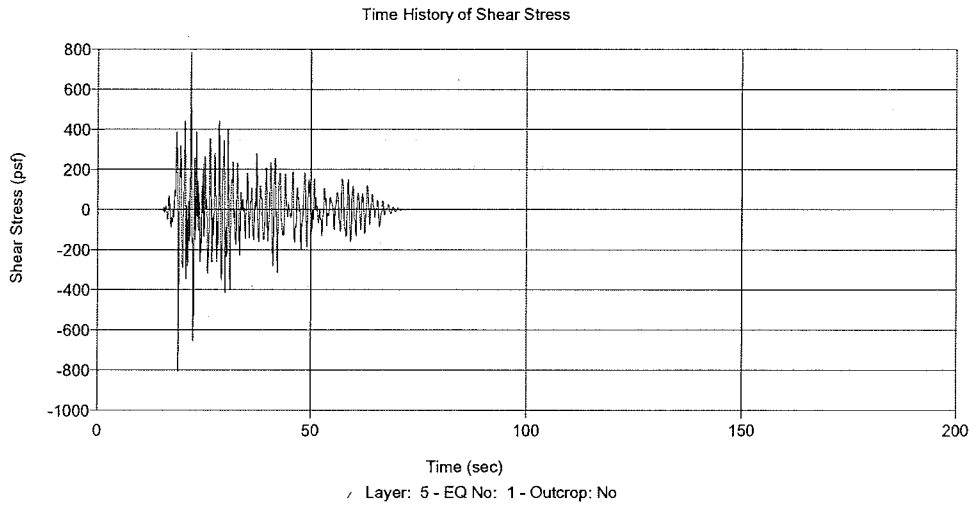

Peak Shear Strain (%)

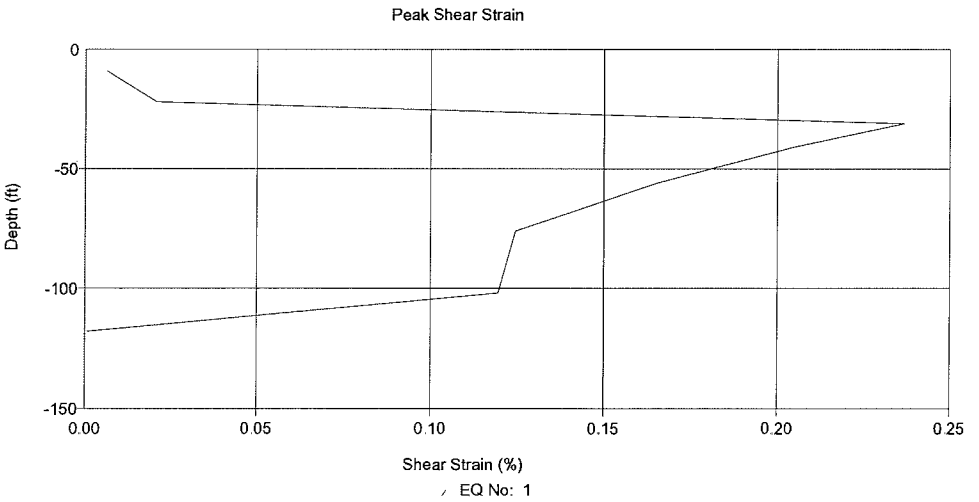

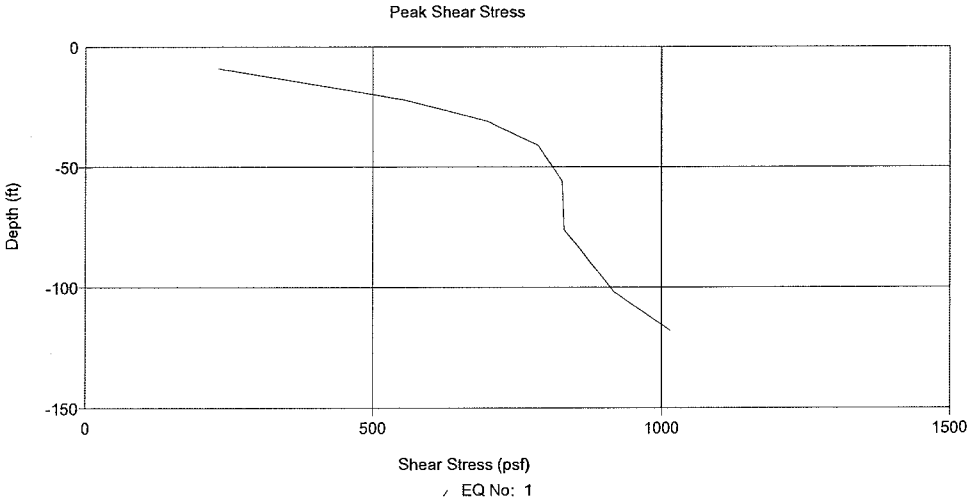
Peak Shear Stress
0
-50
-100
-150
Depth (ft)
0
500
1000
1500
Shear Stress (psf)
EQ No: 1

7. Analysis B-3: Section B-B' with Input Motion El Centro (a_{max}=0.08g).

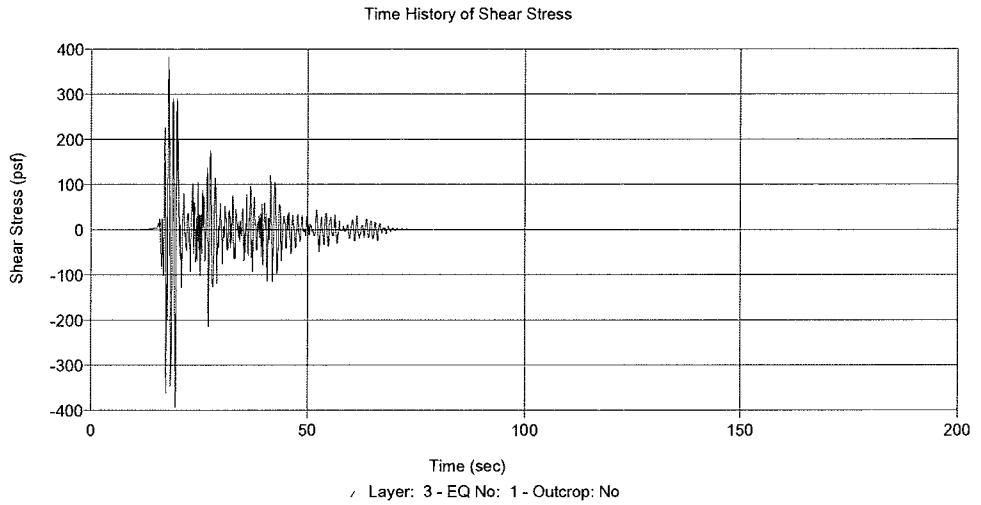

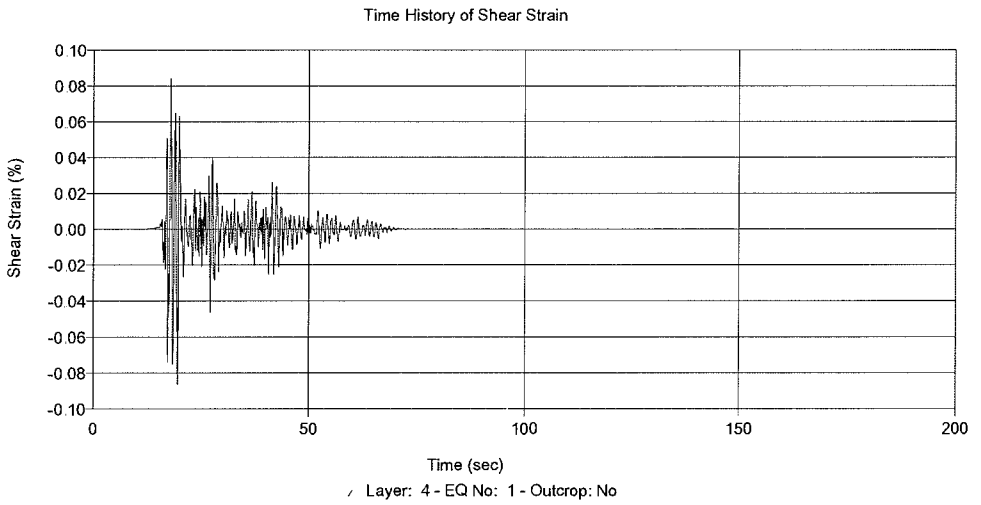

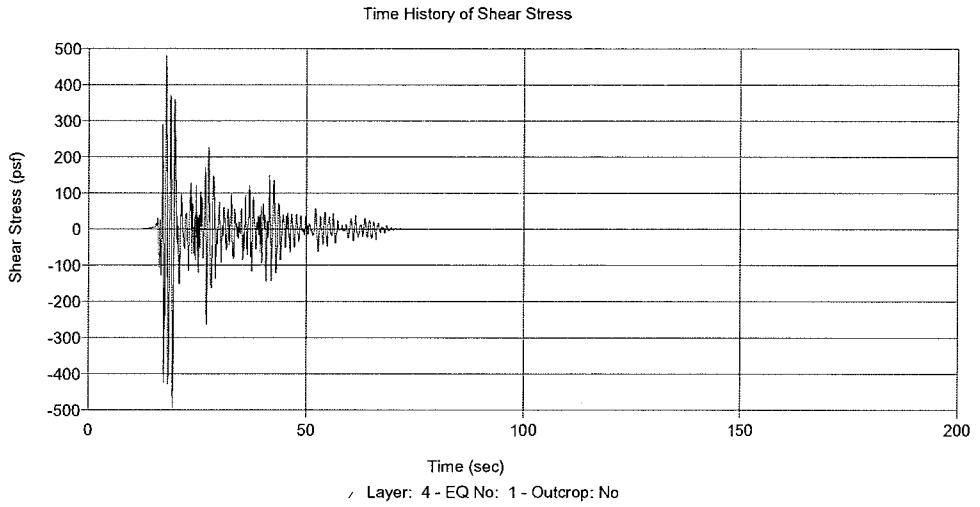
Time History of Shear Stress
Shear Stress (psf)
500
400
300
200
100
0
-100
-200
-300
-400
-500
0
50
100
150
200
Time (sec)
Layer: 4 - EQ No: 1 - Outcrop: No

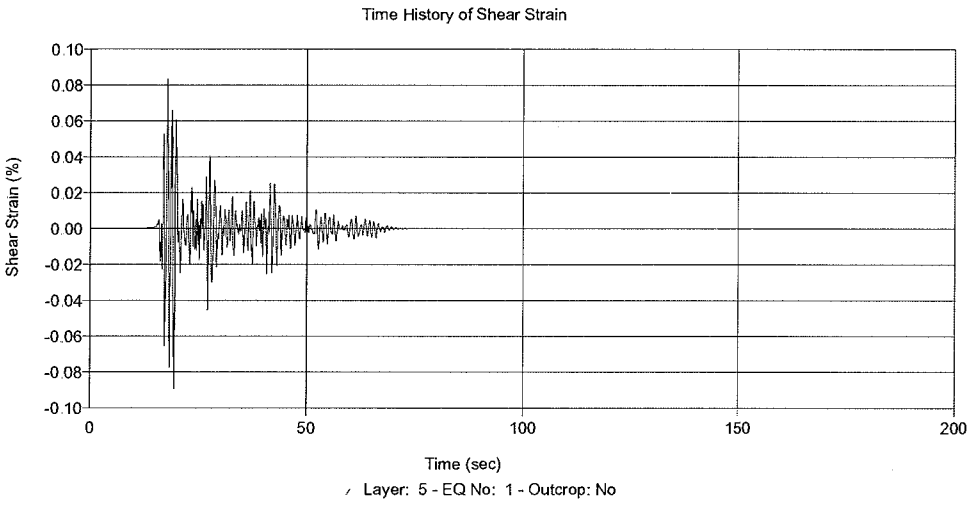
Time History of Shear Strain
Shear Strain (%)
0.10
0.08
0.06
0.04
0.02
0.00
-0.02
-0.04
-0.06
-0.08
-0.10
0
50
100
150
200
Time (sec)
Layer: 5 - EQ No: 1 - Outcrop: No

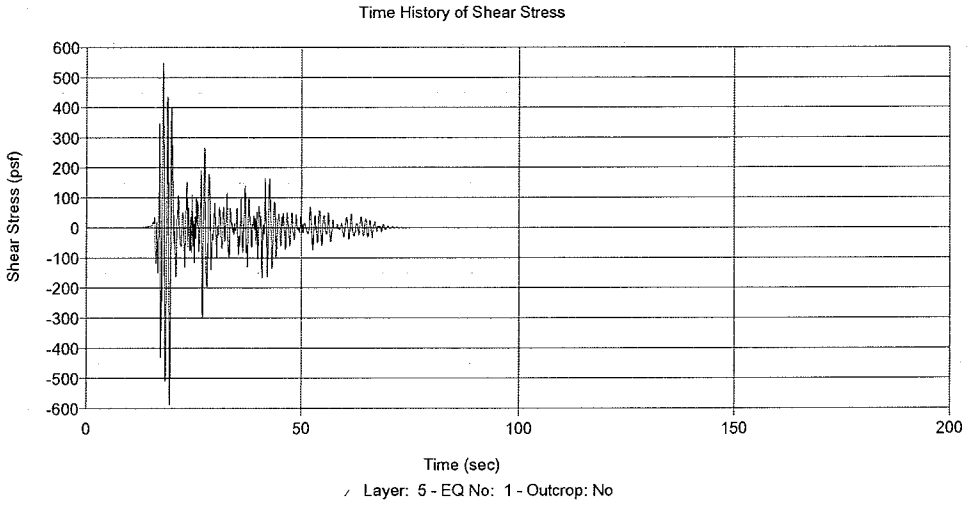

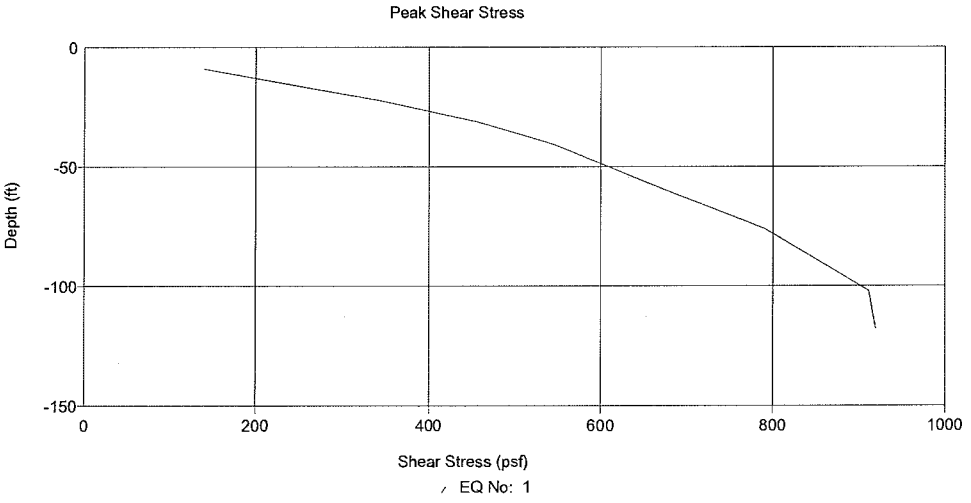

Peak Shear Strain (%)

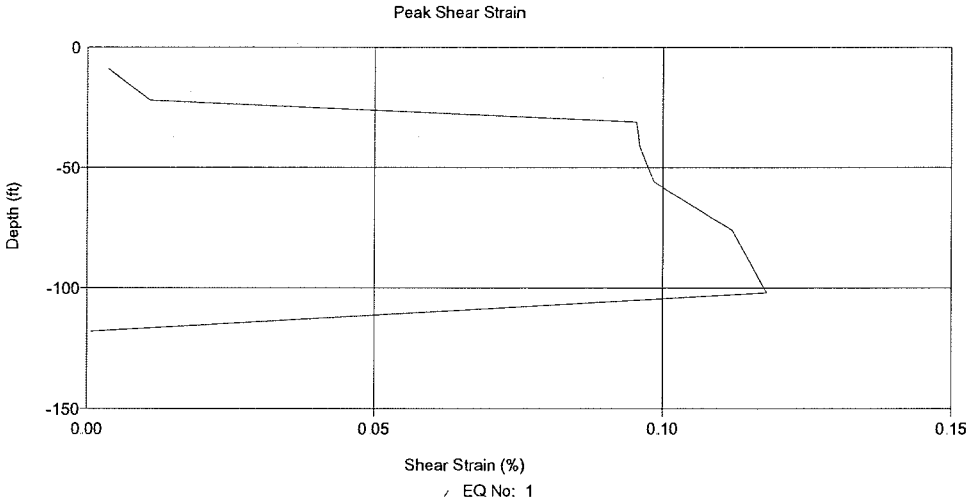
Peak Shear Strain
0
-50
-100
-150
Depth (ft)
0.00
0.05
0.10
0.15
Shear Strain (%)
EQ No: 1

8. Analysis B-4: Section B-B' with Input Motion El Centro (a_{max}=0.15g).

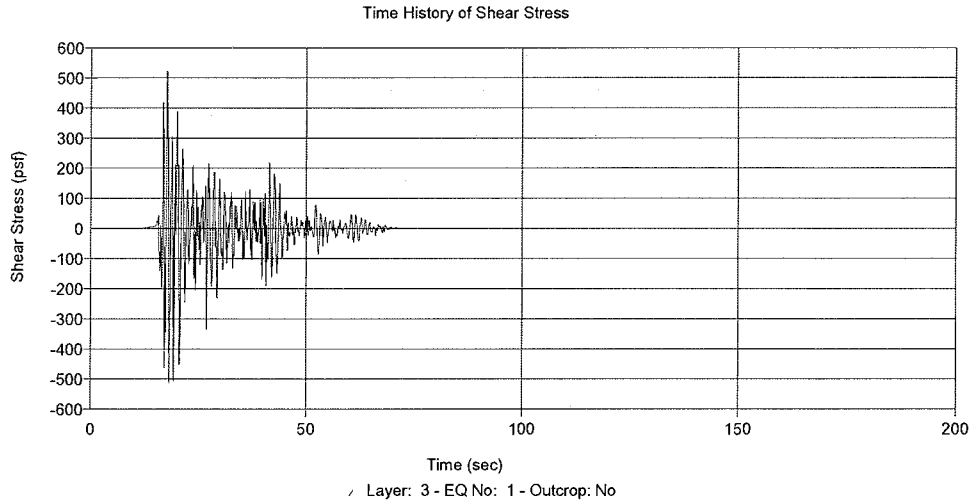

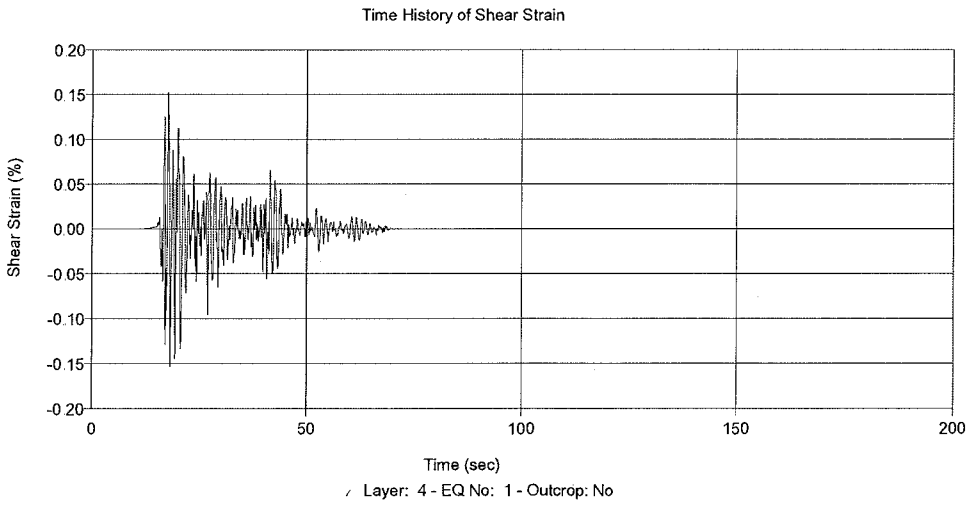

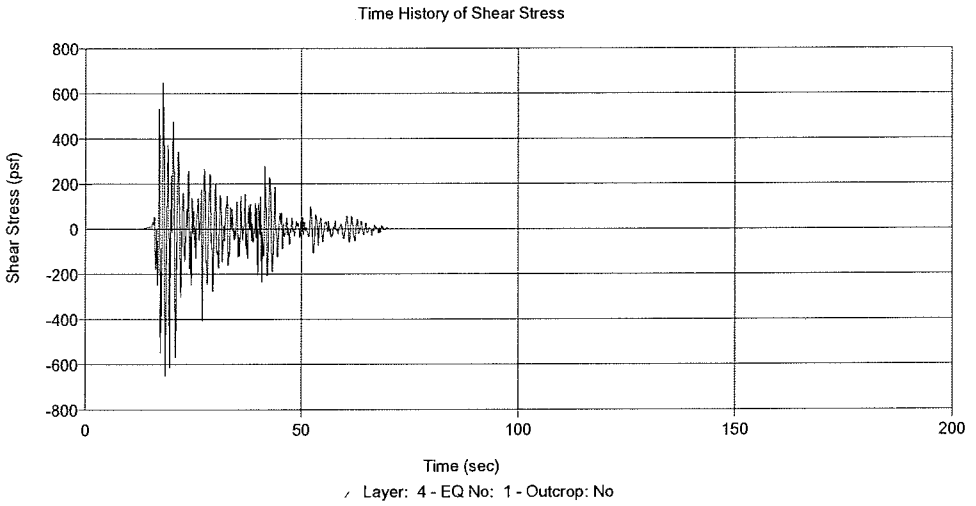
Time History of Shear Stress
800
600
400
200
0
-200
-400
-600
-800
Shear Stress (psf)
0
50
100
150
200
Time (sec)
Layer: 4 - EQ No: 1 - Outcrop: No

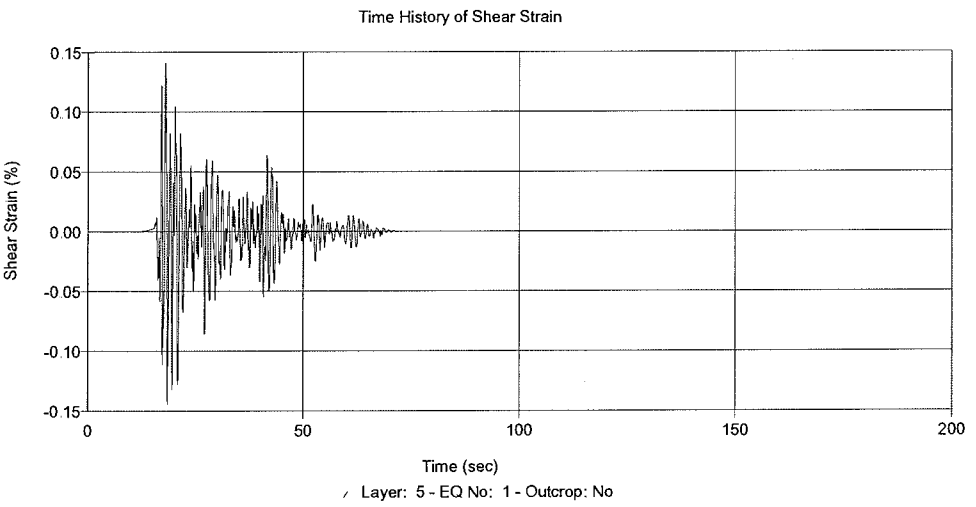
Time History of Shear Strain
0.15
0.10
0.05
0.00
-0.05
-0.10
-0.15
Shear Strain (%)
0
50
100
150
200
Time (sec)
Layer: 5 - EQ No: 1 - Outcrop: No

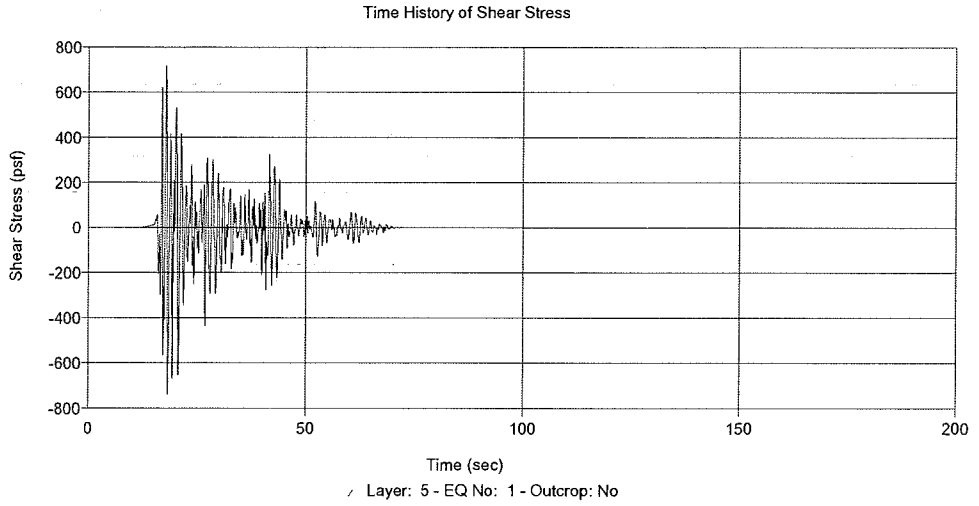
Time History of Shear Stress
800
600
400
200
0
-200
-400
-600
-800
Shear Stress (psf)
0
50
100
150
200
Time (sec)
Layer: 5 - EQ No: 1 - Outcrop: No

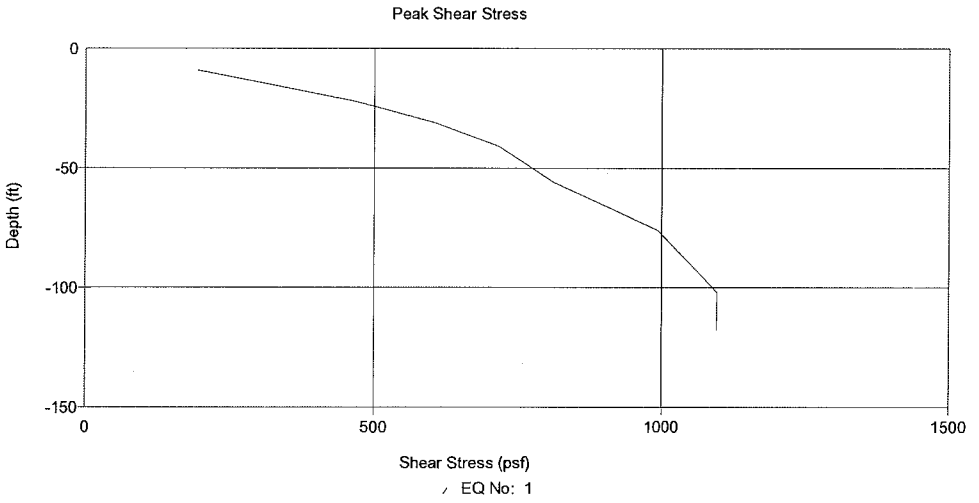
Peak Shear Stress
0
-50
-100
-150
Depth (ft)
0
500
1000
1500
Shear Stress (psf)
EQ No: 1

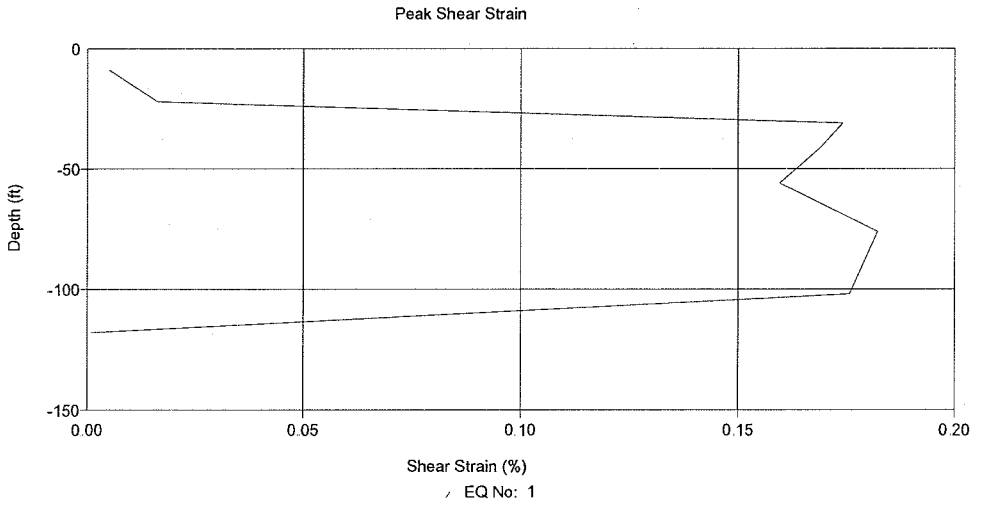
Peak Shear Strain
0
-50
-100
-150
Depth (ft)
0.00
0.05
0.10
0.15
0.20
Shear Strain (%)
EQ No: 1

Appendix C

ASTM D5311

An Experimental Investigation on Liquefaction Potential and Post Liquefaction Shear Strength of Impounded Fly Ash

Behrad Zand[1*], Wei Tu[2], Pedro J. Amaya[3], William E. Wolfe[4], Tarunjit Butalia[5]

[1]Graduate Research Associate, Department of Civil and Environmental Engineering and Geodetic Science, The Ohio State University, 470 Hitchcock Hall, 2070 Neil Ave., Columbus, OH 43210, US, Tel: (614) 292-0992, Fax: (614) 292-3780, E-mail: zand.3@osu.edu

[2] PE, Graduate Research Associate, Department of Civil and Environmental Engineering and Geodetic Science, The Ohio State University, E-mail: tu.45@osu.edu

[3] PE, Senior Geotechnical Engineer, Civil Engineering Division, American Electric Power, Service Corporation, 1 Riverside Plaza, Columbus, OH 43215-2373, US, Tel: (614) 716-2926, E-mail: pjamaya@aep.com

[4] PhD, PE, Professor, Department of Civil and Environmental Engineering and Geodetic Science, The Ohio State University, Tel: (614) 292-0790, E-mail: wolfe.10@osu.edu

[5] PhD, PE, Research Scientist, Department of Civil and Environmental Engineering and Geodetic Science, The Ohio State University, E-mail: butalia.1@osu.edu

[*] Corresponding author

Abstract

Liquefaction resistance and post liquefaction shear strength of impounded class F fly ash is investigated using laboratory experiments. The study was aimed to evaluate liquefaction potential for a 45 hectare impoundment proposed as a base for a utility monofill. The evaluation included cyclic triaxial tests performed on reconstituted fly ash specimens with various densities at different confining stresses and cyclic stress ratios representative of the impounded material and the seismic environment. The results are presented in the form of design charts. Post-liquefaction strengths were measured by reconsolidating the specimens at the initial effective confining stress and performing undrained triaxial tests. The measured cyclic strength was compared with the seismically induced stresses in the profile using one dimensional wave propagation method. The cyclic loadings imposed on the ash by the design earthquakes were found to be lower than the measured cyclic strength of the material. The post liquefaction shear strengths showed some scatter, however they are typically higher than the initial shear strengths before exposure of the material to cyclic load.

Key Words: Impounded Fly Ash, Liquefaction Potential, Post Liquefaction Shear Strength, Dynamic Triaxial Test, Ground Response Analysis

1. Introduction

American Coal Ash Association survey[1] estimates the total fly ash production in US to be 65 million tons (71 million US tons) in 2005, from which only 41% was reused and the rest was left to be disposed in storage ponds or landfills. This fact combined with the increasing landfill coasts highlights the need for innovative methods to exploit full capacity of existing fly ash landfills/impoundments. A 45 hectares fly ash impoundment

(Figure 1), owned by American Electric Power (AEP) was proposed as the base for a utility monofill. The liquefaction potential of fly ash during earthquake was a concern of the design team. Although a large amount of literature exists on the cyclic resistance of sands and clayey soils (Ref. 2 to 9) little has been done for fly ash. To address this concern an experimental program combined with a ground response analysis was conducted to evaluate the liquefaction potential of the impoundment and the post liquefaction shear strength of the material. The cyclic strength of the material was evaluated using standard cyclic triaxial test[10], and the initial and post liquefaction shear strengths were evaluated using undrained shear (CU) test[11].

2. Testing Program and Specimen Preparation

a) Material Properties

Class F fly ash produced by AEP's Mitchell power plant was collected from the impoundment located in West Virginia and used in this study. A gradation curve, supplied by AEP, is presented in Figure 2, showing that in terms of particle size the material is similar to silts. A specific gravity of 2.27 was measured by AEP. The in-situ density of the material was determined by AEP to range from 1600 to 1680 kg/m^3 with a moisture content of about 30%. The in-situ dry density of the material is estimated to range from 92% to 96% of the optimum Proctor dry density[12].

Figure 1. Mitchell fly ash impoundment in West Virginia

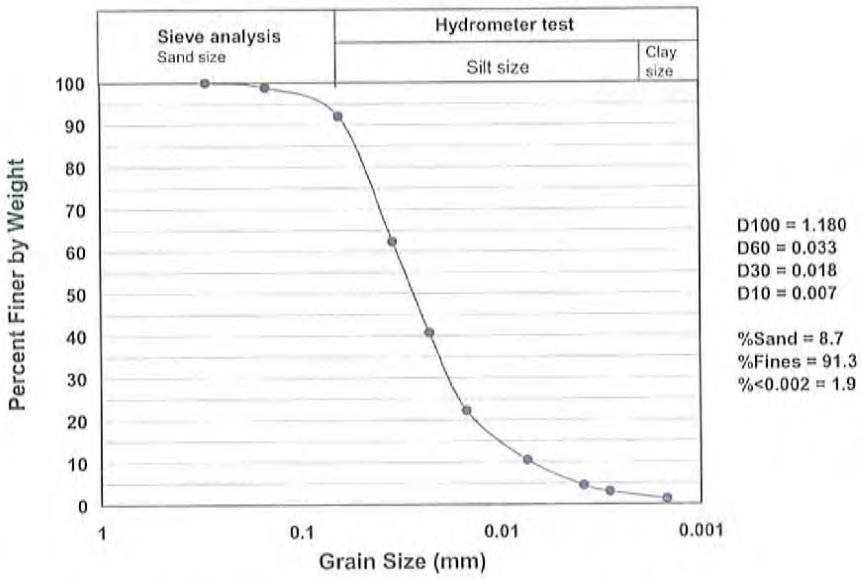

Figure 2. Grain size distribution of Mitchell fly ash

b) Specimen Preparation

Fly ash specimens were made in Harvard miniature mold (3.35 cm diameter, 7.11 cm length) using wet tamping to achieve target densities of 86%, 95%, and 104% of the optimum standard Procter dry density. Specimens were compacted in five equal lifts using a 110 N (25 lb) hand tamper. Figure 3 shows a comparison between the standard Proctor and the Harvard miniature calibration curves. Saturation of the specimens were achieved by application of a small vacuum pressure (<60 kPa) followed by a back pressure of 105 to 310 kPa. All the specimens tested possessed a B-value larger than 97%. The average time needed to saturate the specimens varied from one day to two weeks.

c) Cyclic Triaxial Test

Specimens were consolidated under effective stresses of 68, 135, and 340 kPa, representing typical depths of 3.5, 7, and 20 m, respectively, and were tested under cyclic shear stress ratios ranging from 7.5 to 40% of the effective confining stress. Due to the high permeability of the material (of the order of 10^{-4} cm/sec) the consolidation occurred rapidly. The cyclic test was conducted under undrained conditions and constant cell pressure. The loading frequency was selected to be 0.5 Hz except for one case where a frequency of 1 Hz was used. A 450 Newton load cell was utilized to control load cycles in load control mode while axial deformations were measured by a LVDT attached to loading piston. Specimen pore water pressure and deformation, as well as the deviator load were recorded continuously at a sampling rate of 100 Hz. As shown in Figure 4, liquefaction was defined as the point at which the excess pore water pressure reached the asymptotic level of the initial effective confining pressure accompanied with a dramatic increase in the axial deformation.

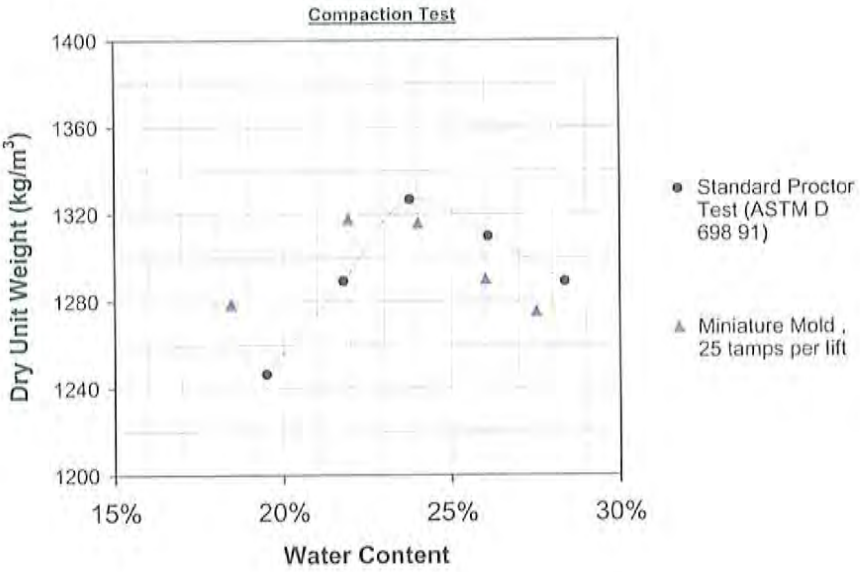

Figure 3. Calibration of compaction effort for Harvard Miniature samples

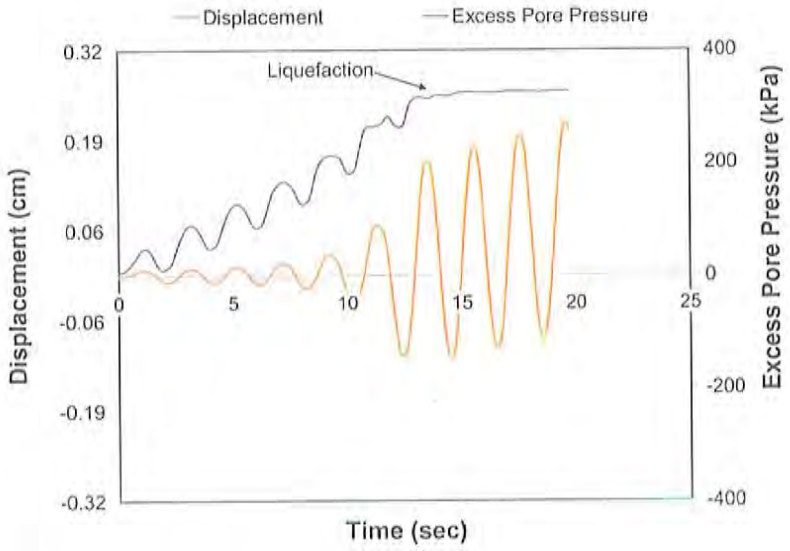

Figure 4. Identification of liquefaction for cyclic triaxial tests

d) *Consolidated Undrained (CU) Shear Test*

CU tests were performed to establish the initial static undrained shear strength of the fly ash material. Additional post-liquefaction CU test was conducted on selected specimens to determine the static undrained shear strength after the earthquake event. The tests were conducted using a strain control load frame and specimen pore water pressure was measured during the test to determine effective stresses and friction angle.

3. Results and Discussion

a) Laboratory Testing

Presented in Table 1 is a list of the specimens tested under cyclic loading together with their relative dry density, effective confining pressure, and shear stress ratios (deviator stress divided by twice effective stress). Figure 5 shows the cyclic test results for the fly ash specimens subjected to consolidation stress of about 135 kPa. The number of loading cycles to produce liquefaction (N) is seen to decrease with increasing shear stress ratio and decreasing initial density. On the bases of these results design curves are established and presented in the figure, which express the liquefaction resistance (shear stress ratio) as a function of N and density. Using these curves, another family of curves, presented in Figure 6, was derived expressing N as a function of initial density and shear stress ratio for specimens consolidated under 135 kPa effective stress.

From Table 1, it can be seen that the initial densities of specimens occasionally deviate from the target value by a small amount. Figure 6 shows that N is not sensitive to small variation in the initial density when the shear stress ratio is relatively high. However, for specimens with higher initial densities tested under stress ratios lower than 0.13, small

variation in the initial density can influence the results. For instance, the actual density for specimen tested under shear stress ratio of 0.11 (95C-135-11) was 0.96% versus the target value of 0.95%. Figure 6 shows that for this stress ratio N decreases by 25 cycles when the relative density decreases from 96% to 95%. The corrected results for 95% and 104% relative density specimens are superimposed in Figure 5. There are only two data points for which the difference is apparent. Similar corrections for 86% density specimens do not change the results because the corrections are fractions of a cycle. The established curves in the figure are still in agreement with the corrected results and they do not need to be revised.

Specimen ID	Initial Compaction	Confining Stress (kPa)	$\frac{\sigma_d}{2\sigma_C}$
85C-135-8 *	87%	135	7.5%
85C-135-10*	86%	135	10%
85C-135-13 *	86%	135	13%
85C-135-15	85%	135	15%
85C-135-20*	87%	135	20%
95C-68-16 *	95%	68	16%
95C-68-17	96%	68	17%
95C-68-18	96%	68	18%
95C-68-20 *	95%	68	20%
95C-68-21	95%	68	21%
95C-68-26	95%	68	26%
95C-68-40	94%	68	40%
95C-135-10a	95%	135	10%
95C-135-10b	95%	135	10%
95C-135-11	96%	135	11%
95C-135-13 *	95%	135	13%
95C-135-15	95%	135	15%
95C-135-21 *	95%	135	21%
95C-135-25	95%	135	25%
95C-340-10 *	95%	340	10%
95C-340-11	95%	340	11%
95C-340-12	97%	340	12%
95C-340-15	95%	340	15%
95C-340-20	95%	340	20%
95C-340-37	95%	340	37%
105C-135-14 *	103%	135	20%
105C-135-20 *	104%	135	20%

* Post-liquefaction CU test conducted

Table 1. List of specimens and loading conditions for cyclic tests

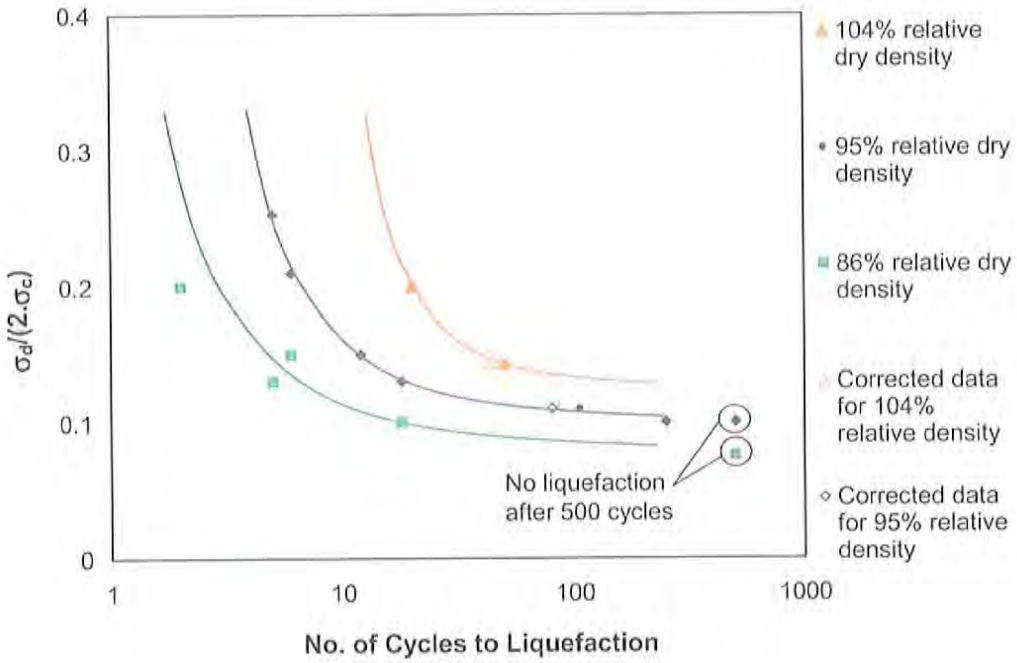

Figure 5. Laboratory cyclic test results for confining stress of 135 kPa, showing effect of density on liquefaction resistance

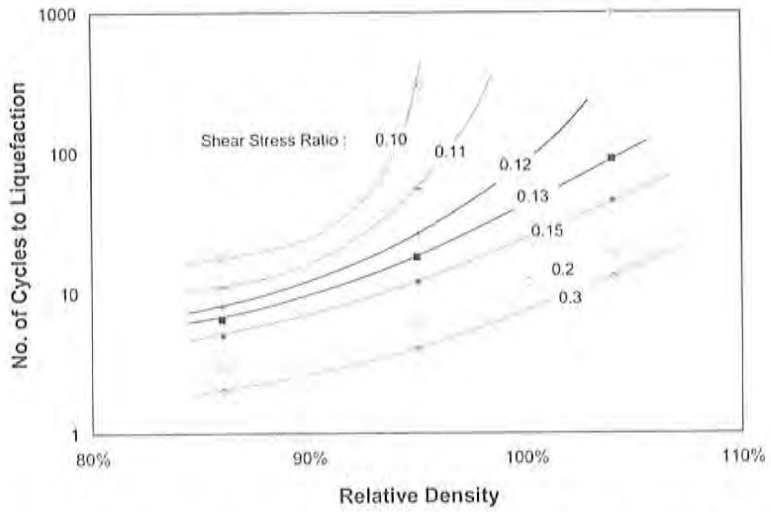

Figure 6. Number of cycles to produce liquefaction as a function of initial density and shear stress ratio

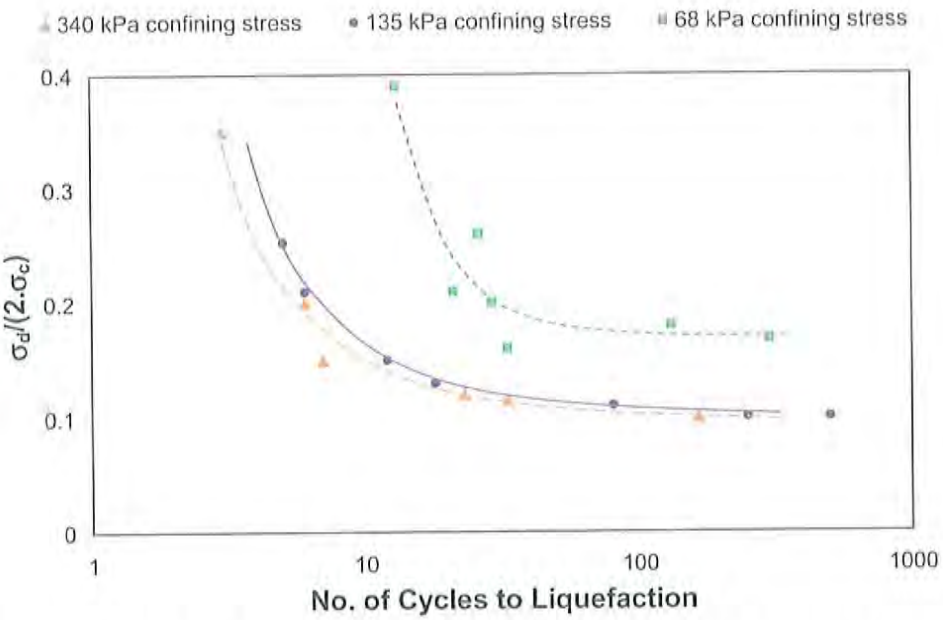

Figure 7. Laboratory cyclic test results for 95% relative density specimens showing the effect of confining stress

Presented in Figure 7 are the results of cyclic tests conducted on specimens with 95% of optimum Proctor initial density subjected to various confining stresses. The two curves that represent 135 and 340 kPa effective confining stresses are very close; suggesting that as confining stress increases liquefaction resistance becomes less sensitive to the confining stress.

After liquefaction, selected specimens (see Table 1) were re-consolidated and the post-liquefaction undrained shear strengths were measured. Table 2 presents a summary of these test results at the peak point and 10% axial strain. Also included are the maximum axial strains experienced during the cyclic test. These data were used to calculate internal friction angle for the material (cohesion is zero), and the results are presented in Figure 8. For those specimens which did not exhibit a peak in their shear strength, the shear stress at 10% axial strain was used. This figure also contains results from pre-liquefaction CU tests conducted on 5 specimens at relative densities of 86%, 95%, 97%, 103%, and 104%. The first specimen (86% relative density) was consolidated under 103 kPa, the last one under 131 kPa, and the rest under 135 kPa effective stresses. All these specimens show a peak at axial strains between 0.5% to 1%. The dashed line in this figure is the suggestive trend for increase of the friction angle with density. It can be seen that the post liquefaction friction angles are scatter. The scatter is believed to be due to distortion of the specimens during liquefaction which changed their geometry. The results from those specimens that underwent less distortion (inspected by eye) were more consistent, so were those from specimens with higher densities. For most of the specimens, the shear strength increases after liquefaction because exposure to cyclic load generally increases material compaction degree.

Specimen ID	Max Axial Strain Experienced	Peak Shear Strength			At 10% Axial Strain	
		τ (kPa)	Axial Strain	u^* (kPa)	τ (kPa)	u (kPa)
85C-135-10	1.1%		No peak		62.7	16.5
85C-135-8	0.7%	17.9	0.49%	50.3	4.4	119
85C-135-13	3.6%	15.2	0.54%	54.6	30.3	85.5
85C-135-20	2.2%	22.1	1.15%	75.8	24.1	-2.6
95C-68-15	6.3%		No peak		49.0	-5.5
95C-68-20	1.3%		No peak		68.2	12.4
95C-135-20	3.9%	10.3	0.64%	71.0	107	7.6
95C-135-13	2.9%	19.3	2.0%	82.9	20.0	92.4
95C-340-10	2.5%		No peak		363	-112
105C-135-14	0.68%	406	5.45%	-233	373	-231
105C-135-20	1.4%		No peak		260	-282

* u represents excess specimen pore water pressure

Table 2. Post liquefaction undrained shear strength

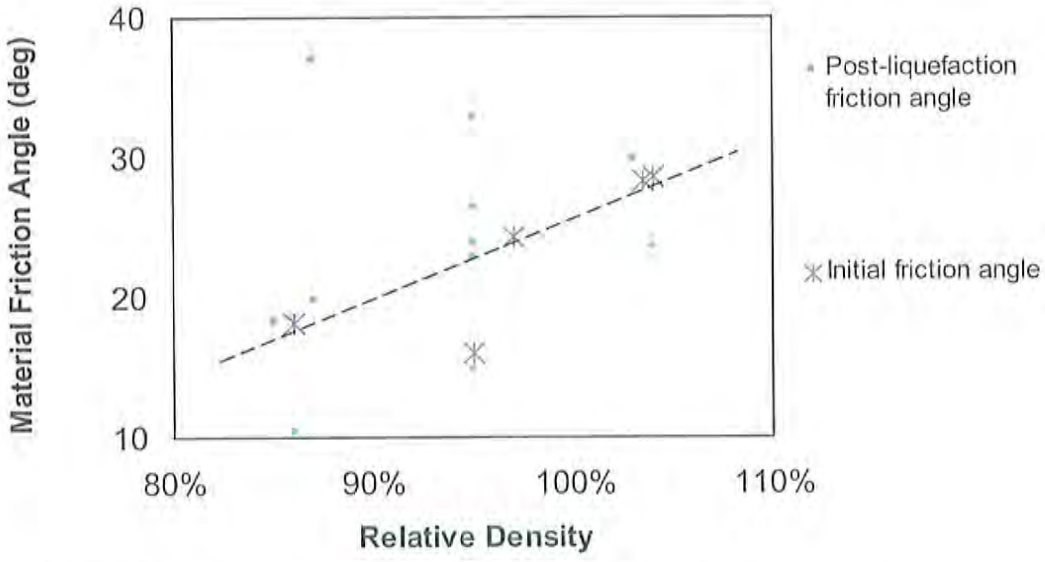

Figure 8. Material friction angles at different densities of the optimum Proctor density

b) Ground Response Analysis

A ground response analysis was performed using the program SHAKE[13] which is a one-dimensional equivalent linear wave propagation analysis. The analysis was carried out for two critical sections, developed based on the results of laboratory and subsurface investigation at Mitchell Station. Site characterization included thickness and unit weight for each soil layer present at the site, and estimates of the dynamic soil properties (shear modulus or shear velocity, modulus reduction and damping models). The two soil profiles, A-A' and B-B', and their dynamic properties are presented in Tables 3 and 4, respectively. Since no specific curves for fly ash materials are available, the curves developed for sands were selected rather than clay to reflect that the fly ash is non-plastic. The maximum shear modulus of sand was assumed to be a function of density and confining stress[14]. For the fine grain materials, the maximum shear modulus was estimated from the undrained shear strength and the subsurface investigation results[14,15], where published shear wave velocities were used to estimate the maximum shear modulus of the sandstone bedrock[16]. Two natural earthquake input motions, El Centro and Taft, were selected to represent the design bedrock motion at the site. The peak accelerations of the input motions were scaled to match the design accelerations of 0.08g and 0.15g as specified by AEP.

Eight analyses were performed using the two selected input motions and the two design peak accelerations. The common cyclic stress approach was used for liquefaction potential evaluation, in which the earthquake-induced loading is compared with liquefaction resistance of the soil expressed in terms of cyclic shear stresses [15]. In order to compare with the cyclic strength determined in laboratory tests, the transient and irregular time history of earthquake-induced shear stresses obtained from the ground response analyses were converted into an equivalent series of uniform stress cycles.

The equivalent number of uniform stress cycles (N_{eqv}) was determined by counting the stress cycles with amplitude greater than 65% of the peak cyclic shear stress (τ_{max}) for a particular shear stress time history [17]. Although different stress levels have been developed for this approach[18], 65% is most commonly used[15]. The uniform shear stress is typically normalized by the initial overburden stress to produce a cyclic stress ratio (CSR):

$$CSR = \frac{\tau_{eqv}}{\sigma_0'} \qquad \text{Equation 1}$$

Pyke et al.[19] showed that multidirectional shaking causes pore water pressure to increase more rapidly than unidirectional shaking. Previous work by other researchers has shown[20] that the CSR required to produce initial liquefaction in the field is about 10% less than values measured in the laboratory. Thus, the predicted field cyclic stress ratios from ground response analysis were corrected accordingly.

The ground response analyses results are summarized in Table 5. Figure 9 presents a comparison between the design earthquake loading predicted from the numerical analysis and the experimentally obtained cyclic strengths. The in-situ density of the material was estimated to range from 92% to 96% relative to the optimum Proctor density. Comparison between the numerical results and experimental liquefaction potential curve for 95% relative density and 135 and 340 kPa confining stress shows that the material has sufficient strength during the design earthquakes and will not liquefy.

Layer No.	Material Description	H (m)	γ (kg/m^3)	G_x (MPa)	Vs (m/sec)	Modulus Reduction & Damping Curve
1	Recompacted Clay Liner	3	2000	26786	304.8	Clay[21]
2	Drainage layer	2.4	2000	22750	280.7	Sand – Average[22]
3	Fly ash	3	1600	6895	172.8	Sand – Average[22]
4	Fly ash	3	1600	8273	189.2	Sand – Average[22]
5	Fly ash	5.5	1600	9653	204.5	Sand – Average[22]
6	Fly ash	9.1	1600	11032	218.5	Sand – Average[22]
7	Fly ash	9.1	1600	12410	232.0	Sand – Average[22]
8	Fly ash	9.1	1600	13100	238.0	Sand – Average[22]
9	Fly ash	9.1	1600	13790	244.4	Sand – Average[22]
10	Sandstone	∞	2245	9.3E6	1700	Linear

Table 3. Site characteristics of soil profile A-A'

Layer No.	Material Description	H (m)	γ (kg/m^3)	G_x (MPa)	Vs (m/sec)	Modulus Reduction & Damping Curves
1	Recompacted Clay Liner	5.5	2000	26786	304.8	Clay[21]
2	Drainage layer	2.8	2000	27579	309.1	Sand – Average[22]
3	Fly ash	3.0	1600	6895	172.8	Sand – Average[22]
4	Fly ash	3.0	1600	8273	189.3	Sand – Average[22]
5	Fly ash	6.1	1600	9653	204.5	Sand – Average[22]
6	Fly ash	6.1	1600	11032	218.5	Sand – Average[22]
7	Fly ash	9.8	1600	12410	232.0	Sand – Average[22]
8	Sandstone	∞	2245	9.3E6	1700	Linear

Table 4. Site characteristics of soil profile B-B'

Parameters	Layer #	Depth (m)	σ_0' (kPa)	τ_{max} (kPa)	τ_{cyc} (kPa)	N_{eq}	CSR
A-A'	3	5.5	107.7	14.84	2.67	4	0.09
Taft	4	8.6	155.6	20.88	13.55	4	0.09
a_{max}=0.08g	5	11.6	203.5	25.66	16.66	4	0.08
A-A'	3	5.5	107.7	19.00	12.35	6	0.11
Taft	4	8.5	155.6	26.62	12.28	6	0.11
a_{max}=0.15g	5	11.6	203.5	32.65	21.21	6	0.10
A-A'	3	5.5	107.7	13.36	8.67	8	0.08
El Centro	4	8.5	155.6	18.29	11.87	8	0.08
a_{max}=0.08g	5	11.6	203.5	21.92	14.27	8	0.07
A-A'	3	5.5	107.7	18.48	12.02	6	0.11
El Centro	4	8.5	155.6	25.66	16.66	6	0.11
a_{max}=0.15g	5	11.6	203.5	31.36	20.40	6	0.10
B-B'	3	7.9	155.6	19.49	12.69	6	0.08
Taft	4	11.0	203.5	23.94	15.56	6	0.08
a_{max}=0.08g	5	14.0	251.4	25.90	16.85	6	0.06
B-B'	3	7.9	155.6	29.68	19.30	5	0.12
Taft	4	11.0	203.5	36.15	23.51	5	0.12
a_{max}=0.15g	5	14.0	251.4	38.59	25.09	5	0.10
B-B'	3	7.9	155.6	18.82	12.21	6	0.08
El Centro	4	11.0	203.5	23.65	15.40	5	0.08
a_{max}=0.08g	5	14.0	251.4	26.43	17.19	6	0.07
B-B'	3	7.9	155.6	26.43	17.19	8	0.11
El Centro	4	11.0	203.5	30.98	20.16	8	0.10
a_{max}=0.15g	5	14.3	251.4	34.33	22.31	8	0.09

Table 5. Summary of the ground response analyses results

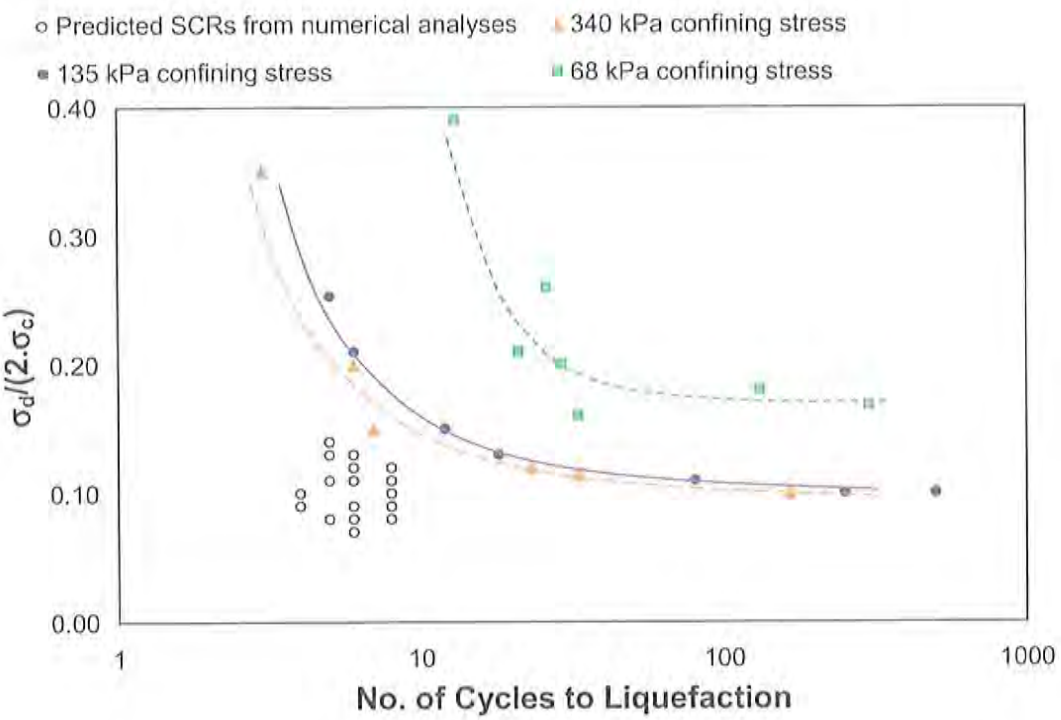

Figure 9. Comparison between the design earthquake load and cyclic resistance of fly ash

4. Summary and Conclusions

The liquefaction potential of an impounded fly ash material was investigated. Cyclic triaxial tests were performed on reconstituted samples with different relative densities, confining stresses, and shear stress ratios. The cyclic shear strength of the fly ash material was presented graphically in terms of cyclic strength curves which show the relationship between density, cyclic stress amplitude, and number of cycles to liquefaction. After cyclic triaxial tests, selected specimens were reconsolidated to the

initial effective confining stress and subjected to CU tests. Additional CU tests were performed to determine the initial static undrained shear strength. The design seismic loading in terms of cyclic stress ratio and equivalent number of cycles were obtained from ground response analyses. The liquefaction potential of the fly ash material was evaluated based on the comparison of the cyclic strength and design earthquake loading. It was concluded that:

1. The cyclic loading imposed by the design earthquakes was found to be lower than the cyclic strength of the fly ash material.
2. Liquefaction resistance of the material was found to be a strong function of initial dry density.
3. In addition to dry density, the liquefaction resistance was found to be influenced by the effective stress at low levels of effective stress (or shallow depths in the field). Cyclic behavior of field material was represented by the specimens consolidated under higher effective stresses.

5. Acknowledgement

AEP suggested the topic of this study and provided the material and classification test data. The authors would like to thank AEP for its support during this investigation. The authors would also like to acknowledge Singh Gursimran Singh for his contribution to the lab work.

6. List of References

1. ACAA 2005 Coal Combustion Products Survey Findings, American Coal Ash Association, 2005.
2. Seed, H.B., and Idriss, I, M., "Ground motions and soil liquefaction during earthquakes," Monograph series, Earthquake Engineering Research Institute, Berkly, Calif, 1982.
3. Seed, H. B., Tokimatsu, K., Harder, L. F., and Chung, R. M., "Influence of SPT procedures in soil liquefaction resistance evaluations," Journal of Geotechnical Engineering, Vol. 111, No. 12, pp.1425-1445, 1985.
4. Sivathayalan, S., "Static, cyclic, and post liquefaction simple shear response of sands", MSc thesis, The University of British Columbia, B.C., Canada, 1985.
5. Boulanger, R. and Seed, R. B., "Liquefaction of sand under bidirectional monotonic and cyclic loading", Journal of Geotechnical Engineering, Vol. 12, No. 2, pp. 870-878, 1995.
6. Youd, T. L. and Idriss, I. N., NCEER. Proceedings Workshop on Evaluation of Liquefaction Resistance of Soils, Technical Report No. NCCER-97-0022, National Center for Earthquake Engineering Research, University of Buffalo, Buffalo, New York, 1997.
7. Finn W. D. L., "State-of-the-art of geotechnical earthquake engineering practice", Soil Dynamics and Earthquake Engineering, Vol. 20, pp. 1-15, 2000.
8. Xenaki, V. C., and Athanasopoulos, G. A., "Liquefaction resistance of sand-silt mixture: an experimental investigation of the effect of fines", Soil Dynamics and Earthquake Engineering, Vol. 23, No. 3, pp. 183-194, 2003.
9. Ghionna, V. N. and Porcino, D., "Liquefaction resistance of undisturbed and reconstituted samples of a natural coarse sand from undrained cyclic triaxial tests", Journal of Geotechnical and Geoenvironmental Engineering, Vol. 132, No. 2, pp. 194-202,2006.

10. ASTM Designation: ASTM D5311, "Standard Test Method for Load Controlled Cyclic Triaxial Strength of Soil", Annual Book of ASTM Standards, 2004, pp. 1167-1176.
11. ASTM Designation: ASTM D4767, "Standard Test Method for Consolidated Undrained Triaxial Compression Test for Cohesive Soils", Annual Book of ASTM Standards, 2004, pp. 913-925.
12. ASTM Designation: ASTM D698, "Standard Test Method for Laboratory Compaction Characteristics of Soil Using Standard Effort", Annual Book of ASTM Standards, 2002, pp. 78-85.
13. Schnabel, P. B., Lysmer, J. and Seed, H. B., "SHAKE – A computer program for earthquake response analysis of horizontally layered sites," EERC Report 72-12. Earthquake Engineering Research Center, Berkeley, California, 1972.
14. Seed, H. B. and Idriss, I. M., "Soil Moduli and Damping Factors for Dynamic Response Analysis," Report No. UCB/EERC-70/10, Earthquake Engineering Research Center, University of California, Berkeley, 1970.
15. Kramer, S.L. (1996). Geotechnical Earthquake Engineering, Prentice Hall, Inc., Upper Saddle River, New Jersey, 653 pp.
16. Burger, H. R., Exploration Geophysics of the Shallow Subsurface, Prentice Hall: Englewood Cliffs, NJ, 1992.
17. Seed, H.B., K. Mori and C.K. Chan, "Influence of Seismic History on the Liquefaction Characteristics of Sands", Report No. UCB/EERC-75/25, Earthquake Engineering Research Center, University of California, Berkeley, 1975.
18. Haldar, A., and W.H. Tang, "Statistical Study of Uniform Cycles in Earthquake Motion", Journal of the Geotechnical Engineering Division, ASCE, Vol. 107, No. GT5, pp. 577-589, 1981.
19. Pyke, R., H.B. Seed and C.K. Chan, "Settlement of Sands under Multidirectional Shaking", Journal of the Geotechnical Engineering Division, Vol. 101, No. GT4, pp. 379-398, 1975.

20. Seed, H.B., K.L. Lee, I.M. Idriss and F.I. Makdisi, "The Slides in the San Fernando Dams During the Earthquake of February 9, 1971 ", Journal of Geotechnical Engineering Division, ASCE, Vol. 101, No. GT7, pp. 651-688, 1975.
21. Sun, J. I., Golesorkhi, R., and Seed, H. B., "Dynamic moduli and damping ratios for cohesive soils," Report No. EERC-88/15, Earthquake Engineering Research Center, University of California, Berkeley, 1988.
22. Seed, H. B., and Idriss, I. M., "Soil moduli and damping factors for dynamic response analyses," Report No. EERC 70-10, Earthquake Engineering Research Center, University if California, Berkeley, 1970.

Figure Captions

Figure 1. Mitchell fly ash impoundment in West Virginia

Figure 2. Grain size distribution of Mitchell fly ash

Figure 3. Calibration of compaction effort for Harvard Miniature samples

Figure 4. Identification of liquefaction for cyclic triaxial tests

Figure 5. Laboratory cyclic test results for confining stress of 135 kPa, showing effect of density on liquefaction resistance

Figure 6. Number of cycles to produce liquefaction as a function of initial density and shear stress ratio

Figure 7. Laboratory cyclic test results for 95% relative density specimens showing the effect of confining stress

Figure 8. Material friction angles at different densities of the optimum Proctor density

Figure 9. Comparison between the design earthquake load and cyclic resistance of fly ash

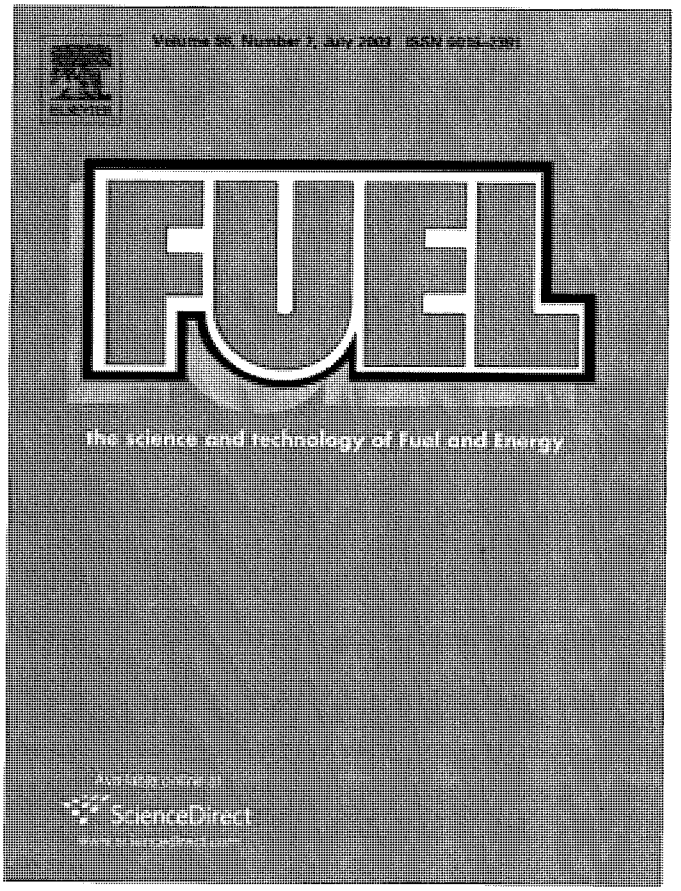

Fuel 88 (2009) 1160–1166

Contents lists available at ScienceDirect

Fuel

journal homepage: www.elsevier.com/locate/fuel

An experimental investigation on liquefaction potential and post-liquefaction shear strength of impounded fly ash

Behrad Zand [a,*], Wei Tu [b], Pedro J. Amaya [a], William E. Wolfe [c], Tarunjit S. Butalia [c]

[a] American Electric Power Service Corporation, 1 Riverside Plaza, Columbus, OH 43215-2373, USA
[b] Black & Veatch Corporation, 8400 Ward Parkway, Kansas City, MO 64114, USA
[c] Department of Civil and Environmental Engineering and Geodetic Science, The Ohio State University, 470 Hitchcock Hall, 2070 Neil Avenue, Columbus, OH 43210, USA

ARTICLE INFO

Article history:
Received 7 May 2007
Received in revised form 3 October 2008
Accepted 7 October 2008
Available online 6 November 2008

Keywords:
Impounded fly ash
Liquefaction potential
Post-liquefaction shear strength
Dynamic triaxial test
Ground response analysis

ABSTRACT

Liquefaction resistance and post-liquefaction shear strength of impounded Class F fly ash are investigated using laboratory experiments. The study was aimed to evaluate liquefaction potential of a 45 ha impoundment proposed as a base for a utility monofill. The evaluation included cyclic triaxial tests performed on reconstituted fly ash specimens with various densities at different confining stresses and cyclic stress ratios representative of the impounded material and the seismic environment. The results are presented in the form of design charts. Post-liquefaction strengths were measured by reconsolidating the specimens at the initial effective confining stress and performing consolidated undrained triaxial tests. The measured cyclic strength was compared with the seismically induced stresses in the profile using a one-dimensional wave propagation method. The cyclic loadings imposed on the ash by the design earthquakes were found to be lower than the measured cyclic strength of the material. The post liquefaction shear strengths showed some scatter; however, they were typically higher than the initial shear strengths before exposure of the material to cyclic load.

1. Introduction

American coal ash association survey [1] estimates the total fly ash production in the US to be 65 million tons (71 million US tons) in 2005, of which only 41% was reused and the rest was left to be disposed in storage ponds or landfills. This fact combined with increasing landfill costs highlights the need for innovative methods to exploit full capacity of existing fly ash landfills/impoundments. A 45 ha fly ash impoundment (Fig. 1), owned by American electric power (AEP) was proposed as the base for a utility monofill. The liquefaction potential of fly ash during an earthquake was a concern of the design team. Although a broad literature exists on the cyclic resistance of sands and clayey soils [2–8] little research has been done on fly ash. In order to address this concern an experimental program combined with ground response analyses was conducted to evaluate the liquefaction potential of the impoundment and the post-liquefaction shear strength of the material. The cyclic strength of the material was evaluated using standard cyclic triaxial tests [9], and the initial and post-liquefaction shear strengths were evaluated in undrained shear (CU) tests [10]. The cyclic loadings induced during a design earthquake motion, estimated from one-dimensional ground response analyses, were compared to the measured cyclic strengths. The cyclic strength of the impounded fly ash was found to be higher than the induced loadings.

2. Testing program and specimen preparation

2.1. Material properties

Class F fly ash produced at AEP's Mitchell power plant was collected from the impoundment at a depth of ~3 m. No other types of coal combustion products have been mixed with fly ash in this facility. A gradation curve is presented in Fig. 2, showing that the dominant particle size is in the silt size range. A specific gravity of 2.27 was measured by AEP. The in situ density of the material was determined by AEP to range from 1600 to 1680 kg/m^3. In situ moisture content under the ground water table was measured to be about 30% by collecting and oven drying bag samples. The in situ dry density of the material is estimated to range from 92% to 96% of the standard Proctor optimum dry density [11]. Presented in Table 1 is the chemical composition of fly ash.

* Corresponding author. Tel: +1 614 716 2873; fax: +1 614 716 2963.
E-mail addresses: bzand@aep.com (B. Zand), tuw@bv.com (W. Tu), pjamaya@aep.com (P.J. Amaya), wolfe.10@osu.edu (W.E. Wolfe), butalia.1@osu.edu (T.S. Butalia).

0016-2361/$ - see front matter © 2008 Elsevier Ltd. All rights reserved.
doi:10.1016/j.fuel.2008.10.020

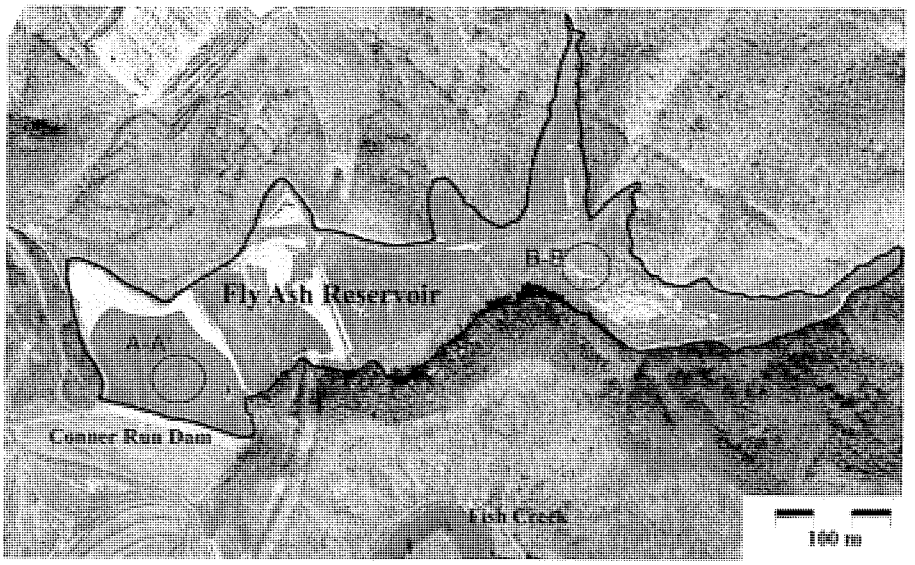

Fig. 1. Mitchell fly ash impoundment in West Virginia.

2.2. Specimen preparation

Fly ash specimens were made in Harvard miniature molds (3.35 cm diameter, 7.11 cm length) using wet tamping to achieve target densities of 86%, 95%, and 104% of the optimum standard Procter dry density (86%, 95%, and 104% relative compactions). Specimens were compacted in five equal lifts using a 110 N (25 lb) hand tamper. Fig. 3 shows a comparison between the standard Proctor and the Harvard miniature calibration curves. Saturation of the specimens was achieved by the application of a small vacuum pressure (<60 kPa) followed by a back pressure of 105–310 kPa. The time needed to saturate the specimens varied from one day to two weeks. All the specimens tested registered B-values larger than 97%.

2.3. Cyclic triaxial test

The cyclic triaxial tests were conducted following the standard ASTM D5311 method for load control cyclic triaxial test [9]. Each saturated specimen was consolidated by applying an effective confining stress σ_c of 68, 135, or 340 kPa, representing typical depths of 3.5, 7, or 20 m, respectively. Specimens were allowed to drain until full dissipation of excess pore water pressure was achieved. Then, each specimen was subjected to a uniform cyclic stress of amplitude σ_d *(zero–peak)* in the axial direction. The ratio of σ_d/σ_c, called shear–stress ratio herein, resembles the amplitude of a shear wave that is normalized by an overburden pressure equivalent to σ_c. Cyclic shear–stress ratios ranged from 7.5% to 40% of the effective confining stress.

Due to the high permeability of the material (on the order of 10^{-4} cm/s) the consolidation occurred rapidly. The cyclic test was conducted under undrained condition and constant cell pressure. The loading frequency was selected to be 0.5 Hz except for one case where a frequency of 1 Hz was used. A 450 N load cell was utilized in load control mode while axial deformations were measured by a

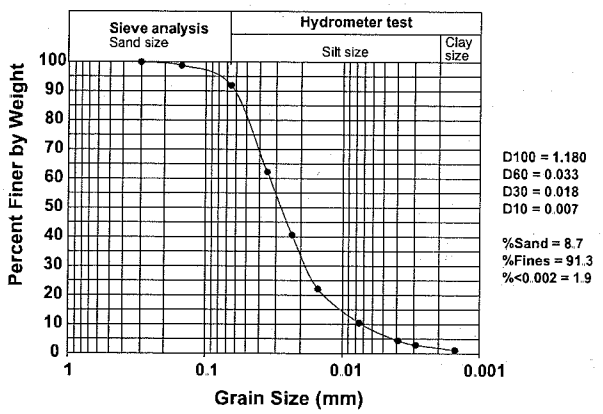

Fig. 2. Grain size distribution of fly ash.

Table 1
Fly ash chemical composition.

Constituent	Results
Silica, SiO_2	54.9
Aluminum oxide, Al_2O_3	17.3
Iron oxide, Fe_2O_3	5.6
Copper oxide, CuO	<0.1
Nickel oxide, NiO	<0.1
Zinc oxide, ZnO	<0.1
Manganese oxide, Mn_3O_4	<0.1
Chromium oxide, Cr_2O_3	<0.1
Molybdenum oxide, MoO_3	<0.1
Lead oxide, PbO	<0.1
Tin oxide, SnO_2	<0.1
Barium oxide, BaO	<0.1
Strontium oxide, SrO	<0.1
Calcium oxide, CaO	3.1
Magnesium oxide, MgO	2.0
Sodium oxide, MgO	0.2
Potassium oxide, K_2O	2.4
Phosphorus pentoxide, P_2O_5	0.1
Sulfur trioxide, SO_3	0.3
Titanium oxide, TiO_2	0.9
Vanadium oxide, V_2O_5	<0.1
Tungsten oxide, WO_3	<0.1
Total carbon, C	0.8
Moisture, H_2O@105 °C	5.7
Net ignition loss (Ignite)	5.6

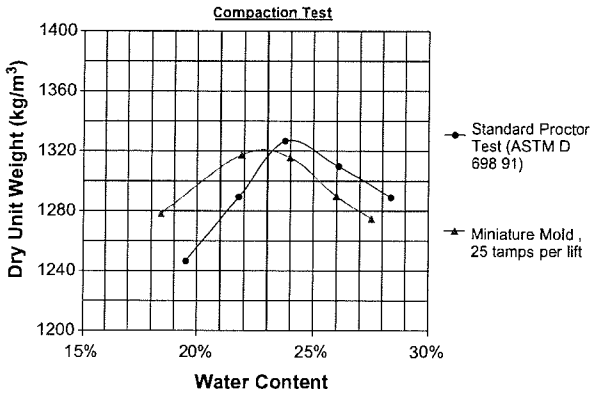

Fig. 3. Calibration of compaction effort for Harvard miniature samples.

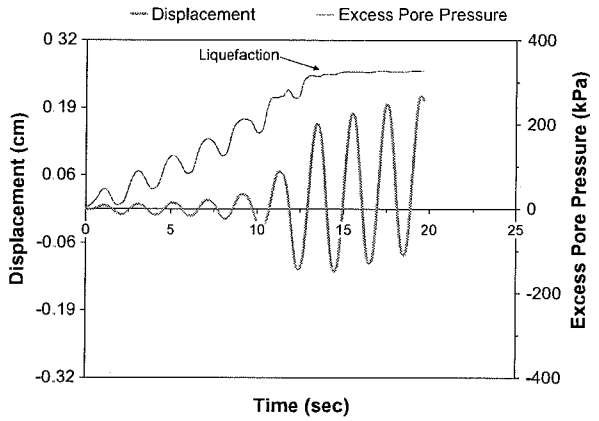

Fig. 4. Identification of liquefaction for cyclic triaxial tests

LVDT attached to loading piston. Specimen pore water pressure and deformation, as well as the deviator load were recorded continuously at a sampling rate of 100 Hz. Liquefaction was defined as the point at which the excess pore water pressure reached the level of the initial effective confining pressure accompanied with a dramatic increase in the axial deformation (see Fig. 4).

2.4. Consolidated undrained shear test

Consolidated undrained (CU) tests were performed on the fly ash to establish the initial static undrained shear strength. Post-liquefaction CU tests were conducted on selected specimens to determine the static undrained shear strength after the earthquake event. The results of the initial and post-liquefaction shear tests are presented in terms of measured internal friction angles (friction angle is the slope of shear strength versus normal stress line in Mohr–Coulomb [12] failure criterion: $S = c + \sigma_N \tan\phi$. In this formula c is cohesion, σ_N is the effective normal stress on the failure plane, and S is shear strength on that plane).

3. Results and discussion

3.1. Laboratory testing

Presented in Table 2 is a list of the specimens tested under cyclic loading together with their relative compactions, effective confining pressures, and shear–stress ratios. Fig. 5 shows the cyclic test results for the fly ash specimens subjected to consolidation stress of 135 kPa. The number of loading cycles to produce liquefaction (N) is seen to decrease with increasing shear–stress ratio and decreasing initial density. On the basis of these results, design curves were established and are presented in the figure, which express the liquefaction resistance (shear–stress ratio) as a function of N and initial density. Using these curves, another family of curves, presented in Fig. 6, was derived expressing N as a function of initial density and shear–stress ratio for specimens consolidated under 135 kPa effective stress.

From Table 2, it can be seen that the initial densities of specimens occasionally deviated from the target value by a small amount. Fig. 6 shows that N is not sensitive to small variation of the initial density when the shear–stress ratio is relatively high. However, for specimens with higher initial densities tested under

Table 2
List of specimens and loading conditions for cyclic tests.

Specimen ID	Initial compaction (%)	Confining stress (kPa)	$\frac{\sigma_d}{2\sigma_c}$ (%)
85C-135-8*	87	135	7.5
85C-135-10*	86	135	10
85C-135-13*	86	135	13
85C-135-15*	85	135	15
85C-135-20*	87	135	20
95C-68-16*	95	68	16
95C-68-17	96	68	17
95C-68-18*	96	68	18
95C-68-20	95	68	20
95C-68-21	95	68	21
95C-68-26	95	68	26
95C-68-40	94	68	40
95C-135-10a	95	135	10
95C-135-10b	95	135	10
95C-135-11*	96	135	11
95C-135-13*	95	135	13
95C-135-15*	95	135	15
95C-135-21*	95	135	21
95C-135-25*	95	135	25
95C-340-10*	95	340	10
95C-340-11	95	340	11
95C-340-12	97	340	12
95C-340-15	95	340	15
95C-340-20	95	340	20
95C-340-37	95	340	37
105C-135-14*	103	135	20
105C-135-20*	104	135	20

* Post-liquefaction CU test conducted.

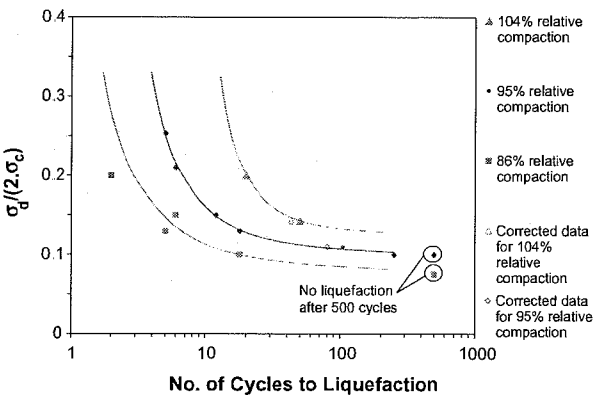

Fig. 5. Laboratory cyclic test results for confining stress of 135 kPa, showing effect of density on liquefaction resistance.

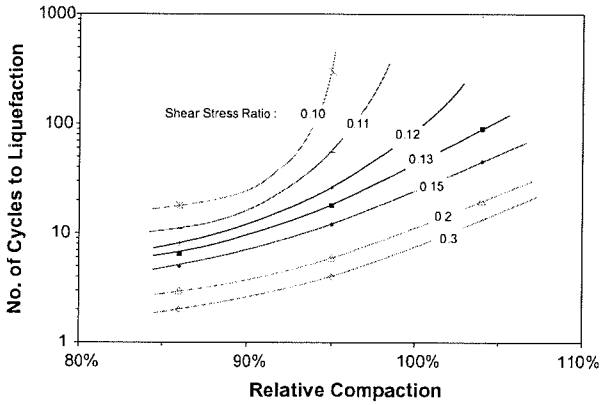

Fig. 6. Number of cycles to produce liquefaction as a function of initial density and shear–stress ratio.

stress ratios lower than 0.13, a small variation in the initial density can influence the results. For instance, the actual relative compaction for the specimen tested at a shear–stress ratio of 0.11 (ID 95C-135-11) was 96% versus the target value of 95%. For this stress ratio, N decreases by 25 cycles when the relative compaction decreases from 96% to 95%. The corrected results for 95% and 104% relative compaction specimens are superimposed in Fig. 5, and there are only two data points for which the difference is apparent. Similar corrections for 86% density specimens do not influence the results because the change is only a fraction of a cycle. Since the established curves presented in the figure are in agreement with the corrected results they were not revised.

Presented in Fig. 7 are the cyclic tests results for the specimens initially compacted to 95% of the Proctor optimum density and consolidated to 68, 135, and 340 kPa. Liquefaction resistance exhibited some dependency to the effective confining stress. The two curves that represent 135 and 340 kPa effective confining stresses were very close; suggesting that as confining stress increases liquefaction resistance becomes less sensitive to the confining stress.

After liquefaction, selected specimens (see Table 2) were reconsolidated to the initial effective confining stress and the post-liquefaction undrained shear strengths were measured. Table 3 presents a summary of these test results for peak strength and strength at 10% axial strain. Also presented are the maximum axial strains experienced during the cyclic test. These data were used to

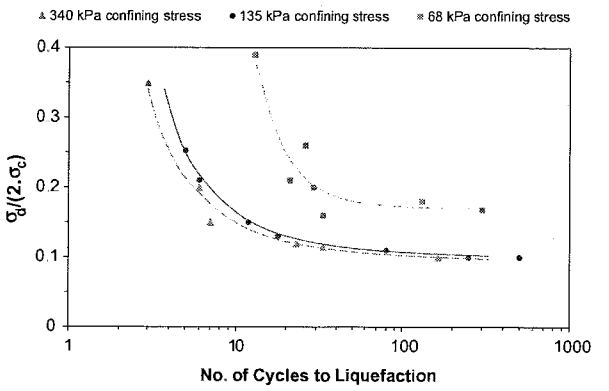

Fig. 7. Laboratory cyclic test results for 95% relative compaction specimens showing the effect of confining stress.

calculate internal friction angle for the material, assuming cohesion is zero. The results are presented in Fig. 8.

$$\sin\phi' = \frac{\sigma_d}{2\sigma'_3 + \sigma_d}$$

In the above equation σ_d is the static deviator stress (which is twice the maximum shear–stress) and σ'_3 is the effective confining stress which is equal to $\sigma_{cell} - u$. Here, u is the measured pore water pressure and σ_{cell} is the cell pressure in the triaxial chamber. For those specimens which did not exhibit a peak in the shear strength, the shear strength at 10% axial strain was used. The figure also contains results from pre-liquefaction CU tests conducted on five specimens compacted to 86%, 95%, 97%, 103%, and 104% of the Proctor optimum density. The first specimen (86%) was consolidated to an effective stress of 103 kPa and the last one (104%) to 131 kPa. The specimens compacted to 95%, 97%, and 103% relative compactions were consolidated to 135 kPa effective stresses. All the specimens show peak strength at axial strains between 0.5% and 1%. The dashed line in Fig. 8 is a trend line showing the friction angle as a function of material density. The scatter in the post-liquefaction friction angles can be attributed to the change in geometry resulting from specimen distortion during liquefaction. The results from those specimens that experienced less amounts of distortion as inspected by eye were more consistent, as were the strengths measured for the specimens with higher densities. It can be seen that, typically, the static shear strength increased after liquefaction. This result is consistent with the observation that sample density increased after exposure to cyclic load. However, the scatter in the post-liquefaction shear strengths indicates additional experiments are needed at greater ranges of initial densities to confirm this observation.

3.2. Ground response analysis

A ground response analysis was performed using the program SHAKE [13] which is a one-dimensional equivalent linear wave propagation analysis. The study was performed for two critical sections, presented in Fig. 9, that were developed based on the results of laboratory and subsurface investigation at Mitchell Station. The approximate locations of these sections are shown in Fig. 1. Site characterization included thickness and unit weight for each soil layer present at the site, and estimates of the dynamic soil properties (shear modulus or shear velocity, modulus reduction, and damping models). The two soil profiles, A-A′ and B-B′, and their dynamic properties are presented in Tables 4 and 5, respectively. The maximum shear modulus of sand was assumed to be a function of density and confining stress [14]. For the fine grain materials, the maximum shear modulus was estimated from the undrained shear strength and the subsurface investigation results [14,15]. Published shear wave velocities were used to estimate the maximum shear modulus of the sandstone bedrock [16]. At the time this study was conducted no published curves for fly ash material were available to the authors. Among the curves available, the authors selected those developed for sands rather than clay or silt to reflect the fact that the fly ash is non-plastic and non-cohesive material. Nonetheless, the grain size distribution of fly ash is different than sand, and the curves developed for a sandy material may not always represent fly ash dynamic characteristics accurately. This fact highlights the need for further investigations on dynamic properties of fly ash. Two natural earthquake input motions, El Centro and Taft, were selected to represent the design bedrock motion at the site. The peak accelerations of the input motions were scaled to match the design accelerations of 0.08g and 0.15g as specified by AEP.

Eight analyses were performed using the two selected input motions and the two design peak accelerations. The cyclic stress

Table 3
Post-liquefaction undrained shear strength

Specimen ID	Max axial strain experienced (%)	At Peak shear strength			At 10% axial strain	
		Shear–stress (kPa)	Axial strain	u^a (kPa)	Shear–stress (kPa)	u (kPa)
85C-135-10	1.1		No peak		62.7	16.5
85C-135-8	0.7	17.9	0.49%	50.3	4.4	119
85C-135-13	3.6	15.2	0.54%	54.6	30.3	85.5
85C-135-20	2.2	22.1	1.15%	75.8	24.1	−2.6
95C-68-15	6.3		No peak		49.0	−5.5
95C-68-20	1.3		No peak		68.2	12.4
95C-135-20	3.9	10.3	0.64%	71.0	107	7.6
95C-135-13	2.9	19.3	2.0%	82.9	20.0	92.4
95C-340-10	2.5		No peak		363	−112
105C-135-14	0.68	406	5.45%	−233	373	−231
105C-135-20	1.4		No peak		260	−282

[a] u represents specimen pore water pressure.

approach was used for liquefaction potential evaluation. In this method the earthquake-induced loading is compared with the liquefaction resistance of the soil expressed in terms of cyclic shear stresses [15]. In order to compare with the cyclic strength determined in laboratory tests, the transient and irregular time history of earthquake-induced shear stresses from the analyses were converted into an equivalent series of uniform stress cycles. The equivalent number of uniform stress cycles (N_{equ}) was determined by counting the stress cycles with amplitude greater than 65% of the peak cyclic shear–stress (τ_{max}) for a particular shear–stress time history [17]. Although different stress levels have been developed for this approach [18], 65% is most commonly used [15]. The uniform shear–stress (τ_{cyc}) was normalized by the initial overburden stress (σ'_0) to produce a cyclic stress ratio (CSR):

$$CSR = \frac{\tau_{cyc}}{\sigma_0'} \tag{1}$$

This ratio is equivalent to the shear–stress ratio in a cyclic laboratory test. Pyke et al. [19] showed that multidirectional shaking causes pore water pressure to increase more rapidly than unidirectional shaking. Previous work by other researchers has shown [20] that the CSR required to produce initial liquefaction in the field is about 10% less than values measured in the laboratory. Thus, the predicted field cyclic stress ratios from ground response analysis were increased by a factor of 1.11 to correct for multidirectional shaking conditions.

The ground response analyses results for 0.15g are summarized in Table 6. The predicted maximum cyclic stress ratio of 0.14 was obtained from the analysis on the B-B′ profile with Taft earthquake input motion at a peak acceleration of 0.15g. Fig. 10 presents a comparison between the design earthquake loading predicted from the numerical analysis and the experimentally obtained cyclic strengths. The in situ density of the material was estimated to range from 92% to 96% relative to the optimum Proctor density. Comparison between the numerical results and experimental liquefaction potential curve for 95% relative compaction and 135 and 340 kPa confining stress shows that the material has sufficient strength during the design earthquakes and will not liquefy.

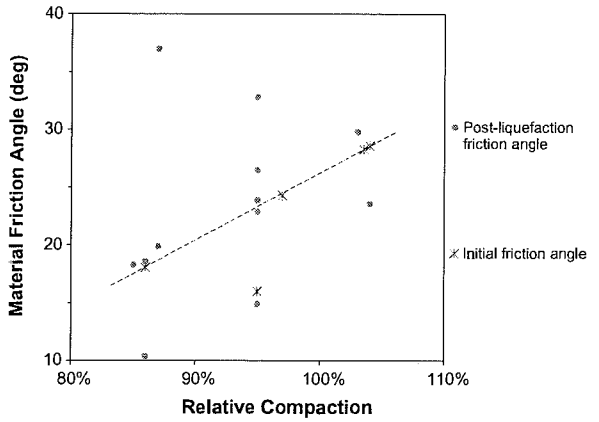

Fig. 8. Material friction angles at different densities of the optimum Proctor density

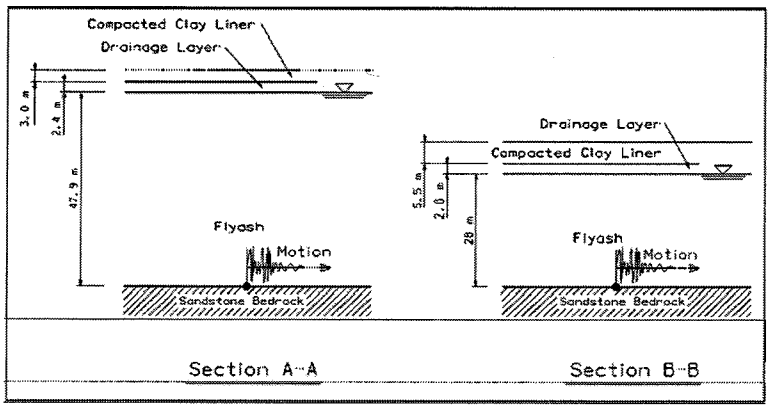

Fig. 9. Idealized sections used in ground response analysis.

Table 4
Site characteristics of soil profile A-A′.

Layer No.	Material description	H (m)	γ (kg/m³)	G_s[a] (MPa)	Vs[b] (m/s)	Modulus reduction and damping curve
1	Recompacted clay liner	3	2000	186	304.8	Clay [21]
2	Drainage layer	2.4	2000	158	280.7	Sand – average [13]
3	Fly ash	3	1600	47.9	172.8	Sand – average [13]
4	Fly ash	3	1600	57.5	189.2	Sand – average [13]
5	Fly ash	5.5	1600	67.0	204.5	Sand – average [13]
6	Fly ash	9.1	1600	76.6	218.5	Sand – average [13]
7	Fly ash	9.1	1600	86.2	232.0	Sand – average [13]
8	Fly ash	9.1	1600	91.0	238.0	Sand – average [13]
9	Fly ash	9.1	1600	95.8	244.4	Sand – average [13]
10	Sandstone	∞	2245	6480	1700	Linear

[a] Initial shear modulus.
[b] Shear wave velocity.

Table 5
Site characteristics of soil profile B-B′.

Layer no.	Material description	H (m)	γ (kg/m³)	G_s (MPa)	Vs (m/s)	Modulus reduction and damping curves
1	Recompacted clay liner	5.5	2000	168	304.8	Clay [21]
2	Drainage layer	2.4	2000	191	309.1	Sand – average [13]
3	Fly ash	3.0	1600	47.9	172.8	Sand – average [13]
4	Fly ash	3.0	1600	57.5	189.3	Sand – average [13]
5	Fly ash	6.1	1600	67.0	204.5	Sand – average [13]
6	Fly ash	6.1	1600	76.6	218.5	Sand – average [13]
7	Fly ash	9.6	1600	86.2	232.0	Sand – average [13]
8	Sandstone	∞	2245	6480	1700	Linear

Table 6
Summary results of ground response analyses for design acceleration of 0.15g.

Parameters	Depth (m)	σ_c' (kPa)	τ_{max} (kPa)	τ_{av} (kPa)	N_{eq}	CSR
A-A′	5.5	107.7	19.00	12.35	6	0.11
Tuff	8.5	155.6	26.62	12.28	6	0.11
	11.6	203.5	32.65	21.21	6	0.10
A-A′	5.5	107.7	18.48	12.02	6	0.11
El Centro	8.5	155.6	25.66	16.68	6	0.11
	11.6	203.5	31.86	20.70	6	0.10
B-B′	7.9	155.6	25.68	15.30	5	0.12
Tuff	11.0	203.5	36.15	23.51	5	0.12
	14.0	251.4	34.59	15.69	5	0.10
B-B′	7.9	155.6	26.42	17.19	6	0.11
El Centro	11.0	203.5	30.98	20.16	6	0.10
	14.3	251.4	34.34	22.31	6	0.09

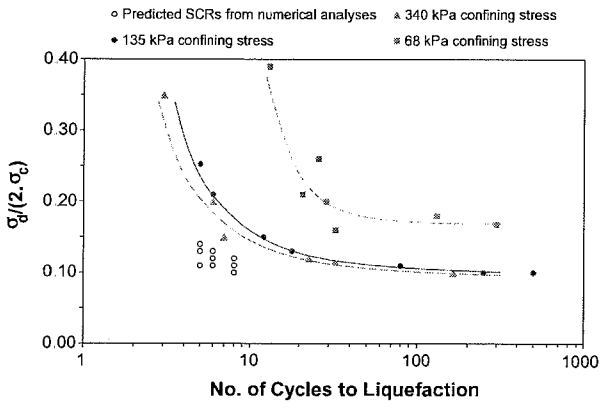

Fig. 10. Comparison between the design earthquake load (0.15g) and cyclic resistance of fly ash.

4. Summary and conclusions

The liquefaction potential of an impounded fly ash material was investigated. Cyclic triaxial tests were performed on remolded samples with different relative compactions, confining stresses, and shear–stress ratios. The cyclic shear strength of the fly ash material was presented graphically in terms of cyclic strength curves which show the relationship between density, cyclic stress amplitude, and number of cycles to liquefaction. After cyclic triaxial tests, selected specimens were reconsolidated and subjected to consolidated undrained (CU) triaxial tests. Additional CU tests were performed to determine the initial static undrained shear strength. The design seismic loading in terms of cyclic stress ratio and equivalent number of cycles were obtained from ground response analysis. The liquefaction potential of the fly ash material was evaluated based on the comparison of the cyclic strength and design earthquake loading. It was concluded that:

1. The cyclic loadings imposed by the design earthquakes were lower than the cyclic strength of the fly ash material.
2. Liquefaction resistance of the fly ash material was found to be a strong function of initial dry density.
3. In addition to dry density, the liquefaction resistance was influenced by the effective stress at low levels of effective stress (or shallow depths in the field). Cyclic behavior of field material was represented by the specimens consolidated under higher effective stresses.

Acknowledgements

AEP suggested the topic of this study and provided the material and classification test data. The authors would like to thank AEP for its support during this investigation. The authors would also like to acknowledge Mr. Gursimran Singh for his contribution to the laboratory work.

References

[1] ACAA 2005. Coal Combustion Products Survey Findings. American Coal Ash Association; 2005.
[2] Seed HB, Idriss, IM. Ground motions and soil liquefaction during earthquakes. In: Monograph series Berkeley, CA: Earthquake Engineering Research Institute; 1982.
[3] Seed HB, Tokimatsu K, Harder LF, Chung RM. Influence of SPT procedures in soil liquefaction resistance evaluations. J Geotech Eng 1985;11:1425–45.
[4] Boulanger R, Seed RB. Liquefaction of sand under bidirectional monotonic and cyclic loading. J Geotech Eng 1995;12(2):870–8.
[5] Youd TL, Idriss IN. NCEER Proceedings workshop on evaluation of liquefaction resistance of soils. Technical Report No. NCCER-97-0022. National Center for Earthquake Engineering Research, University of Buffalo, Buffalo, NY; 1997.
[6] Finn WDL. State-of-the-art of geotechnical earthquake engineering practice. Soil Dyn Earthq Eng 2000;20:1–15.
[7] Xenaki VC, Athanasopoulos GA. Liquefaction resistance of sand–silt mixture: an experimental investigation of the effect of fines. Soil Dyn Earthq Eng 2003;23:183–94.
[8] Ghionna VN, Porcino D. Liquefaction resistance of undisturbed and reconstituted samples of a natural coarse sand from undrained cyclic triaxial tests. J Geotech Geoenvir Eng 2006;132(2):194–202.
[9] ASTM Designation. ASTM D5311. Standard test method for load controlled cyclic triaxial strength of soil. Annual Book of ASTM Standards; 2004. p. 1167–76.
[10] ASTM Designation, ASTM D4767. Standard test method for consolidated undrained triaxial compression test for cohesive soils. Annual book of ASTM standards; 2004. p. 913–25.
[11] ASTM Designation, ASTM D698. Standard test method for laboratory compaction characteristics of soil using standard effort. Annual book of ASTM standards; 2002. p. 78–85.
[12] Boresi AP, Schmidt RJ, Sidebottom OM. Advanced mechanics of materials. 5th ed. John Wiley and Sons, Inc.; 1993.
[13] Schnabel PB, Lysmer J, Seed HB. SHAKE–A computer program for earthquake response analysis of horizontally layered sites. EERC Report 72-12. Earthquake Engineering Research Institute. Berkeley, CA; 1972

[14] Seed HB, Idriss IM. Soil moduli and damping factors for dynamic response analysis. Report No. UCB/EERC-70/10. Earthquake Engineering Research Institute. Berkeley, CA; 1970.
[15] Kramer SL. Geotechnical earthquake engineering. Upper Saddle River. NJ: Prentice Hall; 1996.
[16] Burger HR. Exploration geophysics of the shallow subsurface. Englewood Cliffs, NJ: Prentice Hall; 1992.
[17] Seed HB, Mori K, Chan CK. Influence of seismic history on the liquefaction characteristics of sands. Report No. UCB/EERC-75/25. Earthquake Engineering Research Institute, Berkeley, CA; 1975.
[18] Haldar A, Tang WH. Statistical study of uniform cycles in earthquake motion. J Geotech Eng Div. ASCE 1981;07(GT5):577–89.
[19] Pyke R, Seed HB, Chan CK. Settlement of sands under multidirectional shaking. J Geotech Eng Division, ASCE 1975;101(GT4):379–98.
[20] Seed HB, Lee KL, Idriss IM, Makdisi FI. The slides in the San Fernando Dams during the earthquake of February 9, 1971. J Geotech Eng Division, ASCE 1975;101(GT7):651–88.
[21] Sun JI, Golesorkhi R, Seed HB. Dynamic moduli and damping ratios for cohesive soils. Report No. EERC-88/15. Earthquake Engineering Research Center, Berkeley, CA; 1988.

LIQUEFACTION ANALYSIS OF POND ASH

Shailesh R. Gandhi, Ph.D., Indian Institute of Technology, Madras, India
Ashim K. Dey, Research Scholar, Indian Institute of Technology, Madras, India.

ABSTRACT: Huge quantities of coal ash produced from thermal power plants are disposed in slurry form into lagoons or ponds covering several square kilometer area. The ash in lagoons, called pond ash, is in saturated and loose condition, and liable to liquefy during earthquake. In order to rehabilitate abandoned ash pond, it is therefore, necessary to evaluate the liquefaction potential of pond ash. Present study includes a laboratory investigation on evaluation of liquefaction potential of pond ash. Simplified procedure has been used to evaluate the extent of liquefaction in an ash deposit under different earthquake magnitudes.

Keywords : Liquefaction, pond ash, cyclic loading.

INTRODUCTION

A major source of electrical energy in India is thermal power, which is being generated by burning low-grade coal of high ash content. The current production of ash is about 80 million tons per year (Dayal et al., 1999) out of which a very small percentage (3 to 5%) is being used for various applications. Disposal of the remaining quantity of ash has created a major problem of availability of land. In many thermal power plants the height of ash deposit has exceeded 20 m and the ash ponds have been abandoned. The abandoned ash ponds create environmental hazards by polluting air and ground water, and by inundating the adjoining areas when a breach occurs in the ash dykes due to rain or earthquake motions. The abandoned ash ponds, occupying a very vast area, can be utilized effectively for human habitation, expansion of plant, or increase in pond capacity if the characteristics of ash under static and dynamic loadings are known. Considerable research has been carried out on engineering characteristics of ash (Gray and Lin, 1972, Sridharan et al., 1997, Seals et al., 1972, etc.) but little work has been reported on behavior of ash under dynamic loading. Being cohesionless and non-plastic in saturated condition, the ash has an average particle size (D_{50}) equal to that of silt or fine sand and thus can be susceptible to liquefaction. The present study includes the behavior of ash under dynamic loading, the liquefaction potential of ash and the evaluation of a density at which liquefaction will not occur. The term 'pond ash' is used here for the ash collected from an ash pond in Mettur Thermal Power Plant, Tamil Nadu, India. The property of this ash is found to be similar to that of any other ash obtained by burning low-grade coal in the country.

EXPERIMENTAL INVESTIGATION

To evaluate the liquefaction potential, pond ash samples were subjected to cyclic loading in a triaxial apparatus. Following parameters were varied:

From: Proceedings of the 15th International Conference on Solid Waste Technology & Management. Dec 12-15 1999 Philadelphia, PA.

Relative density, I_D = 50, 60 and 75%;
Initial effective confining pressure, σ_c' = 20, 40 and 60 kPa;
Cyclic stress ratio, CSR = ±0.6, ±0.5, ±0.4, ±0.3, ±0.2 and ±0.1;

CSR is defined as the cyclic shear stress (σ_{dc}/2) divided by σ_c', where, σ_{dc} is the cyclic deviator stress.

Test Set Up: The conventional triaxial test set up was modified by replacing the top cover which can accommodate a loading plunger having a diameter equal to the sample diameter. The test set up is shown in Fig.1 and the modified top cover is shown in Fig.2. This modification eliminates two problems during extension: separation between loading plunger and the sample, and unequal stretching of rubber membrane and the sample. In addition to it, the modification permits independent variation of axial stress and radial stress. The loading plunger is made of nylon having sp.gr. 1.14 so that the seating load on the sample was minimum. To facilitate the top drainage, an opening was provided in the top plunger, and was connected to one of the outlets of the cell through a flexible rubber tube. To minimize the friction between the larger plunger and the top cover, lubricating grease was applied on the contact surfaces. To prevent leakage around the larger plunger, a rubber 'O' ring was provided as shown in Fig.2.

Sample Preparation: The sample was prepared by dry pluviation technique suggested by Ladd (1974), where, oven dried sample was taken in five parts and each part was compacted by vibrating. The weight of each part was predetermined depending on the desired relative density. The final compacted sample was 38 mm in diameter and 80 mm in height. A little vacuum was applied through the bottom drainage valve of the triaxial cell to impart rigidity to the sample while placing the plunger and the top cover. The sample was saturated with distilled water flowing under a small head of 400 mm. Whenever the Skempton's parameter B was less than 1, back pressure was applied through a pair of mercury pots till the parameter B=1 and the sample was kept in this condition for an hour. The saturated sample was then consolidated at k=1 condition (i.e. isotropic condition) for an hour and the volume of water squeezed out during consolidation was noted to obtain the post consolidated diameter and height of the sample.

Cyclic Load Application: Cyclic load was applied to the sample by varying the radial pressure only. From the isotropic state, the axial stress was increased to a value so that the desired shear stress was achieved - this is termed as 'Initiation'. The radial pressure was then varied gradually from the initial condition (= σ_c') to a value double the deviator stress achieved during 'initiation'. The radial pressure was again brought back to σ_c' and the cycles were repeated till liquefaction occurred. Liquefaction is defined as a condition at which the residual excess pore water pressure becomes equal to the initial effective confining pressure σ_c'. Fig.3 shows the stress path followed during this type of load application.

TEST RESULTS AND ANALYSIS

General Characteristics: The tests were carried out with a representative sample obtained by mixing thoroughly equal volume of disturbed samples collected from four widely spaced boreholes at one meter interval. The average properties are: γ_{max} = 12.62 kN/m^3, γ_{min} = 9.27 kN/m^3, e_{min} = 0.54, e_{max} = 1.10, G_s = 1.985, permeability coefficient k = 7.56 x 10^{-5} m/s, c' = 0, ϕ' = 41.4°. The low specific gravity is due to presence of hollow spherical particles

3/8

known as cenosphores. A typical particle size distribution curve is shown in Fig.4. The average in-situ field density was obtained as γ_d = 10.69 kN/m^3 (i.e. e=0.82 and I_D=50%).

Undrained Cyclic Triaxial Tests: Typical variation of applied cyclic shear stress, induced strain and increased pore pressure with time is shown in Fig.5. The time period, T for load application was kept as 10 sec. Typical variation of CSR with number of cycles for liquefaction is shown in Fig.6. It can be seen that with increase in CSR the number of cycles for liquefaction reduces. From this figure it is possible to show the effect of confining pressure and relative density on CSR to cause liquefaction as shown in Fig. 7 and 8 respectively. It can be seen that with increase in confining pressure and relative density, CSR required for liquefaction also increases.

Evaluation of Liquefaction Potential of Ash Deposit : Out of many methods available for evaluation of liquefaction potential, cyclic stress method proposed by Seed and Idriss (1971) is used in this analysis. The earthquake-induced loading, expressed in terms of cyclic shear stresses, is compared with the liquefaction resistance of the soil, also expressed in terms of cyclic stresses. At locations where the earthquake loading exceeds the resistance, liquefaction is expected to occur. The earthquake induced cyclic shear stress (τ_{av}) is obtained from the following equation:

$$\tau_{av} = 0.65 \frac{a_{max}}{g} \sigma_v \gamma_d \qquad (1)$$

The liquefaction resistance in terms of field shear strength τ_f is obtained from the following equation:

$$\left(\frac{\tau_f}{\sigma_v'}\right) = \left(\frac{\sigma_{dc}}{2\sigma_c'}\right)_{50} C_r \frac{I_D}{50} C_M \qquad (2)$$

where, a_{max} is the maximum acceleration at the ground surface and is shown in Table 1 for different earthquake zones in India, σ_v is the total vertical stress at the depth under consideration, r_d is a reduction factor, σ_v' is the effective vertical stress, $(\sigma_{dc}/2\sigma_c')_{50}$ is the CSR causing liquefaction in the laboratory for I_D = 50%, C_r is a correction factor, I_D is the field relative density and C_M is a correction factor for multidirectional shaking usually equal to 0.9 (Seed et al., 1978).

A comparison of τ_{av} and (τ_f) at I_D=50% is shown in Fig.9. It can be seen that ash deposit can liquefy upto 4.0 m in earthquake zone III when water table (WT) is at the ground level (GL). The resistance to liquefaction increases significantly with lowering of water table. With WT at 1 m below surface, there is no chance of liquefaction in Zone III whereas, a depth of 2.5 m is not adequate to prevent liquefaction in Zone IV.

Table 1 : Design Parameters for Earthquake Zones

Earthquake Zones in India	I	II	III	IV	V
Magnitude, M (IS: Seismic Zoning Map)	5	5.5	6.25	6.75	7
a_{max}/g (Calculated)	.058	.097	.211	.354	.459
N_{eq} (after Seed, 1979)	3	5	7	10	12

The extent of liquefaction in an ash deposit can also be evaluated by comparing the equivalent number of cycles, N_{eq}, representing an earthquake with the number of cycles causing liquefaction in the field. The number of cycles causing liquefaction, N_l varies with CSR as per the following relationship.

$$(CSR) = A(N_l)^{-\beta} \tag{3}$$

where, A and β are experimental constants. Putting this relation in equation (2) it is possible to find N_l for field condition. N_{eq} for different earthquake zonesf is shown in Table 1. Figure 10 shows a comparison of N_{eq} and N_l in the field. It can be seen that the ash deposit does not liquefy in zones I and II even for a relative density as low as 50%. For zone III the minimum relative density for no-liquefaction condition is around 65% and for zone IV the deposit gets liquefied even if the relative density is increased to 75%. Thus, ash ponds located in zone IV should be carefully handled and the W.T. should be always kept more than 3 m below the surface.

CONCLUSIONS

Following conclusions are drawn from the present study:

1. The modified triaxial test set up is found to be satisfactory to apply cyclic loadings in the laboratory
2. The ash deposit exhibits a risk of liquefaction in saturated condition for N_{eq} >7 unless the water table is lowered by at least 1 m.
3. The number of loading cycles to create liquefaction reduces with increase in cyclic shear stress magnitude and increases with increase in overburden pressure at larger depth
4. The cyclic stress ratio for liquefaction increases linearly with relative density.
5. There is no risk of liquefaction for ash deposits located in earthquake zones I (M=5) and II (M=5.5). The minimum relative density required for no liquefaction in zone III (M=6.25) is 65%. There is always a high risk of liquefaction for ash deposits located in zone IV (M=6.75) and zone V (M=7) unless the water table is lowered sufficiently below surface.

ACKNOWLEDGMENTS

The work presented is part of doctoral thesis by the second author being submitted to Indian Institute of Technology, Madras, India. The facilities extended by the institute to carry out this study is gratefully acknowledged.

REFERENCES

1. **Dayal, U., S.Shukla and R.Sinha** *Geotechnical Investigation for Ash dykes*, 22-31. In **U.Dayal, R.Sinha and V. Kumar** (eds.) *Flyash disposal and Deposition: Beyond 2000 A D* , Narosa publishing House, New Delhi, 1999.

2. Gray, D.H. and Y.K. Lin (1972) Engineering properties of compacted Fly ash. *Journal of the Soil Mechanics and Foundations Division*, ASCE, Vol.98, SM4, 361-379.

3. Ladd, R.S. (1974) Specimen preparation and liquefaction of sands. *Journal of the Geotechnical Engineering Division*, ASCE, Vol.100, GT 10, 1180 - 1184.

4. **Seals, R.K., L.K. Moulton and B.E. Ruth** (1972) Bottom ash : an engineering material. *Journal of the Soil Mechanics and Foundations Division*, ASCE, Vol.98, SM4, 311-325.

5. Seed, H.B. (1979) Soil liquefaction and cyclic mobility evaluation for level ground during earthquakes. *Journal of the Geotechnical Engineering Division*, ASCE, Vol.105, GT 2, 201-255.

6. **Seed, H.B. and I.M. Idriss** (1971) Simplified procedure for evaluating soil liquefaction potential. *Journal of the Soil Mechanics and Foundations Division*, ASCE, Vol.97, SM9, 1249-1273.

7. **Seed, H.B., R.M. Pyke and G.R. Martin** (1978) Effect of multidirectional shaking on pore pressure development in sands. *Journal of the Geotechnical Engineering Division*, ASCE, Vol. 104, GT1, 27-44.

8. **Sridharan, A., N.S. Pandian and C. Rajasekhar** (1997) Geotechnical characterisation of Pond Ash. *Symposium on Flyash utilization* held at I.I.Sc, Bangalore, India, 43-58.

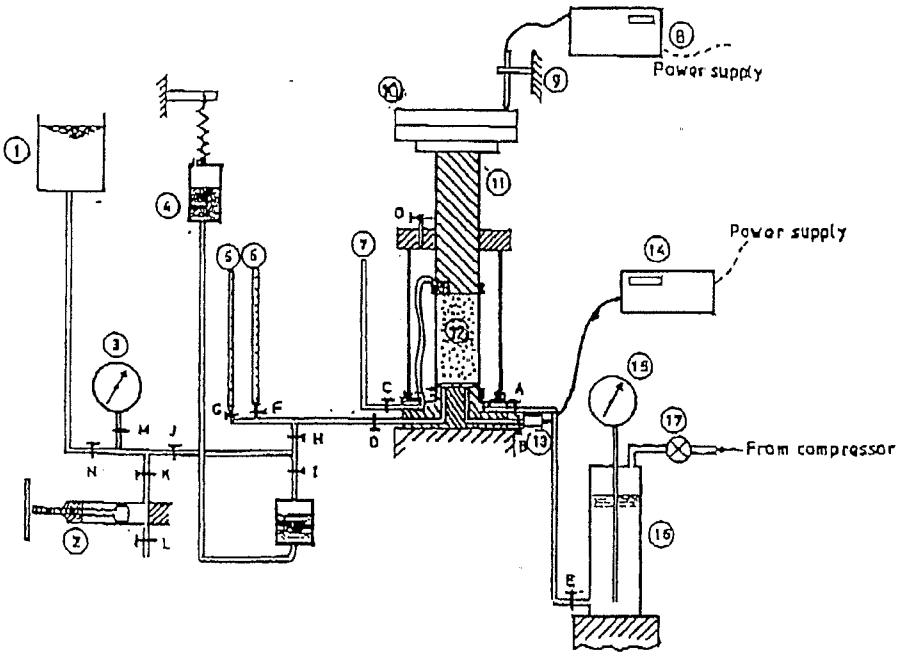

(1) Water reservoir
(2) Screw control cylinder
(3) Pressure gauge
(4) Mercury pot
(5) 0-1.5cc Burette
(6) 0-25cc Burette
(7) Overflow tube
(8) Read out unit
(9) LVDT
(10) Weights
(11) Loading plunger
(12) Sample
(13) Pore pressure transducer
(14) Read out unit
(15) Pressure gauge
(16) Air/water reservoir
(17) Regulating valve

Fig. 1 Test set up

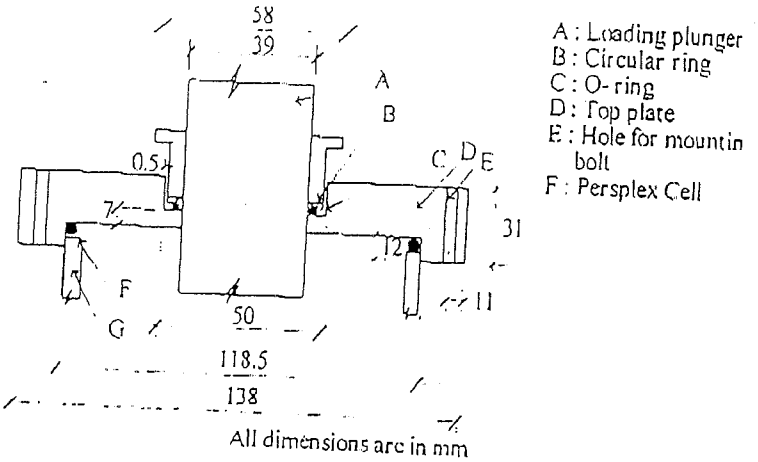

Fig. 2 Details of top cover

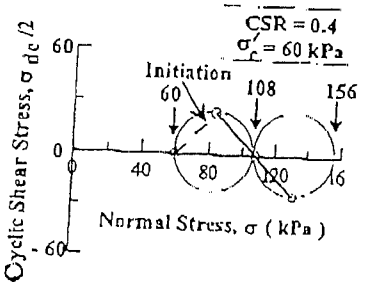

Fig. 3 Stress path for cyclic loading

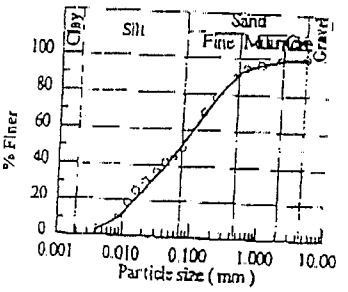

Fig. 4 Particle size distribution curve

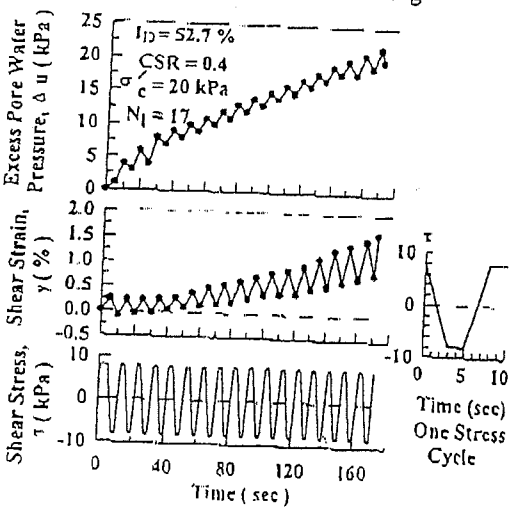

Fig. 5 Typical variation of excess pore water pressure, shear strain, and shear stress with time

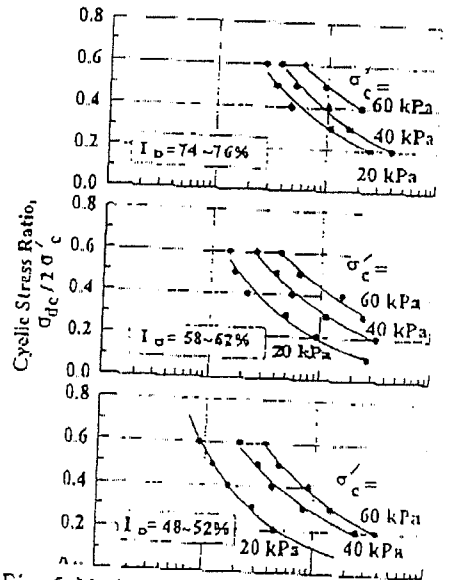

Fig. 6 Variation of CSR with number of cycles for liquefaction

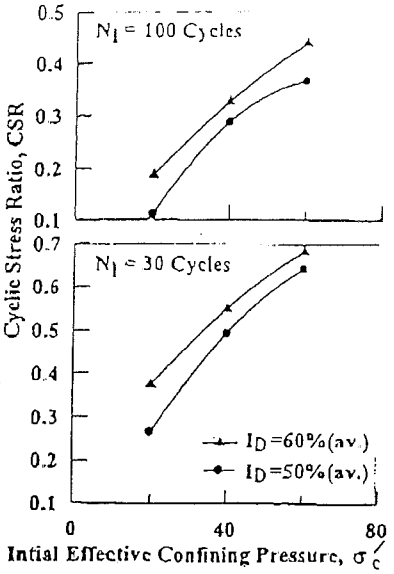

Fig. 7 Effect of confining pressure on cyclic stress ratio causing liquefaction

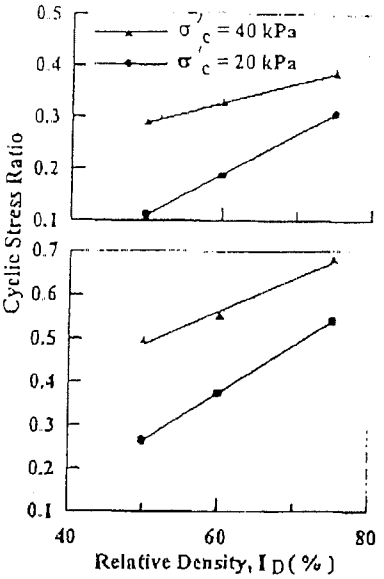

Fig. 8 Effect of relative density on cyclic stress ratio causing liquefaction

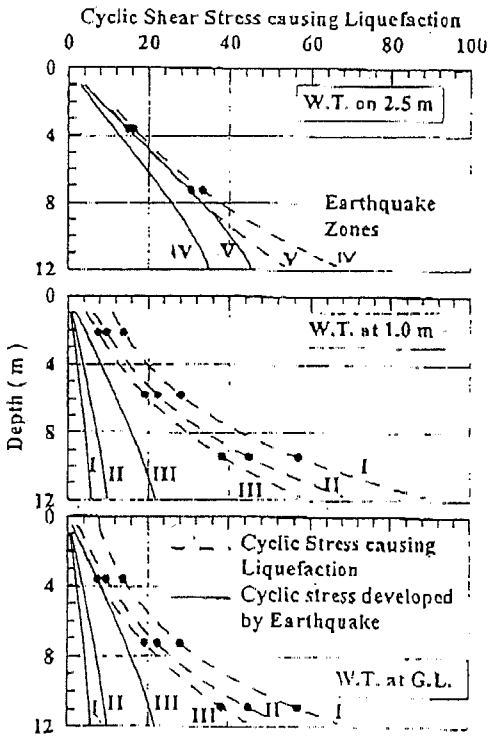

Fig. 9 Comparison of shear stresses at different earthquake zones with water table at different locations over a depth of 12 m

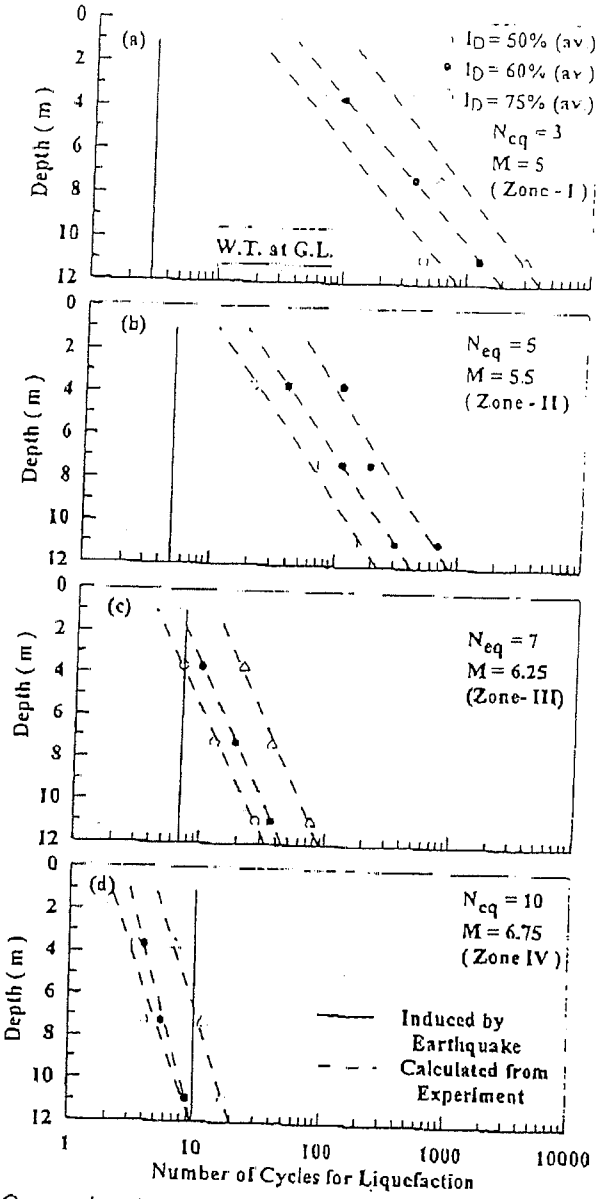

Fig. 10 Comparison between number of cycles causing liquefaction and equivalent number of cycles induced by earthquakes.

ATTACHMENT B
PROPOSED ACTION PLAN IN RESPONSE TO DOWNSTREAM EMBANKMENT SLOUGHING, EROSION AND SURFACE IRREGULARITIES RECOMMENDATIONS
U.S. EPA DIRECTED DAM SAFETY ASSESSMENT
PHILIP SPORN PLANT – MASON COUNTY, WEST VIRGINIA

Introduction

Following is the an outline of the current status of ongoing activities and the proposed action plan for the proposed construction activities related to the recommendations provided in the West Virginia Department of Environmental Protection Division of Water and Waste Management Dam Safety Section inspection report and the draft Dam Safety Assessment Report prepared by Dewberry & Davis, LLC (dated October 2009) as received from the U.S. Environmental Protection Agency.

Downstream Embankment Surface Sloughing Stabilization Work
Current Permitting and Construction Plan

On March 11, 2009 the West Virginia Department of Environmental Protection Division of Water and Waste Management Dam Safety Section performed an inspection of the Sporn Unit 5 Fly Ash Pond Dam. Their inspection report recommended that an Application for a Certificate of Approval be submitted to stabilize the slips on the west exterior slope and depressions on the east exterior slope below the haul road. The report also recommended that a scour analysis for a 100-year flood along the eastern exterior slope be performed to determine if slope armoring is warranted. The referenced report was received on May 14, 2009 and the scour analysis was completed on August 24, 2009 and determined that armoring isn't necessary. The draft Dam Safety Assessment Report prepared by Dewberry & Davis, LLC (dated October 2009) as received from the U.S. Environmental Protection Agency also recommended remedial efforts to address sloughing along the downstream slopes of the management unit.

Since receiving the WVDEP inspection report, American Electric Power Service Corporation on behalf of Appalachian Power Company has taken the following steps to complete those recommended construction activities:

- Plans and an Application for a Certificate of Approval to make the repairs were prepared and submitted to Dam Safety on September 22, 2009 and is currently being reviewed;
- A Stormwater Pollution Prevention Plan is being prepared is being prepared and is scheduled to be submitted during the week of November 2, 2009. Due to the area involved, WVDEP approval of the plan will be at least 45 days;
- Tree clearing commenced on October 28, 2009;
- The grading and stabilization scope of work was reviewed on site with a selected Contractor and a Contract Release was prepared. It is anticipated that the Contractor would be able to mobilize within 2 weeks after notice to proceed, which will be granted upon final approval from the WVDEP.

Given the anticipated issue/approval dates for the Certificate of Approval and the Stormwater Pollution Prevention Plan, construction is planned to commence in late 2009 or early 2010 with the stabilization of the western slope (along the railroad). Given the nature of the grading work on the east exterior slope and the potential for severe erosion through the winter and spring, it is preferable that this portion of the work be deferred until the spring of 2010.

Upstream and Downstream Embankment Surface Sloughing and Erosion Remediation Work
Current Construction Plan

On March 11, 2009 the West Virginia Department of Environmental Protection Division of Water and Waste Management Dam Safety Section performed an inspection of the Bottom Ash Pond Complex. All of the items recommended in that report have been implemented with the exception of the repairing the smaller erosion gullies along the exterior slope of the east dike as a maintenance item. In addition to the WVDEP report, the draft Dam Safety Assessment Report prepared by Dewberry & Davis, LLC (dated October 2009) as received from the U.S. Environmental Protection Agency also recommended remedial efforts to address sloughing along the downstream slopes of the management unit. Additionally, that report recommended erosion repairs along the upstream slopes adjacent to the paved roadway on the crest. It is anticipated that further grading work will be completed by the end of the 2009 calendar year.

ATTACHMENT C
RESPONSE TO COMMENTS REGARDING POSSIBLE SLOPE STABILITY ISSUES RELATED TO RAILROAD INDUCED GROUND VIBRATION
U.S. EPA DIRECTED DAM SAFETY ASSESSMENT
PHILIP SPORN PLANT – MASON COUNTY, WEST VIRGINIA

Introduction

Following is an analysis performed in support of the proposed slope improvement as related to the shallow slope stability issues believed to be the result of the railroad traffic induced vibrations along the west dike. It is believed that the results of the analysis indicate that the proposed stabilization work, when completed, as on Drawing 5-30075, will provide an adequate long-term factor of safety against slope instability due to railroad induced vibrations.

In addition, AEP accepts the contractor's recommendation and will measure railway induced vibrations at the site and conduct analyses to evaluate the impact of the rail traffic on the dikes.

Existing conditions at the dike of concern include approximately 2 ft thick topsoil placed over silty sand. The dike has a maximum slope of 2.2H: 1V with maximum length along the slope of 50 feet. A typical cross-section showing the existing conditions is presented in Figure 1.

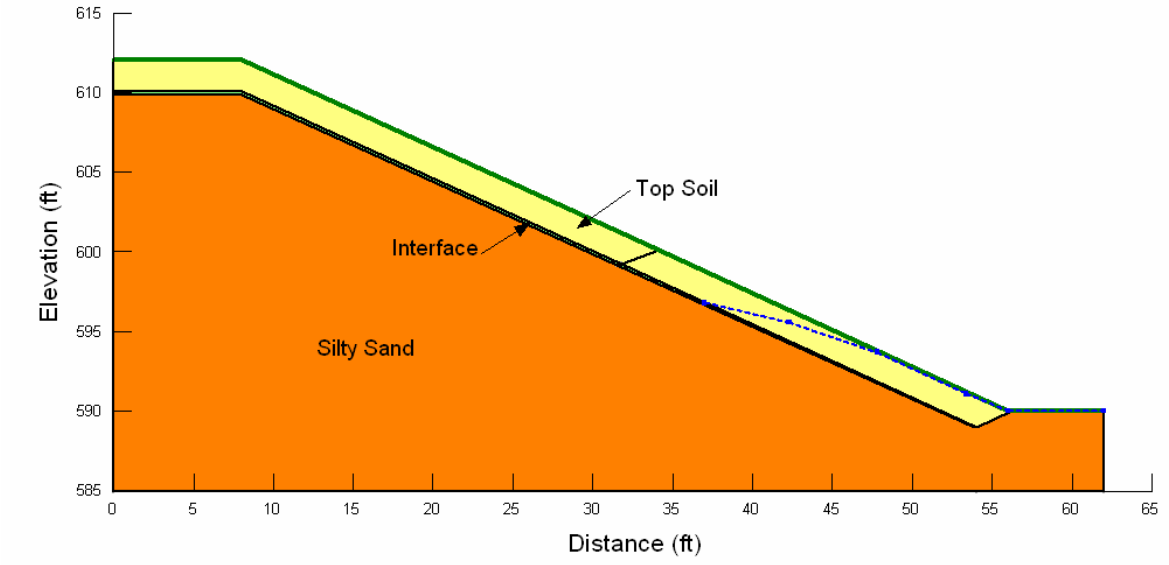

Figure 1. Modeled Existing Conditions.

Field observation indicates that topsoil slipping along the topsoil/silty sand interface is occurring as a result of train induced vibrations. These conditions are simulated in a model prepared using Geo/Slope program. Material properties used in the analysis are presented in Table 1.

Table 1. Material Properties Used in the Analysis

Material	Density, γ (pcf)	Cohesion, c (psf)	Friction Angle, ϕ (Degrees)
Topsoil	110.5	80	23.2
Silty Sand	100	0	35
Topsoil/Sand interface	100	0	30
Riprap	111	0	45

The analysis showed that factor of safety of less than 1 was reached for slipping along the topsoil/silty sand interface under an equivalent acceleration load of approximately 0.12 g induced by the trains. Figure 2 show the results of the analysis.

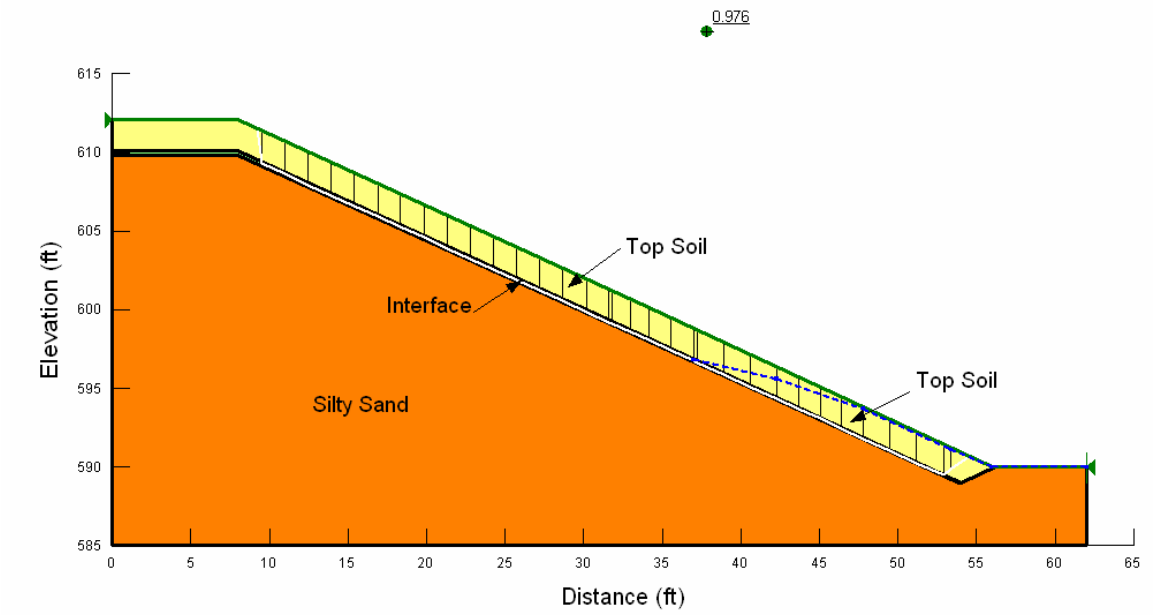

Figure 2. Analysis Results for Existing Conditions

Stabilized scheme include replacing the topsoil at the lower portion of the slope with riprap. The model for the stabilized section is presented in Figure 3. The material property of the riprap is presented in Table 1.

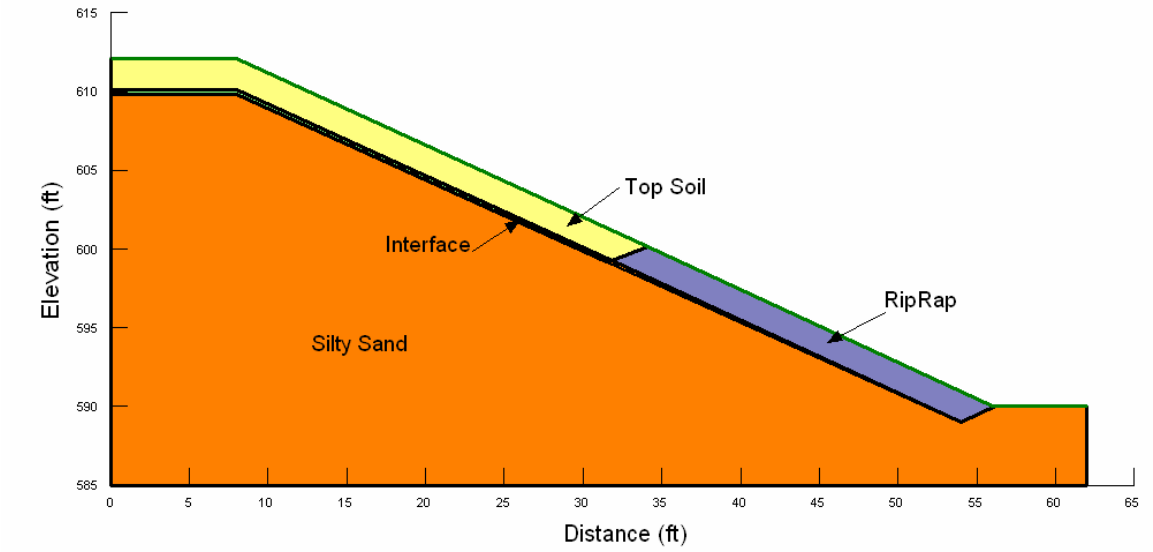

Figure 3. Modeled Stabilized Section.

The results of the analysis of the typical section utilizing the proposed stabilization scheme are shown in Figure 4.

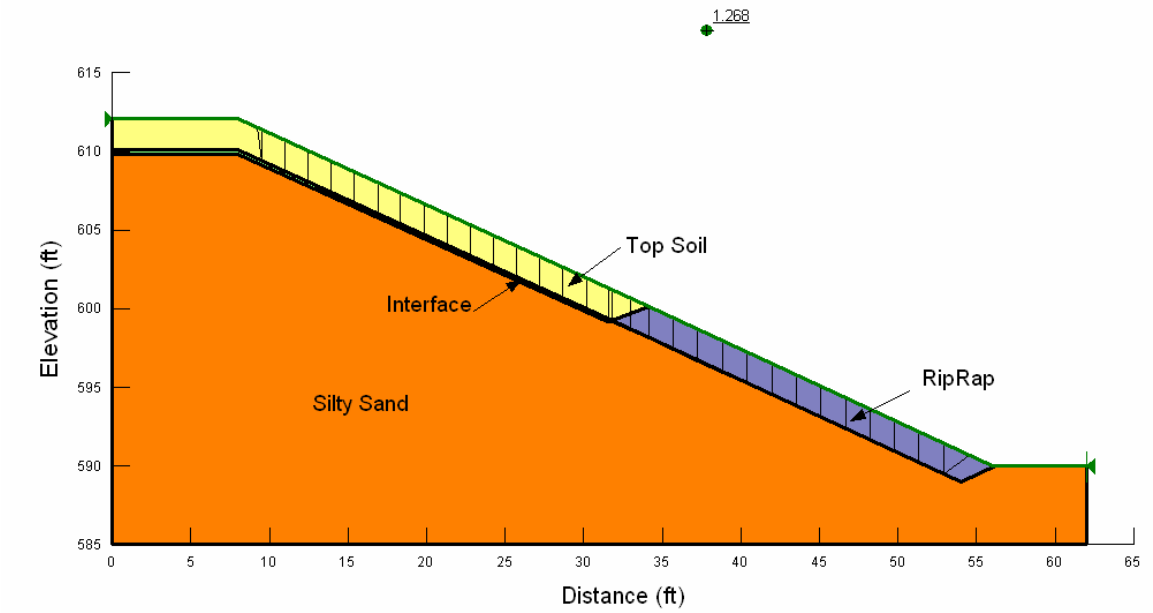

Figure 4. Analysis Results for Stabilized Conditions

Analysis of the stabilized section produced stable conditions with a factor of safety of 1.268 under an acceleration load of approximately 0.12 g induced by the trains. Factors of safety of this magnitude are commonly acceptable for seismic loading.

DWG. NO. 5-30075

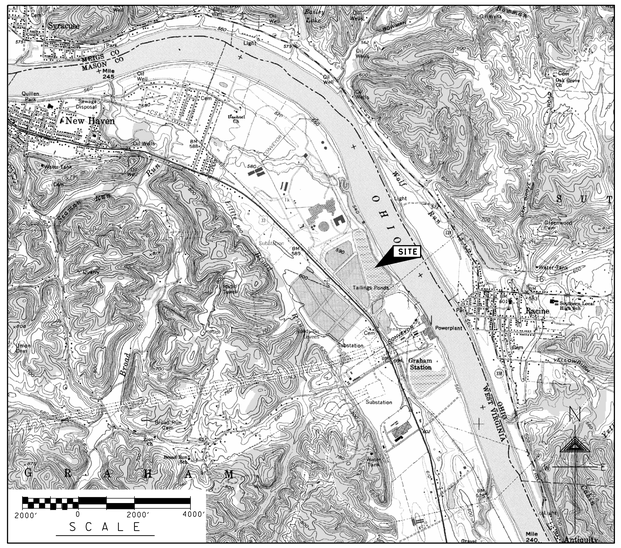

LOCATION MAP

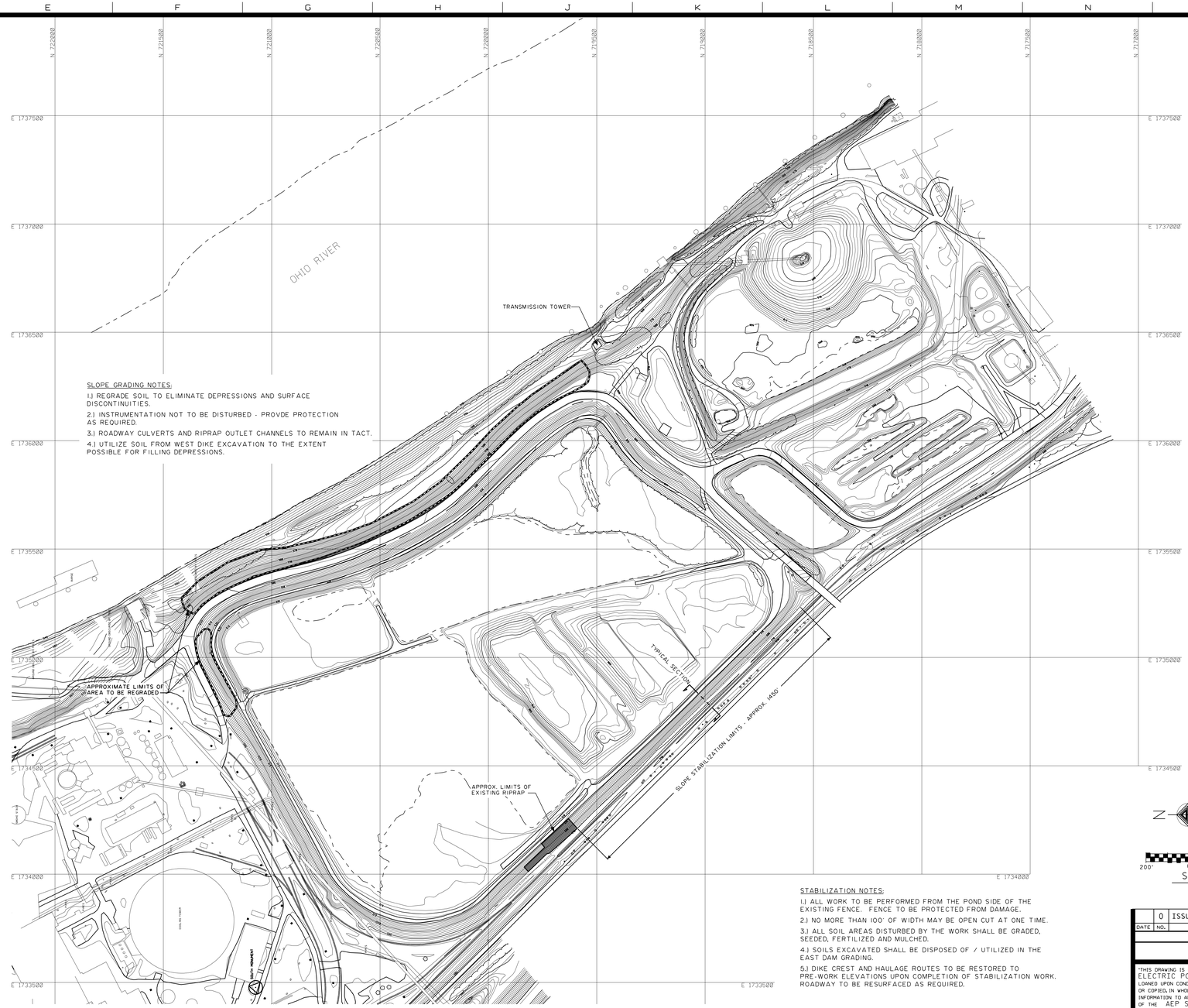

SLOPE GRADING NOTES:

1.) REGRADE SOIL TO ELIMINATE DEPRESSIONS AND SURFACE DISCONTINUITIES.

2.) INSTRUMENTATION NOT TO BE DISTURBED - PROVDE PROTECTION AS REQUIRED.

3.) ROADWAY CULVERTS AND RIPRAP OUTLET CHANNELS TO REMAIN IN TACT.

4.) UTILIZE SOIL FROM WEST DIKE EXCAVATION TO THE EXTENT POSSIBLE FOR FILLING DEPRESSIONS.

STABILIZATION NOTES:

1.) ALL WORK TO BE PERFORMED FROM THE POND SIDE OF THE EXISTING FENCE. FENCE TO BE PROTECTED FROM DAMAGE.

2.) NO MORE THAN 100' OF WIDTH MAY BE OPEN CUT AT ONE TIME.

3.) ALL SOIL AREAS DISTURBED BY THE WORK SHALL BE GRADED, SEEDED, FERTILIZED AND MULCHED.

4.) SOILS EXCAVATED SHALL BE DISPOSED OF / UTILIZED IN THE EAST DAM GRADING.

5.) DIKE CREST AND HAULAGE ROUTES TO BE RESTORED TO PRE-WORK ELEVATIONS UPON COMPLETION OF STABILIZATION WORK. ROADWAY TO BE RESURFACED AS REQUIRED.

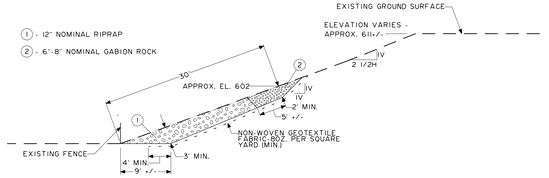

TYPICAL SECTION

10' 0 10' 20'

NOTE: THIS MAP COMPLIES WITH NATIONAL MAP ACCURACY STANDARDS

HENDERSON AERIAL SURVEYS INC.
3889 GROVE CITY RD. GROVE CITY, OHIO 43123

JOB NO.: 42140 NAME: SPORN PLANT
NAD27/NAVD29 WV South
SCALE: 1"=100' AERIAL PHOTOGRAPHY EXPOSED: 05.22.07
CONTOUR INTERVAL: two12foot SHEET: 1 OF 1

NOTE: CONTOURS INSIDE TREE LINES SHOULD BE CONSIDERED AS GROUND OBSCURED

DRAWING IS IN US SURVEY FEET

DATE	NO.	DESCRIPTION	APPD.
	0	ISSUED FOR PERMIT	BBCM

REVISIONS

APPALACHIAN POWER COMPANY

PHILIP SPORN PLANT

GRAHAM STATION W. VA.

UNIT 5 FLY ASH POND MODIFICATIONS

DWG. NO. 5-30075-0

ARCH — ELEC — MECH — STR GS

SCALE: 1"=200' CIVIL ENGINEERING DIVISION

DR: CH: SUP: DATE: APPROVED

AMERICAN ELECTRIC POWER

1 RIVERSIDE PLAZA
COLUMBUS, OH 43215

IG50694

SYSTEM DATE: DD-MMM-YYYY
SYSTEM TIME: HOUR:MINUTE

ATTACHMENT D
RESPONSE TO EPA'S OCTOBER 29, 2009 PRESS RELEASE REGARDING SIMILARITIES BETWEEN SPORN AND KINGSTON.
U.S. EPA DIRECTED DAM SAFETY ASSESSMENT
PHILIP SPORN PLANT – MASON COUNTY, WEST VIRGINIA

INTRODUCTION

AEP has thoroughly reviewed the Kingston root cause report and other information to understand the Kingston failure. In addition, Mr. Pedro Amaya, PE and Manager AEP Geotechnical Engineering, participated in informal peer reviews of the Kingston root cause report with AECOM personnel and others. As a result of these reviews and considerable study of other information available in the public domain, AEP has concluded that the unique conditions that led to the failure at Kingston do not exist at the Philip Sporn facilities.

The attached draft "white paper" prepared by Mr. Barry Thacker, P.E. and Principal Engineer and President of Geo/Environmental Associates, Inc summarizes his preliminary analysis of the claims made in the October 29, 2009 EPA press release and provides an overview of the forensic studies performed after the Kingston failure. In addition, it describes some of the critical factors that differentiate the Sporn ash impoundments from the Kingston facility.

1 November 2009

RE: White Paper on Factors at AEP's Sporn Ash Disposal Facilities as Compared to Those at TVA's Kingston Facility

BY: Barry Thacker, P.E.

BACKGROUND

On 22 December 2008, TVA's Kingston Ash Facility failed. Following the Kingston failure, U.S. EPA conducted on-site evaluations of impoundments at electric utilities nationwide to evaluate the structural integrity of those facilities.

According to a press release dated 29 October 2009, "EPA contractors identified factors at the AEP Philip Sporn facility that are similar to the Kingston facility – specifically, both facilities piled coal ash and bottom ash around the impoundment to raise the impoundment's walls." EPA has alerted West Virginia public officials and first responders that additional safety testing is required at both the Sporn Unit 5 Fly Ash Facility Dam and the Sporn Bottom Ash Facility Dam.

I have reviewed the as-built drawings of the two dams at Sporn and performed a preliminary analysis to evaluate the claims made by EPA contractors. Presented are the results of my preliminary analysis. Furthermore, a summary of forensic studies performed after failure of the Kingston facility is presented for comparison with my understanding of conditions at Sporn.

TVA KINGSTON FACILITY FAILURE AND ROOT-CAUSE ANALYSIS

Construction at Kingston began in 1958 when an earthen embankment, designated as Dike C, was built within an inundated embayment of Watts Bar Lake. Dike C was raised in an upstream direction over sluiced ash in the 1960s using compacted earthen fill and again in the 1970s using compacted ash.

In 1984, construction of dredge cells began on the sluiced ash at Kingston approximately 200 feet upstream (i.e. setback) from Dike C when the sluiced ash had achieved a maximum depth of approximately 45 feet. The outslopes of the dredge cells were constructed in stages using compacted ash. Sluiced ash was then deposited within cells created by the multi-sided outslopes.

The northeastern outslope of the dredge cells, located directly upstream of Dike C, was founded entirely on sluiced ash (i.e. splitter dike). The other outslopes of the dredge cells were founded partially on previous embankments or they abut other dredge cells. No internal drainage provisions were included in the construction of Dike C, whereas numerous internal drains were installed at various levels within the northeastern outslope of the dredge cells.

In 2003 and 2006, "blowouts" reportedly occurred at the downstream toe of the northwestern outslope of the Kingston dredge cells. Internal drainage improvements were made and the dredge cells continued to be raised. At the time of the Kingston failure, the sluiced ash was as much as 90 feet deep beneath the dredge cells and additional raising was in process.

TVA retained AECOM to determine the root cause of the Kingston failure. AECOM concluded that the primary failure occurred at the northeastern outslope of the Kingston dredge cells due to static liquefaction as shown by the results on Figure 1. Furthermore, AECOM concluded that the primary failure caused subsequent failure of Dike C and the northwestern outslope of the dredge cells.

AECOM reported that silt and fine fly ash that deposited in that inundated area of Watts Bar Lake from the Kingston plant prior to the construction of Dike C formed a laminate with water content as high as 140% and other characteristics that make it susceptible to "creep" at a certain loading. "Creep" tests showed failure at shear strength 85% of the peak shear strength. The presence of this layer was the primary contributor to the failure, because without the presence of the slimes layer, failure of the dredge cells would not have occurred.

As shown on Figure 2, AECOM determined that the failure was caused by four overlapping factors as follows:

1. The presence of an unusually weak slimes foundation
2. The fill geometry and setbacks
3. Increased loads due to higher fill
4. Hydraulically placed loose wet ash

AECOM evaluated vibrations caused by train traffic on an active rail line adjacent to the northwestern outslope of the dredge cells as a possible trigger to the failure, but determined that no trains travelled the line at the time of the failure. Also, if vibrations from trains had triggered the failure, then the primary failure would likely have occurred at the northwestern outslope of the dredge cells adjacent to the rail line and not at the northeastern outslope of the dredge cells located several hundred feet from the rail line.

AECOM concluded that triggering of the failure was due to either excess construction pore water pressures in the sluiced ash due to rapid filling of the cells or to the undrained creep of the unusually weak slimes foundation identified beneath the dredge cells.

INDEPENDENT ASSESSMENT OF KINGSTON FAILURE

I analyzed the Kingston Ash Facility based on steady-state seepage and effective stress conditions as part of the due diligence evaluation of AEP's ash disposal facilities in accordance with the design manual *Slope Stability* of the U.S. Army Corps of Engineers. Based on the results of independent modeling, I believe that Kingston's Dike C failed violently due to high

pore water seepage pressures in the underlying sluiced ash. The sluiced ash upstream of Dike C, left unsupported by the Dike C rupture, would still have pore water under high seepage pressure and could then have failed explosively. The loss of sluiced ash upstream of Dike C could have then undermined the downstream toe of the dredge cells.

Although stable during normal operating conditions, I conclude that the rapid loss of its foundation caused the catastrophic collapse of the Kingston dredge cells in a progressive slope failure mode as documented in a white paper report dated 26 June 2009. Results of seepage modeling from that white paper report are shown on the attached Figure 3 and results of stability analysis are shown on Figure 4 for reference.

No piezometers were installed in Dike C at Kingston to validate the independent modeling results, but piezometers were installed in the sluiced ash beneath the northeastern outslope of the dredge cells at the locations shown on Figure 3. Monitoring results from piezometers MW-13 to MW-15 are shown on Figure 5.

According to TVA records, artesian pore water pressure conditions were reached in MW-15 in the fall of 2007. TVA then stopped sluicing to Cell 2 of the dredge cells and water levels in the piezometers gradually decreased. When sluicing resumed on 16 October 2008, water levels in MW-13 to MW-15 were increasing at a rate of 5 to 8 feet per month when artesian conditions were again achieved in MW-15 on 19 November 2008. Sluicing continued to Cell 2 until the artesian pore water pressures increased to the point where Dike C burst as predicted by my modeling results shown on Figure 3 and 4.

Figure 6 shows the results of additional seepage modeling for an imaginary piezometer installed on the bench at elevation 765 feet of Dike C and screened in the underlying sluiced ash. Based on the modeling, increased levels of the sluiced ash in the dredge cells resulted in increased water levels in the sluiced ash beneath Dike C. Although independent analysis based on Corps of Engineers procedures shows the Kingston failure was caused by artesian pore water seepage pressures beneath Dike C, continued raising of the dredge cells after the 2003 and 2006 "blowouts" caused the pore water seepage pressure beneath Dike C to increase to the critical level.

ASSESSMENT OF FACTORS AT SPORN

Unit 5 Fly Ash Facility

The original earthen dikes at the Sporn Fly Ash Facility were built in 1959 using cohesive soil borrow material on a natural brown clay foundation. Some of the borrow material for construction of the dike was obtained from the area between the dikes. Unlike the original construction at Kingston, which was built on a flooded embayment, the site at Sporn was at least

10 feet in elevation above the normal pool level of the Ohio River.

The earthen dikes were then raised in 1965 and 1968 using a combination of cohesive soil and cohesionless soil borrow materials. Unlike the raising of the earthen dike at Kingston, which was done in an upstream direction with a foundation on sluiced ash, the raising of the earthen dikes at Sporn were done primarily in a downstream direction with a foundation on natural clay soil. The exception is at the southeastern corner (i.e.
Section K-K) where the raising in 1965 and 1968 was done by a combination of construction in the upstream and downstream directions.

Expansion occurred again in 1972 when dikes were constructed using a combination of cohesive soil and cohesionless borrow material over sluiced fly ash at the eastern and southeastern portion of the dikes when the sluiced ash was a maximum of 35 feet thick. The maximum height of the dike built in 1972 over sluiced ash was approximately 25 feet. In 1995, an observed line of seepage was found at the downstream toe of the eastern dike. Remedial repairs were initiated, consisting of internal drainage provisions and a buttress built at the downstream toe of the eastern dike.

Furthermore, the maximum allowable level of the sluiced ash was lowered from its design elevation of 620 feet to elevation 605 feet. Unlike the Kingston facility where the level of the sluiced ash continued to increase after remedial repairs were made in 2003, alternative ash disposal provisions were made at Sporn so that the level of sluiced ash has not increased since 2003 and no raising is proposed in the future.

Comparison of factors from the Kingston root-cause analysis in Figure 1 shows that the only factor that applies at Sporn is the presence of hydraulically placed loose wet ash beneath the foundation of the eastern and southeastern dikes. At Sporn, no increased loads have been applied. To the contrary, the allowable sluiced ash level was set at an elevation that is 15 feet below the original design level (i.e. from elevation 620 feet to elevation 605 feet) after seepage was observed and remedial repair was done.

Furthermore, no soft weak foundation zones have been detected at Sporn as would be expected considering that borrow material was excavated between the dikes during the initial construction when the site was dry and not under water as in the case at Kingston. As stated previously, AECOM concluded that failure at Kingston would not have occurred except for the presence of the weak slimes layer and such conditions were not present at Sporn for a slimes layer to form. Finally, unlike Kingston where a 200-foot wide setback was created between the dredge cells and the original construction, no setback is present at the Sporn dikes.

A rail line is present adjacent to the western dike at Sporn, but the dikes within about 500 feet of the rail line are founded on natural ground and not on hydraulically-placed ash fill.

One of the early practitioners in design of ash disposal facilities was Professor Arthur Casagrande of Harvard University who served as a consultant on many of the AEP ash disposal facilities. A 1971 design report he co-authored states: *"When fly ash is deposited from a slurry in a pond, considerable segregation develops according to grain size and specific gravity. The resulting stratification and loose structure produces relatively high horizontal permeability."*

To assess the potential similarities to Kingston with regard to high pore water seepage pressures, finite element seepage analysis was performed for the Sporn Section K-K using a high ratio of horizontal to vertical hydraulic conductivity as recommended by Professor Casagrande. The seepage analysis uses what I consider to be a very conservative ratio of 100 for hydraulically-placed fly ash. As shown by the results in Figure 7, the predicted phreatic level is well below ground surface and is collected by a bottom ash blanket drain and rockfill toe. For the imaginary piezometer shown in Figure 7, the predicted pore water seepage pressure is at a level that is 7 feet below ground surface.

Bottom Ash Facility

Borings drilled through the dikes of the Sporn Bottom Ash Facility show that fly ash was used as structural fill at some locations. Areas where compacted fly ash is present within the original dike core appear to have been buttressed with compacted bottom ash. Rip rap and internal drains are present to provide internal seepage control. The boring data reveal relatively high blow counts within the fly ash portions of the dikes indicating that it is dense.

Comparison of factors from the Kingston root-cause analysis in Figure 1 shows that none of those factors are present at the Sporn Bottom Ash Facility. The only potential concern identified by EPA's contractors appears to be the use of fly ash as structural fill.

The previously referenced 1971 report by Professor Arthur Casagrande warns of the importance of seepage control for dams and dikes retaining fly ash due to its *"extreme sensitivity to erosion, piping, and liquefaction when in a loose state. When fly ash is well compacted… it has good strength characteristics and is safe against liquefaction failure."*

I concur with Professor Casagrande's assessment. In my opinion, the use of dense, compacted fly ash as structural material in the core of the Sporn Bottom Ash Facility dikes is prudent. In its dense state, I assess that it is not subject to liquefaction or significant loss of strength either from earthquake loading or vibrations such as those from trains.

CONCLUSIONS AND RECOMMENDATIONS

Only one of the four factors identified as causing the failure at Kingston is present at the Sporn Unit 5 Fly Ash Facility. The only similar condition is the presence of hydraulically-placed ash beneath some of the dikes. Unlike conditions at Kingston where loading continued even after "blowouts" occurred in 2003 and 2006, loading ceased at the Sporn Fly Ash Facility after seepage was encountered and remedial repair was done.

None of the four factors identified as causing the failure at Kingston are present at the Sporn Bottom Ash Facility. I assess that the dense, compacted fly ash present in the core of the dikes is not subject to liquefaction or significant loss of strength either from earthquake loading or vibrations such as those from trains.

I recommend that a piezometer be installed at the location shown on Figure 7 at Section K-K of the Sporn Unit 5 Fly Ash Facility to supplement the existing monitoring and surveillance program at the site.

Finally, I recommend that AEP continue its practice of design and performance monitoring on its ash disposal facilities according to procedures recommended by the U.S. Army Corps of Engineers.

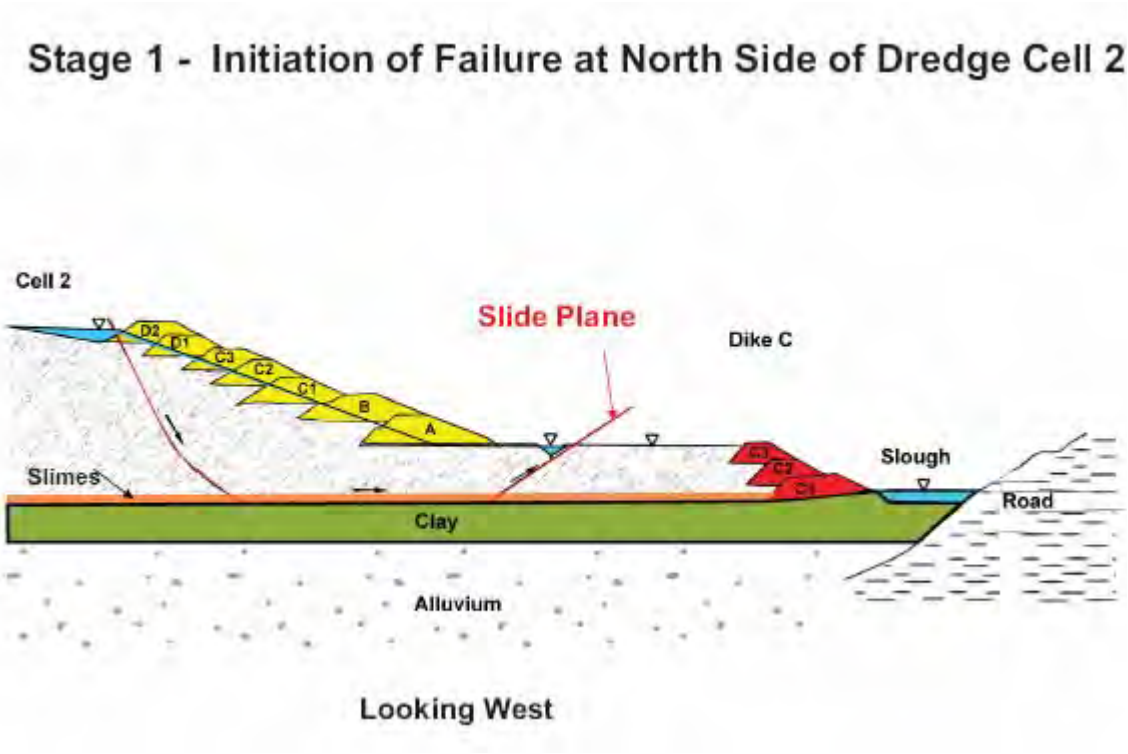

Figure 1. Primary failure surface location at Kingston from AECOM study

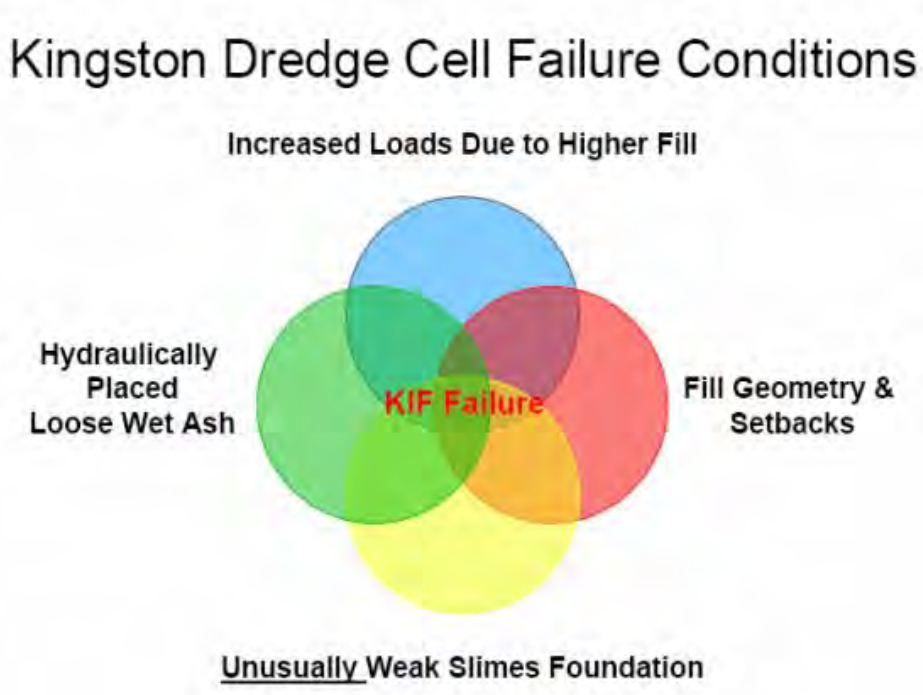

Figure 2. Overlapping causes of Kingston Ash Facility failure according to root-cause analysis performed by AECOM

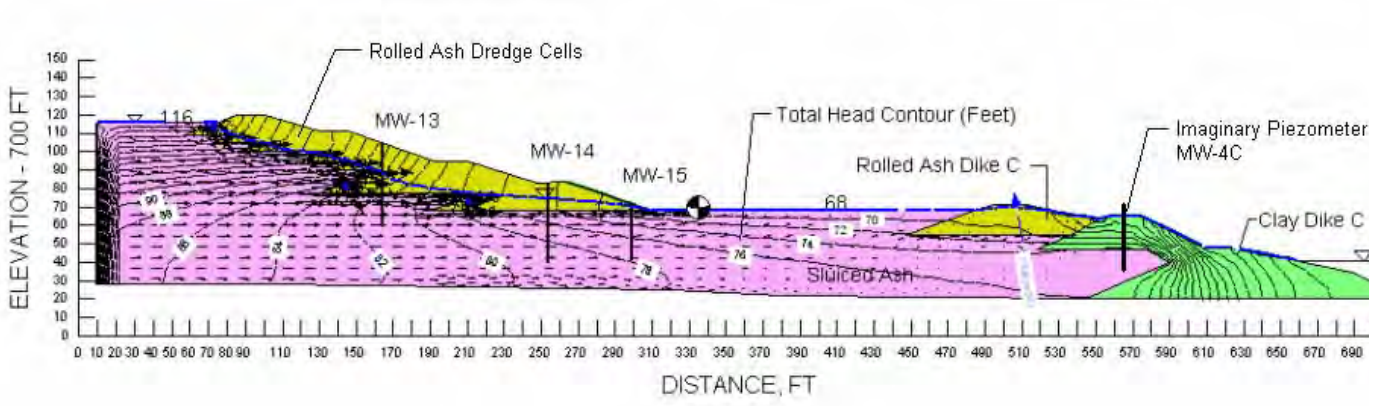

Figure 3. Results of finite element seepage analysis of Kingston Ash Facility from independent study (Note: Actual piezometers MW-13 to MW-15 installed on outslope of dredge cells were screened in the sluiced ash at the level where the sluiced ash underlies Dike C. Ground surface at MW-15 is at elevation 771 feet).

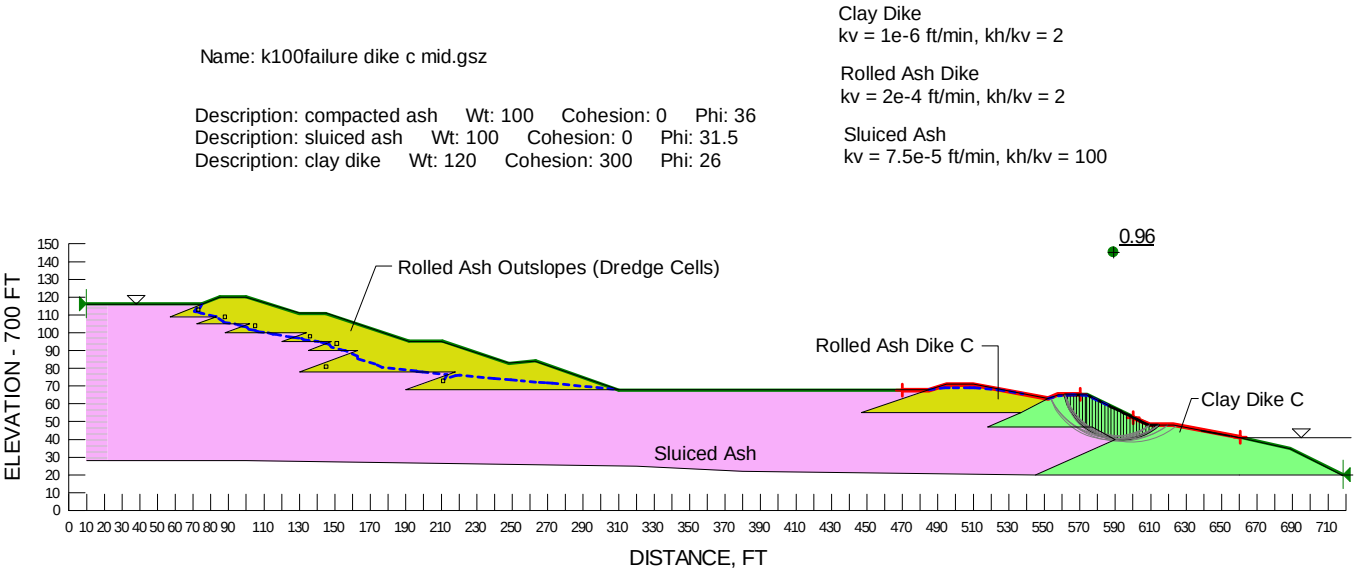

Figure 4. Results of stability analysis of Kingston Ash Facility from independent study predicting factor of safety less 1.0 at Dike C for steady-state seepage condition

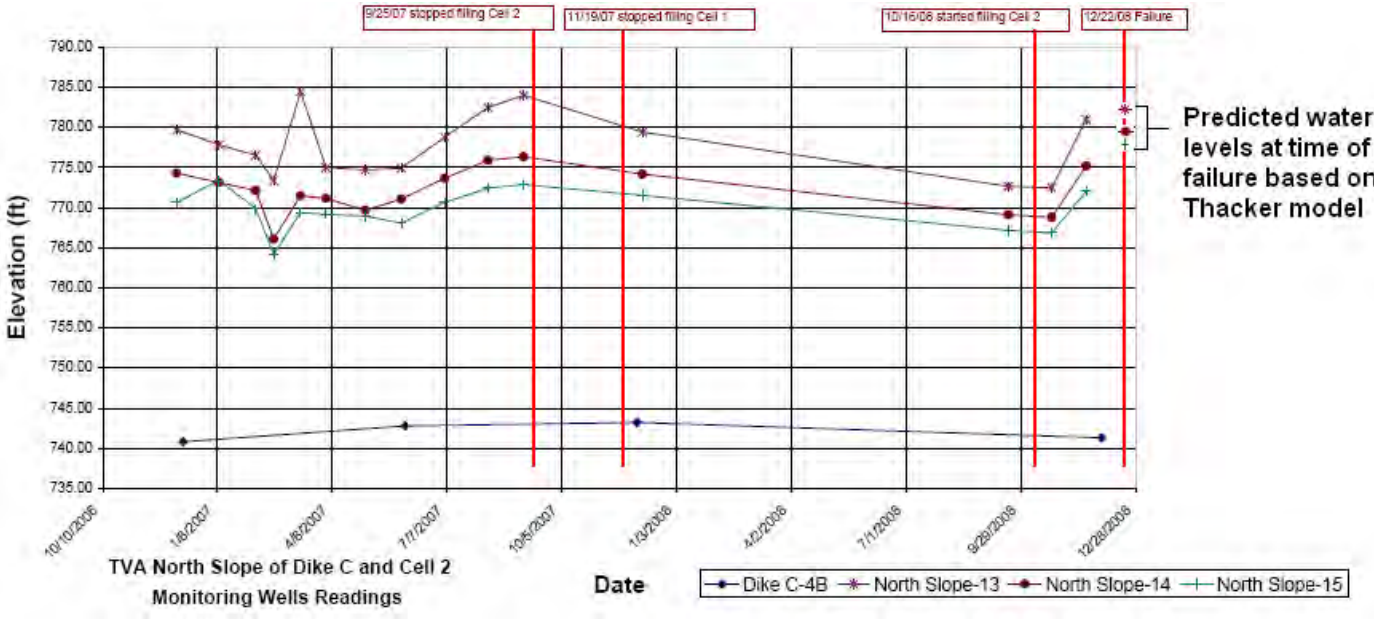

Figure 5. Water level monitoring data from Kingston provided by AECOM showing artesian conditions at piezometer MW-15 on 19 November 2008. Even after artesian conditions developed in MW-15 on 19 November 2008, sluicing to dredge cells continued until failure occurred on 22 December 2008.

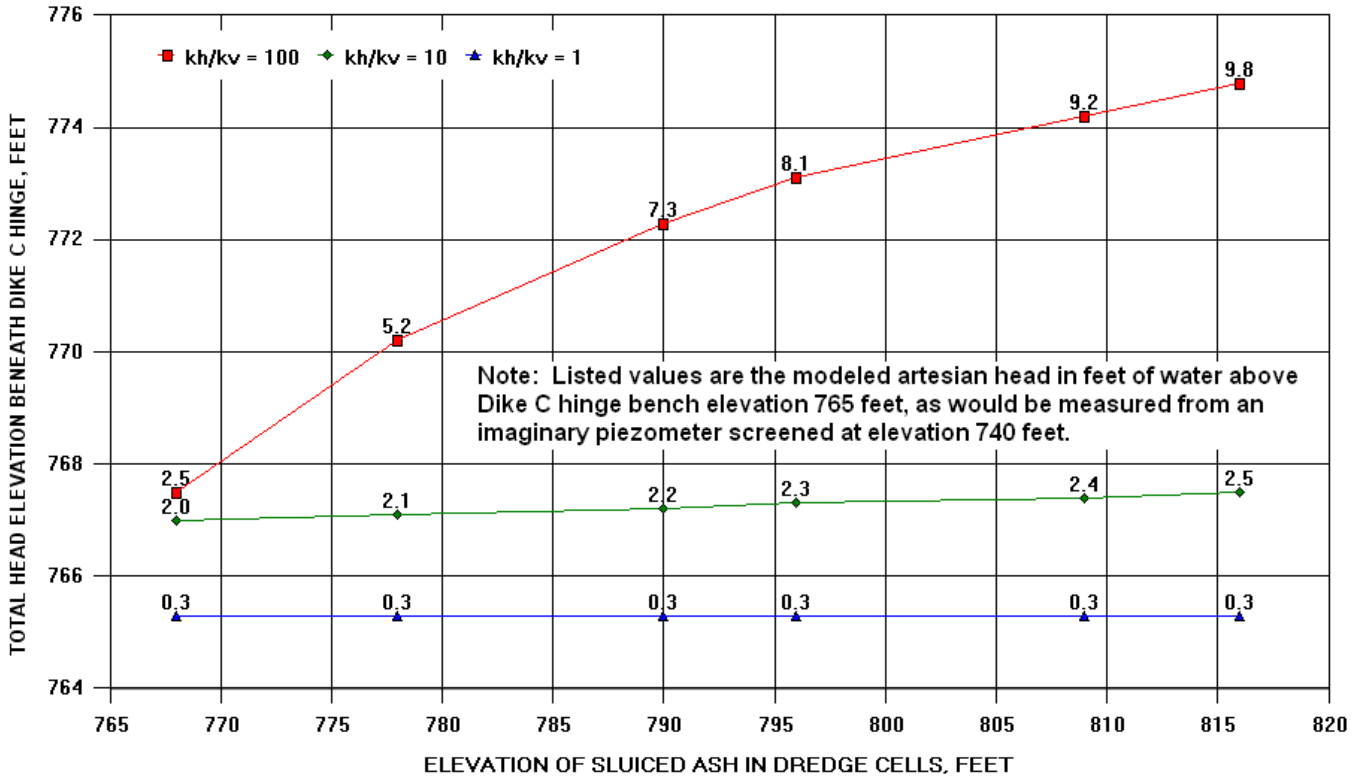

Figure 6. Water levels predicted by independent study for imaginary piezometer MW-4C installed through the clay-portion of Dike C at Kingston during raising of dredge cells

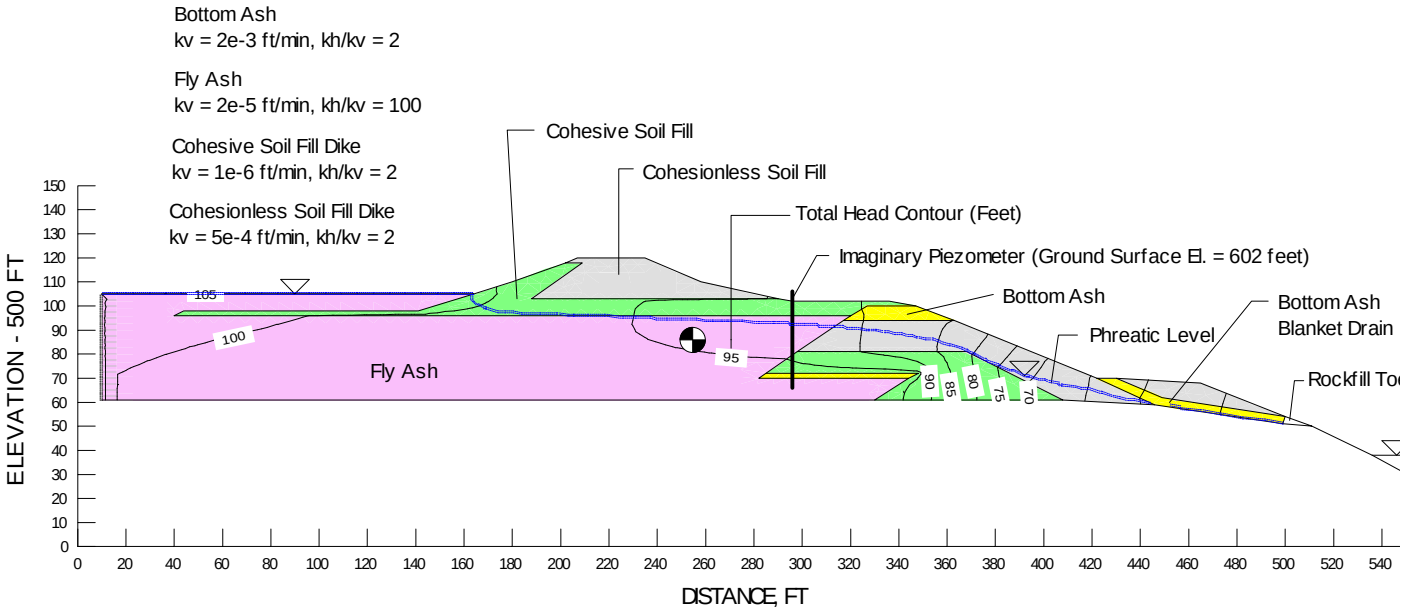

Figure 7. Results of finite element seepage analysis for Sporn Fly Ash Facility Section K-K predicting controlled internal drainage beneath dikes (Note: Imaginary piezometer predicts a water level that is 7 feet below ground surface)